Feedforward control for wave disturbance rejection on floating offshore wind turbines

M.K. Al

Master of Science Thesis

TU Delft Delft University of Technology

Delft Center for Systems and Control

Feedforward control for wave disturbance rejection on floating offshore wind turbines

Master of Science Thesis

For the degree of Master of Science in Systems and Control at Delft University of Technology

M.K. Al

December 20, 2019

Faculty of Mechanical, Maritime and Materials Engineering (3mE) · Delft University of Technology

Abstract

Floating Offshore Wind Turbines (FOWTs) offer an alternative to fixed-bottom wind turbines in deep waters. However, FOWTs are not yet economically feasible due to engineering challenges. Particularly, dynamics of the floating platform are disturbed by wind and waves. In the field of control engineering, feedback (FB) control is primarily used to address the problem. Control of the blade pitch angle and the electrical generator torque based on measurements of the system, is used to attenuate external disturbances. However, FOWTs remain moderately sensitive to wind and waves. FB control can only attenuate an error once it is already occurring.
In addition to FB control, feed forward (FF) is a simple and powerful technique that complements FB to reduce the effect of measurable disturbances (e.g. wind and waves). With a perfect measurement of a disturbance, FF control provides perfect attenuation while the FB control provides robustness against uncertainties. The objective of this research is to identify the potential and feasibility of FF control to reject wave-disturbances on FOWTs.

In this research, the effectiveness of a novel wave-FF controller is validated via a case study on a floating system to reject the wave-induced rotor speed variations. The wave-affected dynamics are identified using high-fidelity simulations, by comparing load cases with- and without waves. A linear model is obtained, expressing the turbine dynamics as a function of surface elevations. Real-time implementation of the FF controller has become possible by developing a wave-prediction method. Then, linear system analysis is used to determine which dynamics are sensitive to waves and which control actions are effective for rejecting wave-excitations. A linear model-based wave-FF controller is developed based on linear model inversion and it is added to the standard wind turbine FB controller. The performance of the FF+FB controller is compared to a regular FB controller via similar simulations.

The high-fidelity simulations illustrate that waves are primarily affecting the tower base fatigue damage, the blade pitch control action and rotor speed variance. Therefore, the initial control objective is to attenuate wave-induced rotor speed variations. Via simulation, a 27% rotor-speed variation reduction is obtained requiring 11% fewer blade pitch control action with respect to baseline control. The reduction is equivalent to 92% of the *wave-induced* rotor speed variations. It shows that wave-FF is an effective control strategy to strongly reduce the rotor speed variations. Moreover, the results raise the question of what additional control

objectives can be achieved using FF control. On the downside, larger additional generator torque actions are needed, leading to 135% more fatigue damage on the rotor shaft. By tuning the FF controller gain down, one can trade-off the performance with the control action. Ultimately, scaled experiments have been conducted in the wave basin at MARIN, confirming the correctness of the wave-prediction method. For verification on the FF controller, further experiments are required.

Altogether, this work has confidently demonstrated the feasibility and effectiveness of wave-FF control on FOWTs by mathematical derivation and simulation. Further research should aim to verify the results using scaled experiments. Especially higher-order wave excitation forces and the effect of measurement errors are recommended to be reviewed. A generalised procedure is developed to extend the theory towards alternative control objectives and FOWTs. Considering the observations in this study, it would be a waste not to accommodate wave knowledge into the control action. Using FB control, undesired dynamics are attenuated once they are measured. With FF control, the idea is to attenuate undesired dynamics before they occur.

Table of Contents

List of Figures

List of Tables

Preface

This master thesis report is part of the graduation project of M.K. Al, under the supervision of Prof.Dr.Ir. J.W. van Wingerden and Ir. D.C. van der Hoek. I would like to thank them for their contribution. I would like to thank Prof.Dr.Ir. A. Reniers, Ir. A. Fontanella, Ir. S. Mulders and Dr. Y. Liu for their collaboration. Furthermore, I would like to thank Kari, Lottelein, Folkert, Joris, Rogier for their support and feedback during my graduation.

This master thesis is written for readers with a considerable background in control engineering with a special interest in floating offshore wind turbines. It is based on the literature survey on the state of the art control strategies for floating offshore wind turbines [8].

The report is kept as brief as possible. It focused on presenting new findings, rather than to repeat existing work. Well-known concepts from systems and control engineering will only receive a brief introduction. FOWT technology is provided with a brief description, whereafter a source is given for further elaboration. For a solid background on FOWT from a control point of view, please ask for the literature report.

In the literature survey, it was found that much promising research exists, however, it is not being implemented. Therefore, this work stresses the contribution to realistic industry implementation.

Chapter 1

Introduction

In a world of growing wealth, the emission of greenhouse gasses is leading to global warming. Climate change has become one of society's major challenges. In the Paris Agreement [9] from 2015, a union of 197 nations agreed on a common long-term goal to reduce global warming, by keeping the global temperature rise well below 2°C in 2050. This agreement is a driving force for a transition towards renewable energy technologies. Consequently, the wind energy industry has been growing strongly over the past years. In Europe, the maximum available wind energy capacity grew from 50 GW in 2007 to 170 GW in 2017 [10], becoming the second-largest energy source in Europe when operating on full capacity.

Onshore wind turbines are economically most attractive, in terms of levelised cost of energy (LCOE) [11]. Their cost to produce electricity is the second most cost-effective renewable energy source available, after bio-fuel [12]. However, civil obligations on account of visual pollution and noise disturbance cause their deployment to be a politically unpopular choice.

More popular are offshore wind turbines (OWTs), as they are deployed in uninhabited areas. Wind resource offshore tends to be stronger and more uniform [13]. However, OWTs come with several additional challenges. First, the LCOE of OWTs is about 2.5 times then an onshore wind turbine [12]. Second, OWTs tend to have more negative environmental impact [14]. Third, people experience 'horizon pollution' as OWTs are generally visible from coastal areas. Finally, the area in which OWTs can be deployed is seriously limited, as they cannot be placed in waters deeper than about 60 meters [15], shipping lanes or protected natural parks.

The use of FOWTs allows OWTs to be deployed non-visible from coastal zones, enjoy higher wind speeds and eliminates limitations on deployment area by water-depth. Moreover, assembly of a FOWT is simpler as it can take place in the harbourside, instead of on location. Some estimations argue that FOWTs have the potential to produce energy at a lower or equal cost compared to OWTs [11]. Either way, FOWTs are likely to become the preferred option at specific sites.

In this chapter, the background and major challenges of FOWTs will be discussed. Moreover, the motivation and aim of this research will be explained. The content of the chapter is

based on literature research. Section 1-1 provides key-background information regarding the technology and its state of development. Section 1-2 addresses the main challenges of FOWTs. Section 1-3 provides insight into the most important findings on state-of-the-art control, by briefly indicating where a gap in knowledge exists. Section 1-4 will introduce the main objective of this work. Finally, the outline of the report is discussed in Sec. 1-5.

1-1 Background of floating offshore wind turbines

A FOWT is simply a OWT on a floating platform. The platforms can be divided into four main categories shown in Figure 1-1, based on their stabilising principle. The Spar platform is long cylinder-shaped, stabilised by ballast, to lower the centre of gravity. The semi-submersible platform is wider and more shallow, stabilised by buoyancy and weight. The barge platform is a simple floating buoy, being water-bed stabilised. Finally, the tension leg platform (TLP) is stabilised by mooring line tension. Each platform is designed such that it is least sensitive to disturbances. For most concepts, a regular wind turbine is placed on top of the floating platform.

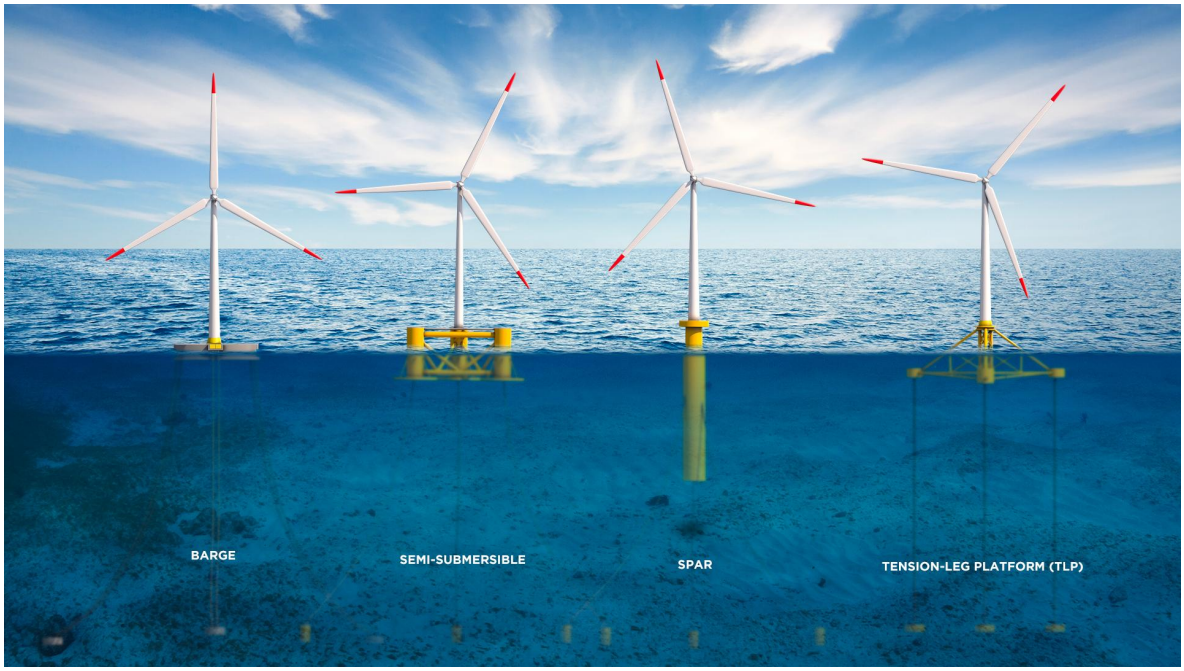

Figure 1-1: Four major categories of floating platforms [1].

The first full-scale FOWT prototype is Hywind [16]. The 2.3 MW spar-like platform was deployed in 2009. Since then, the development has gained a boost with the Windfloat Semi-submersible in 2011 [17]. Recently the first FOWT park named Hywind Scotland has been deployed [18] consisting of five turbines, rated on a total capacity of 30 MW. Several bigger projects are in the pipeline. According to Wind Europe [19], the technology of FOWTs has now reached the stage of 'system tests, launch and operations' on the technology readiness level (TRL) scale, being the final stage of development.

Investigating the control of FOWTs, the fundamental strategy is adapted from non-floating WT control. Each turbine has 2 control loops[1]. The blades pitching around their axis θ_c, regulating the horizontal aerodynamic thrust force F_{thrust} and aerodynamic rotor torque T. A baseline blade pitch controller consists of a proportional-integral (PI) structure, designed to reject variations in rotor speed Ω while operating in above-rated wind speed, using collective blade pitch θ_c control. Pitch control is thus mainly active in above-rated wind speeds (region 3), indicated in Figure 1-2. The second baseline controller is a non-linear generator torque τ_g controller. This controller is also regulating the rotor-speed Ω for optimal power production, but mainly active in below-rated wind speeds (region 2).

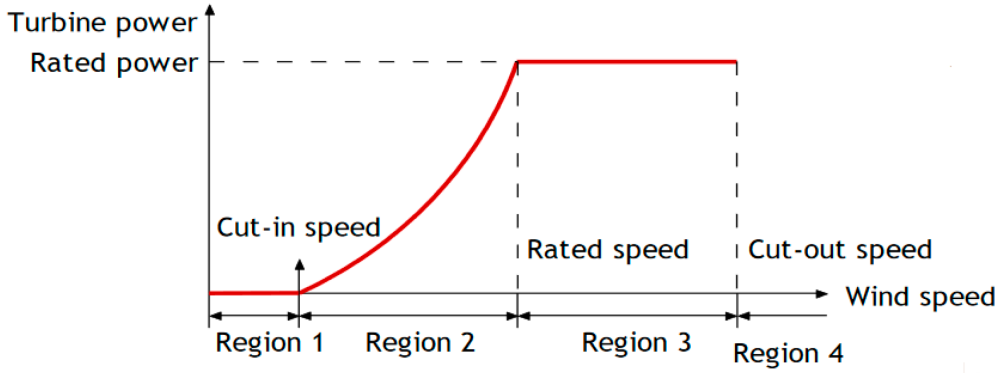

Figure 1-2: Typical wind turbine power curve as a function of wind speed. Turbine starts rotating (cut-in speed), reaches maximum power (rated speed) and goes in survival mode (cut-out speed) [2].

Both controllers are tuned such that $P = \Omega \cdot \tau_g \cdot N$ provides optimal power production in steady-state, where N is the drive-train gear ratio. A control scheme of the whole is provided in Figure 1-3. Note that both baseline controller loops are nearly decoupled, as their operating regions are separate.

1-2 Control challenges in floating offshore wind turbines

The full-scale tests demonstrate that FOWTs are already feasible, from a technical perspective. It is even argued that FOWTs have the potential to produce energy at a lower or equal cost compared to OWTs. Why then, are FOWTs then not already being deployed on a large scale, similar to fixed-bottom WTs? The reason is that FOWTs are not yet economically feasible, due to two main reasons [20]. First, FOWTs are relatively new, and the scale at which deployment is taking place is still minor. Thus, cost-effective mass production is not yet in place. Resolving this challenge is merely a matter of economic market force and is considered as a matter of time. The second cause is that replacing the fixed foundation by a floating platform induces rigid body dynamics, additional to the existing structural dynamics. These lead to undesired motions and thus additional engineering challenges. A stabilising mechanical system has to be developed, considering the fully coupled aero-hydro-servo-elastic non-linear dynamics. At the same time, a modified stabilising controller has to be developed.

[1] Control of the yaw direction and individual blade pitch control is not taken into consideration.

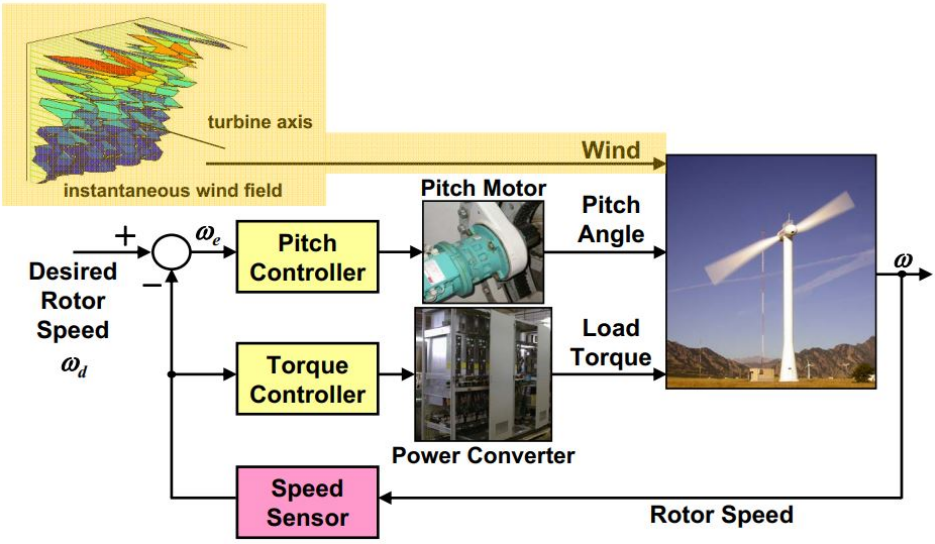

Figure 1-3: Baseline control scheme: independent SISO pitch control and torque control. Wind as the only disturbance input. [3]

Control is effecting all dynamics and loads. Thereby, control influences the power production and life-time of the FOWT. Better controllers may reduce the effect of disturbances and increase the life-time.

The first control-challenge is to keep the FOWTs as stable as possible [20]. Motions of the rotor nacelle assembly (RNA) will intensify the design requirements, since the design has to be more robust to inclination angles and nacelle acceleration. Motions of the platform increase the loads on the mooring lines. Tower-top motions will lead to a relative wind speed v_r, as defined in Eq. (1-1). Relative wind speed variations lead to additional rotor speed variations, thus power variations. Section 3-1 will elaborate on this effect.

$$v_r = v_0 - \dot{x}_t \tag{1-1}$$

The second challenge when adapting the FB controller from a non-floating WT, is the so-called negative damping problem (NDP) [5]. Considering the linearized system, two non-minimum phase zeros are found in the complex right-half plane (RHP), as seen in Figure 1-4. Therefore, closed-loop pitch control with a high gain can lead to instability[2], as illustrated in Figure 1-5. A solution to this problem is tuning down the controller gains to stable values, however, this is at the expense of fast disturbance rejection. Additional control methods should be researched.

The third control challenge is how to handle external disturbance signals. Waves and wind constantly apply varying forces on the FOWT. These are the driving force of any dynamics and loads. The wind speed is measured on top of the RNA. However, due to placement *behind* the rotor and rotor-caused turbulence, these measurements are not usable for control. Waves are not being measured on board. The wind turbine has no preview about what is going to happen in the future and is essentially 'blind' to disturbances.

[2] In the above-rated region

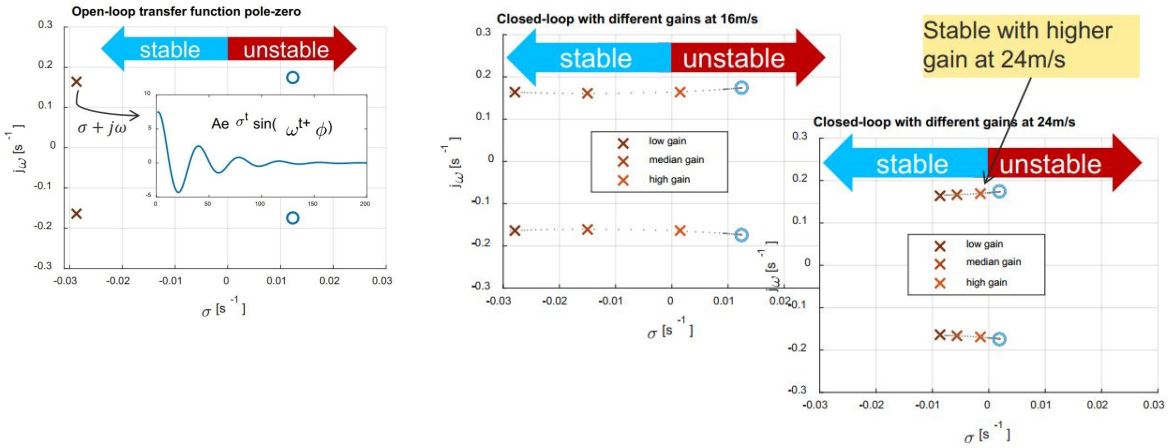

(a) OL pole-zero map. Two LHP (stable) poles and two RHP non-minimum phase zeros can be observed.

(b) CL root-locus plot. The poles move towards the RHP when increasing the controller gain. Leads to instability in the $16m/s$ case using high gain.

Figure 1-4: Linearised pole-zero map of the blade-pitch to the rotor-speed [4], indicating to the NDP [5].

The field of FOWT control can be considered as relatively young. Many of the control strategies originate from non-floating WT control. Many novel promising control concepts are currently being developed. Considering this current stage of development, it is important to explore the potential of new concepts, rather than exploiting existing ones.

1-3 Research motivation: effectiveness of feedback control is limited

Current research addresses the challenges primarily by developing more advanced FB control strategies. Advanced single-input single-output (SISO) control strategies, such as individual blade pitch control [21], gain scheduling [22] or reset control [23], can enhance performance. However, SISO control does not increase the performance enough. multi-input multi-output (MIMO) control has shown exceptional performance, but publications on the topic are limited. For example, MIMO H_∞ control is showing excellent performance on non-floating WTs [24], but extension to FOWTs is rare. non-linear model predictive control (NMPC) has shown exceptionally high-performance [25] by using a non-linear model of the FOWT and accommodating wind and wave previews into the control signal. However, solving the NMPC problem is computationally too complex to implement in real-time. The authors suggest to learn from its behaviour and consider it as an upper limit for FOWT control.

As for all state-of-the-art control strategies, only very few have been implemented. A novel feedback controller requires major changes to the control loop. The wind-industry is reluctant to implement major changes in the feedback loop, in order to maintain simplicity and the need to meet the regulatory requirements. As a result, many promising FB control strategies remain unused. To contribute to the field of FOWTs, a novel strategy should be of low

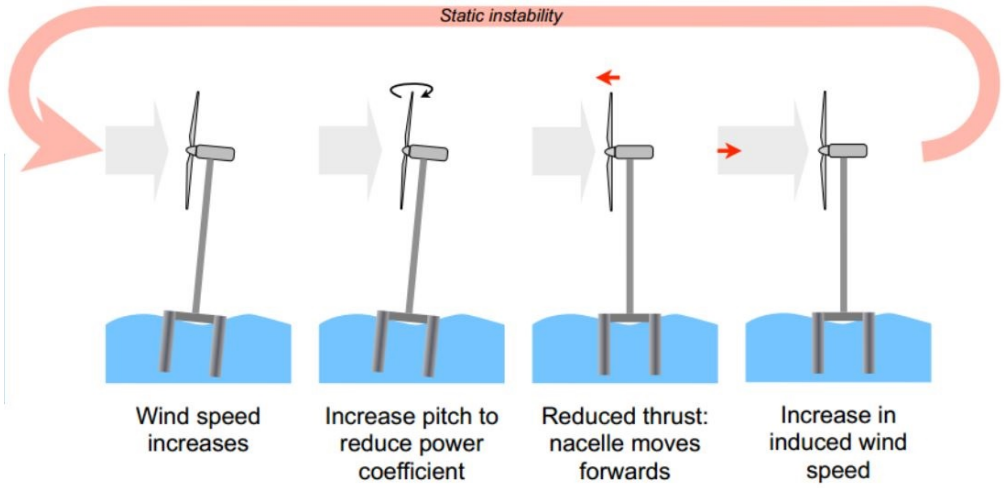

Figure 1-5: Effect of a disturbance using a regular fixed-bottom WT controller on a FOWT. The FOWT becomes unstable. [5]

complexity.

disturbance accommodating control (DAC) [26] accommodates a measurement of the disturbance into the control signal. A currently promising application is LIDAR[3] assisted FF control [27]. A LIDAR measures the average speed of incoming wind particles and utilises it to construct a control signal to compensate for wind speed variations. A stable FF controller receiving a stable input signal cannot make a stable system unstable [28]. Therefore, a stable designed FF controller does not effect the system stability. Moreover, FF is inherently faster then FB control, because it prevents disturbed dynamics rather than recover from them. A FB controller can only reject an error, once the error is measurable. In certain situations, the performance of control systems can be enhanced greatly by the application of FF control. However, it requires an accurate model of the disturbance-effects and, for wind, obtaining the preview is currently difficult and costly.

Research on only the effect of wave accommodating control does not yet exist, by the best knowledge of the author. Relatively to wind-FF, wave-FF seems more simple. Measuring waves is a well-known technology [29]. For example, wave-buoys or radar systems [30] may be used. Such systems are of relatively low cost. Using radar, a wave preview of more than 60 seconds in advance is obtained. Moreover, wave propagation is primarily deterministic, whereas wind propagation requires the frozen turbulence assumption [31]. Finally, recent findings provide a methodology to obtain a parametric wave excitation model from non-parametric simulation data [32], such that wave excitation forces can efficiently be estimated from measured surface elevations.

[3]light detection and ranging (LIDAR)

1-4 Research objective: identify the potential of wave-FF control

It is essential to equip the new generation wind turbines with disturbance estimators, such that they are not blind to external excitations. **The objective of this work is to identify the effect of wave excitations on FOWTs and develop a controller such that it can be compensated without compromising on energy capture or controller complexity.** If this method proves valuable, showing significant performance increases, further research can be conducted towards its practical implementation[4]. However, this study is primarily about exploring potential rather than exploiting it.
Because this work is proposing a realistic alternative to advanced control strategies, special focus is being laid to realistic industry implementation. To maintain the properties of the FB controller, the idea is to create a modular framework acting independently of the FB controller. By doing so, it can complement any arbitrary (advanced) FB controller, such that the improvements add up.

The methodology to obtain the objective consists of several steps. A case study is applied on the DTU 10MW reference wind turbine using the SWE TripleSpar floating platform. The effect of waves on TripleSpar is determined using high-fidelity simulations, comparing the performance in seven different load cases. Each load case is simulated twice, in waves and in still water. Dynamic responses dominated by waves will stand out in the comparison.
The FF controller presented in this work is based on a linear model to capture the FOWT dynamics using the surface elevations. Special care is given to obtain a parametric model of the wave forces and a realistic (future) wave preview.
Linear analysis is used to determine the effectiveness of control inputs and provides an understanding of the (wave) disturbance sensitivity. A FF controller is formulated based on linear model inversion and it is added to the standard wind turbine FB controller. Again, similar high-fidelity simulations are carried out to determine the effectiveness of the novel controller. Performance of the FB+FF controller is compared to regular baseline FB control.

1-5 Report outline

The outline of this report is briefly in Figure 1-6. The purpose of the chapter is indicated together with the main question being addressed. In Chapter 2, the impact of waves on FOWTs is studied. A ROM description of the FOWT is obtained to simplify the analysis. A simulation configuration is derived, where performance for *wind in still water* is compared to performance in *wind and waves*. Several standardised load cases with an increasing intensity are studied. The wave-induced performance differences and frequency response are discussed. Hereby, the problem which wave-FF attempts to improve is identified.

In Chapter 3, a thorough foundation for the understanding of the system is presented. The first principles of the ROM are identified. Then, a CROLM in state-space form is obtained. This model will allow linear analysis and linear model-based control. It consists of the free-floating body dynamics, a parametric WEM and an analytical wave prediction function.

In Chapter 4, the controller is designed and verified on the linear model. The previous analysis and linear model are utilised to design a wave-FF controller that has a good rejection of wave-

[4]If the method proves non-valuable, further research towards practical implementation is not relevant.

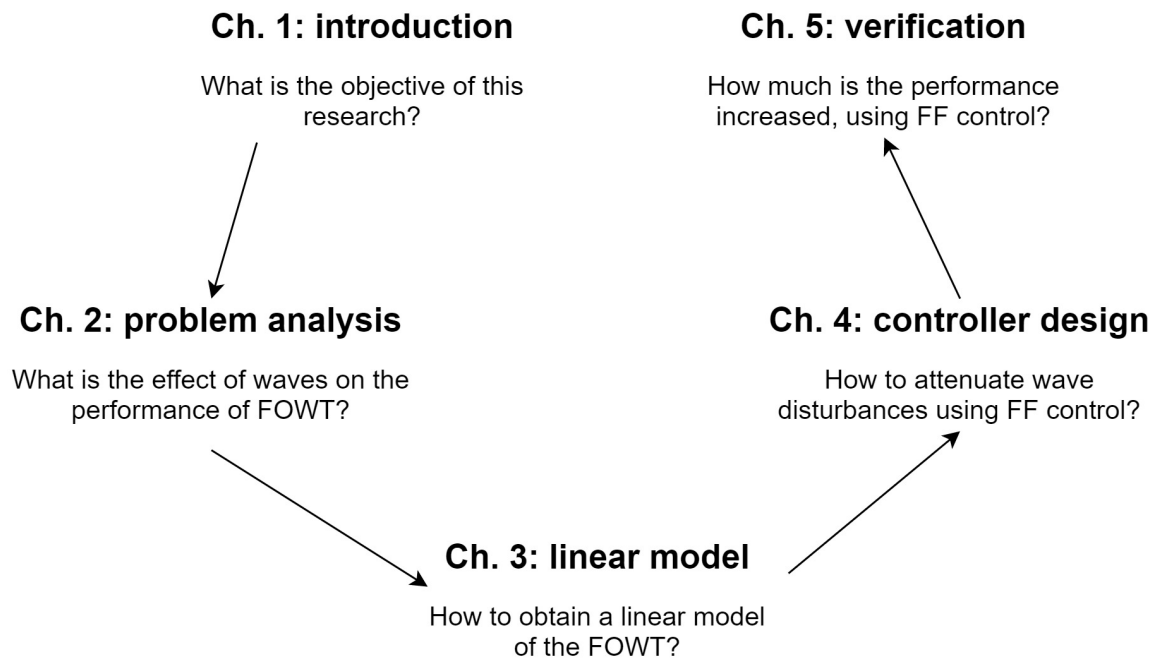

Figure 1-6: Outline of the report, described by the function of the chapter and the main question being anwserd.

induced disturbances. The linear model is used to apply linear analysis. The control logic is derived and a controller is designed. Ultimately, a generalised design procedure is presented, such that the work can be extended to any arbitrary platform or control objective.

In Chapter 5, the controller is subjected to high-fidelity simulations. The wave-FF controller is again exposed to the seven load cases, similar as in Chapter 2. The overall performance and frequency responses are compared with the baseline controller and the still water case, to measure the performance improvements. Moreover, scaled experiments have been conducted in a wave at MARIN. The results of the experiments are discussed in this chapter.

Ultimately, the significance and the implications of this work is evaluated with respect to existing research in the Discussion.

Chapter 2

Problem analysis: the impact of waves

Waves are one of the two primary external disturbances acting on the FOWT. The concept of wave-FF control is to reject wave-induced disturbances, using prior wave-knowledge. However, it is not known what these wave-induced disturbances are. In this chapter, the impact of waves is examined using high-fidelity simulations. Moreover, the configuration of a case-study is defined. A simulation software package, named FAST[1], is developed by NREL to simulate coupled dynamics responses for (floating) wind turbines. The aim of the simulations is to understand and quantify the influence of waves on different outputs and frequencies. The results will help to determine a control objective for the wave-FF controller.

The outline is as follows. The reference FOWT used in this work is described in Section 2-1. In Section 2-2, a ROM description is obtained. Two configurations are modelled in Section 2-3. One is with wind and waves, one is with wind in still water. Then, the general control objectives of FOWTs are defined in Section 2-4. Moreover, a set of load cases is determined, on which the performance is measured. In Section 2-5, the FOWT is simulated for each load case to study dynamic responses and load differences induced by waves. In Section 2-6, the time- and frequency response data is compared. This information should help to understand the effect of waves on FOWTs.

2-1 Definition of the 10MW TripleSpar reference wind turbine

Since the objective is to minimise wave-induced performance loss, it is reasonable to research a well-developed platform that is most sensitive to waves. The barge platform is such a platform [20]. It is superior in low production cost and complexity but has trouble with rejecting wave disturbances since it is waterbed-stabilised [33]. Its sensitivity to wave loading will increase the dynamic responses of the system. Moreover, the spar and the semi-submersible platforms are both moderately sensitive to waves and the TLP is least sensitive to waves.

Although a barge platform is argued to show the greatest improvements, the *DTU 10MW reference wind turbine on the SWE TripleSpar platform* [6] is selected for further analysis,

[1] fatigue, aerodynamics, structures, and turbulence (FAST)

illustrated in Figure 2-1. This decision is made merely from a practical perspective. Chapter 3 will point out that, only for this platform, a linearization [34] and linear system analysis [35] are available. Using the TripleSpar, this research can build on an existing linearized model. Nonetheless, it can be argued that any improvements found on the medium wave-sensitive TripleSpar, are even greater on the very wave-sensitive barge platform.

Table 2-1: The DTU 10 MW reference wind turbine design summary [6]

Description	Value
Rated power	10 MW
Rotor orientation, configuration	Upwind, 3 bladed
Baseline control	Variable speed, collective pitch
Drive train	Medium speed, multiple stage gearbox
Rotor, hub diameter	178.3m, 5.6m
Hub height	119m
Cut-in, rated, cut-out wind speed	4m/s, 11.4m/s, 25m/s
Cut-in, rated rotor speed	6RPM, 9.6RPM
Rated tip speed	90m/s
Overhang, shaft tilt, pre-cone	7.07m, 5°, 2.5°
Pre-bend	3m
Rotor-mass	229 tons (≈41 tons per blade)
Nacelle mass	446 tons
Tower mass	605 tons

The most important properties of the TripleSpar are listed in Tab. 2-1. The reference baseline-controller is the basic DTU wind energy controller [36]. It consists of below-rated torque control, an above-rated pitch-controller for stable rotor speed and an above-rated pitch-controller for stable power production.

2-2 Reduced order model description

The dynamics in all degrees of freedom (DOF) can be properly simulated in FAST. However, such a model is very difficult to interpret and the simulation is very time-consuming because of high computational complexity. Albert Einstein stated: “Everything should be made as simple as possible, but not simpler”. The objective of this section is to derive an accurate, simple and efficient simulation configuration that can be used throughout the rest of this study. Therefore, a ROM is obtained. All simplifications will be described throughout the following subsections, together with their implications.

Degrees of freedom

The FOWT will be considered in a 2-dimensional space. It is found that heave motions (i.e. upwards directed) are nearly fully decoupled [35] from the other dynamics. Therefore, we assume that the heave motions (z_p) exactly follow the surface elevation, such that heave can be neglected. The DOF that are considered in the ROM are presented in Fig. 2-1, drawn in black. It considers the platform translational surge displacement x_p, the platform rotational

pitch angle β_p, the rotor azimuth angle φ and the fore-aft tower deflection x_d. Moreover, the COF and centre of mass (COM) are indicated.

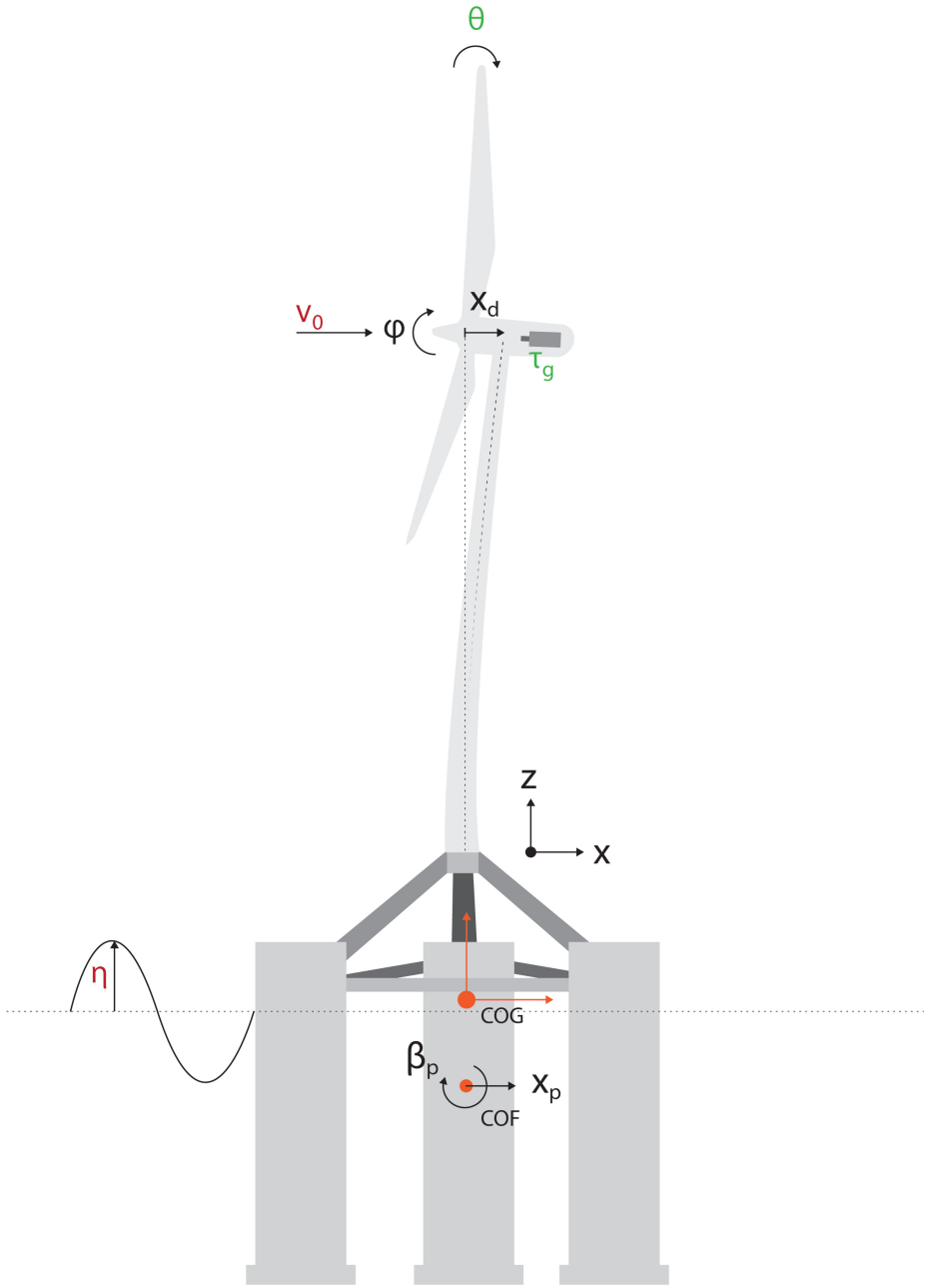

Figure 2-1: Considered degrees of freedom of the reduced order model, including the control inputs (green) and disturbance inputs (red).

The configuration vector $\boldsymbol{q}$ of the ROM is represented in Eq. (2-1). It consists of 3 rigid body DOF $\boldsymbol{q}_r$ and one elastic $\boldsymbol{q}_e$. The platform DOF can be collected in $\boldsymbol{q}_p$. Note that Ω is used to denote the rotor speed.

$$\begin{aligned} \textit{All: } \boldsymbol{q} &= \begin{bmatrix} x_p & \beta_p & \varphi & x_d \end{bmatrix} \\ \textit{Rigid body: } \boldsymbol{q}_r &= \begin{bmatrix} x_p & \beta_p & \varphi \end{bmatrix} \\ \textit{Platform: } \boldsymbol{q}_p &= \begin{bmatrix} x_p & \beta_p \end{bmatrix} \\ \textit{Elastic: } q_e &= \begin{bmatrix} x_d \end{bmatrix} \end{aligned} \tag{2-1}$$

To describe the state-space model, an 8^{th} order state vector $\mathbf{x}$ is obtained. It contains the configuration vector $\boldsymbol{q}$ and its derivative $\dot{\boldsymbol{q}}$, being $\boldsymbol{x} = [\boldsymbol{q},\ \dot{\boldsymbol{q}}]$.

$$\boldsymbol{x} = \begin{bmatrix} x_p, & \beta_p, & \varphi, & x_d, & \dot{x}_p, & \dot{\beta}_p, & \Omega, & \dot{x}_d \end{bmatrix}^T \tag{2-2}$$

The tower top speed (x_t) is considered to be an important measure because tower top speed leads directly to changes in relative wind speed, explained in Section 1-2. The tower top displacement can be written as a non-linear combination of multiple states.

$$x_t = x_p + x_d + L \cdot \cos \beta_p \tag{2-3}$$

This equation is linearized in Eq. (2-4). The linearization is valid for small pitch angles only. The tower top speed $\dot{x}_t$ and acceleration $\ddot{x}_t$ follow directly from differentiation.

$$x_t \approx x_p + x_d + L \cdot \beta_p \tag{2-4}$$

The ROM does not describe all FOWT dynamics. All elastic deformations, except that of the tower, are neglected. Also, dynamics in the y-direction are not taken into account. It is found that misaligned loads are leading to uncontrollable dynamics [8] and cannot be ignored. In-plane aligned loads (2 dimensional) have the largest effect on fatigue [37]. For decisive research, misalignment should also be considered. Yet, as this is a pilot study on the potential of wave-FF control, they are now not taken into account.

Control and disturbance inputs

The model is defined with four inputs, of which two are controllable and two are disturbances. The controllable inputs are the blade pitch angle θ_c and the electric generator torque τ_g, together $u = [\theta_c,\ \tau_g]$. The disturbance inputs are simplified to the absolute rotor-effective wind speed in x-direction v_0 and the surface elevation height η_0 at the origin of the platform, together $d = [v_o,\ \eta_0]$. It is found that first-order wave forces are related to the surface elevation, since there exist a linear time-invariant (LTI) relationship between the surface height η_0 and the first-order wave excitation forces $F^{we,1}$ [32]. Figure 2-1 shows how the control inputs θ_c and τ_g (green) and the disturbance inputs v_0 and η_0 (red) are added to the previously autonomous system.

Input-output model

To generalise the ROM in a control framework, the block diagram in Figure 2-2 is used for further analysis. C is the baseline controller, divided into C_{τ_g} and C_{θ_c}. The diagram shows how the waves η_0 and wind v_0 disturb the plant, while the controller is attempting to track Ω_{opt} using the blade pitch angle θ_c and generator torque τ_g. The output y can be any measurable state or combination of states. Moreover, the loads are also available in FAST. A method to measure the performance using the outputs is described in Section 2-4.

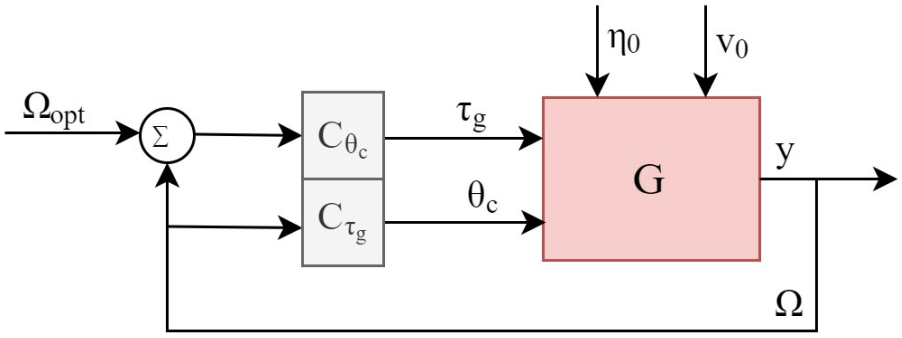

Figure 2-2: Input-output representation of the ROM.

2-3 Simulation configuration and load cases

The TripleSpar is simulated the in simulation software package FAST v8 [38]. Two configurations are simulated: one subjected wind disturbance in still water and one subjected to wind and wave disturbances. Both configurations are shown in Figure 2-3. The difference in performance is considered to be the consequence of wave-induced loads. The load cases as described later in this section will apply in order to measure performance.

A reference model of the TripleSpar with the corresponding baseline controller is used as a basis for simulation. The DOF are reduced according to the ROM. For each simulation, the setup is subjected to all seven load cases for 1200 seconds with a time-step of $T_s = 0.1$ s. Since the initial conditions of the FOWT are unknown, the first 600 seconds of the simulation is considered to be transient data. The following 600 seconds are used for the analysis.

The disturbances are pseudo-random, according to a spectrum in which they occur. For waves, the joint North Sea wave project (JONSWAP) [39] spectrum is used. This spectrum has approximately the same shape for any wind-wave condition. It scales according to the significant wave height H_s and significant period T_s. The spectrum is only non-zero between 3 to 20 seconds and may be presumed constant for a period of up to 30 minutes.
For wind, the turbulent Kaimal spectrum [40] is used. This spectrum is non-zero in the low-frequency range, starting from about 40 seconds period. An example of their power spectral density function is shown in figure 2-4. Disturbances as a result of the rotor passing the tower are in this analysis not taken into account as external system disturbance inputs. However, they are also simulated in FAST.

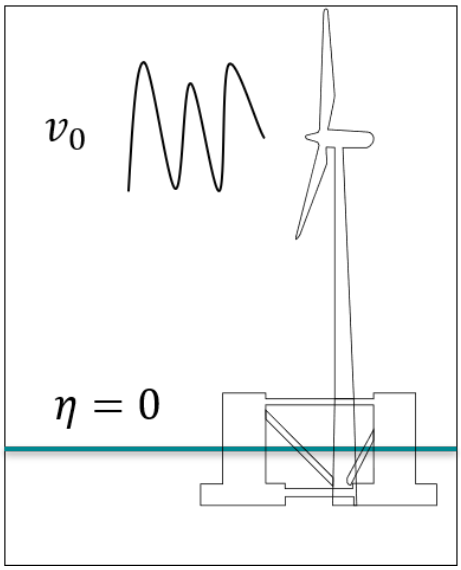

(a) Simulation configuration 1: wind in still water

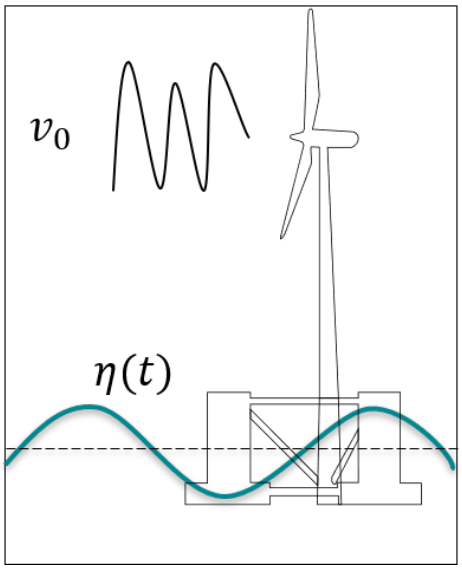

(b) Simulation configuration 2: wind and waves

Figure 2-3: Simulation configuration. Two test-cases to measure the effect of waves on FOWTs.

The performance of the FOWT with the controller is subjected to diverse oceanic sea states, i.e. load cases. Seven load cases are selected from [7] and presented in Tab. 2-2, ranging from calm weather conditions to extreme. Their probability of occurrence is indicated. Neglecting swell waves[2], a rough relation between wind and waves exist. These sea states will be used for simulation purposes, measuring the performance for each. A weighted sum is be obtained by using the Weibull average, weighing the performance of each load case to their corresponding occurrence probability p_i.

Table 2-2: Selection of oceanic states based on their occurrence probability based on Life 50+ [7]

	v_0 [m/s]	Hs [m]	Ts [s]	p [-]
Load case 1	5	1,4	7	14%
Load case 2	7,1	1,7	8	24%
Load case 3	10,3	2,2	8	26%
Load case 4	13,9	3	9,5	20%
Load case 5	17,9	4,3	10	11%
Load case 6	22,1	6,2	12,5	3.8%
Load case 7	25	8,3	12	0.74%
				$\approx 100\%$

[2]Swell waves are travelling waves, originated from some different wind field

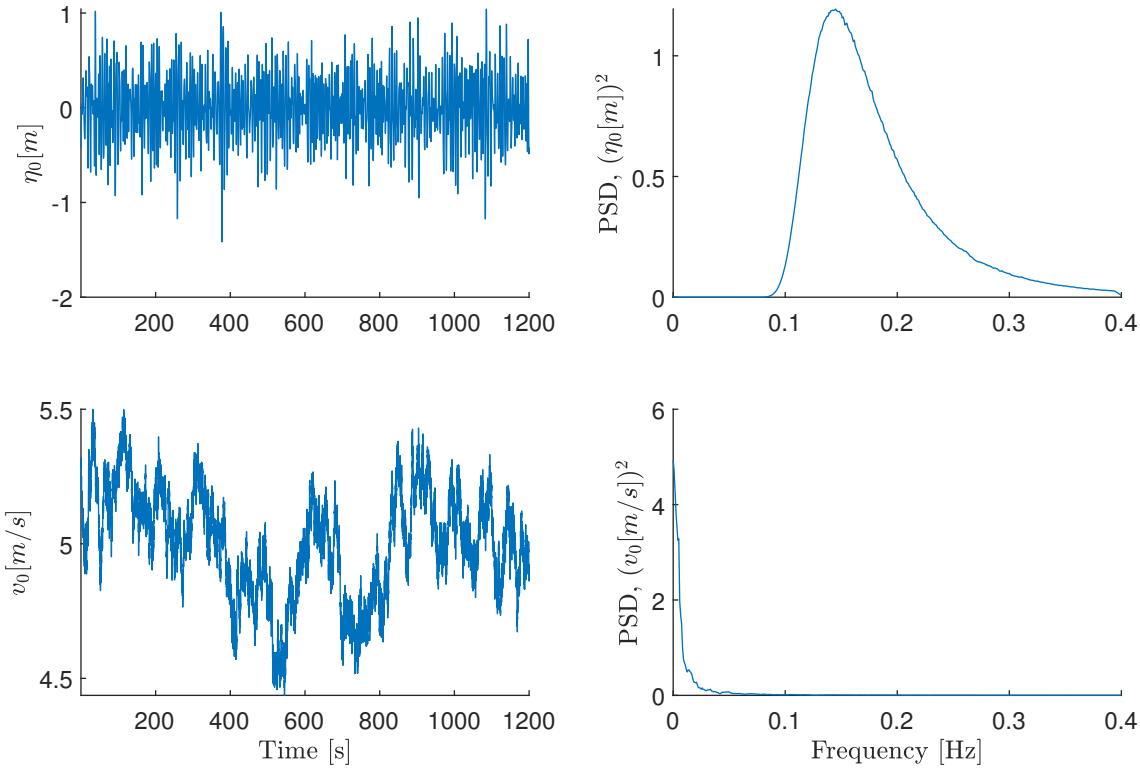

Figure 2-4: Sample disturbances v_0 and η_0 using load case 1. Left: time series. Right: power spectral density.

2-4 Control objectives

Since we want to compare different controller performances, a set of measurable performance indicators is obtained. For FOWTs there are two main control objectives, as defined by H. Namik et al. [41].

1. Maximum power production
2. Minimise power production variations
3. Minimum structural loads

More specifically, the objective is to obtain an optimal power production without causing high static loads, load cycles or bearing wear by blade pitch motion [42]. The performance indicators as used throughout this work are shown in Tab 2-3 and described in the following paragraphs.

For power stability, the objective can be divided into multiple sub-objectives. To obtain effective power production, tracking of the optimal rotor-speed $\Omega_{err} = \Omega - \Omega_{opt}$ is desired, together with high generator torque values τ_g. Multiple approaches exist to obtain rotor-speed tracking. For example, a reduction of rotor speed tracking errors (Ω_{err}) *can* be obtained by

reducing the tower top motions ($\dot{x}_t$). However, since minimum rotor speed variation can also be obtained by alternative methods, minimising tower top motions is not a holistic approach and is not included in the performance indicators. The same thinking applies for platform pitch (β_p) and platform surge (x_p). In other words, only the ultimate objectives are measured.

The structural loads and load cycles are taken into account as follows. By reducing structural loads, longer lifetime and hence longer power production is obtained. The tower bending moment ($M_{y,T}$), blade out of plane (OOP) moment ($M_{b,oop}$) and low-speed shaft (LSS) rotational moment (M_{LSS}) are considered to be the most critical loads. The damage equivalent load (DEL) will be used as a measure of fatigue damage. *MLife* [43] is used to calculate the DEL from a time series, using Eq. (2-5). The result is a 1 Hz-fatigue-equivalent load. For this equation, the following frequency domain data is used. Each cyclic load $b = 1..N$ is occurring $N_{cyc,b}$ times with an intensity of $M_{y,b}$

$$DEL(M(t)) = \frac{\sum_{b=1}^{N} N_{cyc,b} \cdot M_{y,b}}{N_{cyc,1Hz}} \tag{2-5}$$

Furthermore, wear is taken into account. The industry stresses that blade-pitch control action should be reduced to reduce bearing wear. Therefore, the mean collective-pitch control action is taken into account. The mean travelled angle per second is measured as ($|\dot{\theta}_c|$) and should be minimised.

Table 2-3: Peformance indicators

Performance objectives				
#	**Objective**		**Label**	**Motivation, enhances:**
	Stable power production			
1.1	$maximise\ mean(P)$	$[MW]$	Power production	Energy production
1.2	$minimise\ var(\Omega - \Omega_{opt})$	$[RPM]$	Rotor error	Energy stability
	Load reduction			
2.1	$minimise\ DEL(M_{y,T})$	$[kNm]$	DEL tower	Tower durability
2.2	$minimise\ DEL(M_{lss})$	$[kNm]$	DEL shaft	Low speed shaft durability
2.3	$minimise\ DEL(M_{b,oop})$	$[kNm]$	DEL blade	Blade durability
2.4	$minimise\ mean(\|\dot{\theta}_c\|)$	$[rad/s]$	Blade angle distance	Pitch-bearing durability

Alongside performance objectives, performance limits are considered. Table 2-4 shows the established limits on performance. The power P is limited to protect the electric system. The rotor speed is upper-bound to limit vibrations in the blades, caused by high blade-tip speeds. The generator torque τ_g is upper-bound to protect the electronic system. The pitch angle β_p of the tower is limited, to maintain stability and keep the RNA horizontal. The tower-top acceleration $\ddot{x}_t$ is upper-limited to prevent RNA inertia forces from becoming too high. Finally, the tower bending moment $M_{y,T}$ and LSS moment (M_{LSS}) are upper-bounded to protect against static material failure. In this work, the maximum values are not quantified. Benchmark maximum values do not yet exist for the TripleSpar. However, attention is given such that they do not exceed unrealistic values, compared to baseline control.

Table 2-4: Performance requirements

Performance constraints		
Constrain	**Constrain label**	**Motivation**
$P < P_{max}$	Power	Prevent overrated power
$\Omega < \Omega_{max}$	Rotor speed	Prevent vibrations and overrated power
$\tau_g < \tau_{G,max}$	Generator torque	Protects generator electronics
$\beta_p < \beta_{p,max}$	Platform pitch angle	Maintain stability
$\ddot{x}_{TT} < a_{max}$	Tower-top acceleration	Protects against inertia forces
$M_{y,T} < M_{y,T,max}$	Tower base load	Protects against static material failure
$M_{LSS} < M_{LSS,max}$	LSS load	Protects against static material failure

2-5 High-fidelity simulation results

Waves acting on a FOWT cause dynamic oscillations and additional structural loads. The total wave-induced performance loss is equivalent to the maximum possible performance improvement, that can be obtained by using wave-FF. In other words, still-water performance is considered to be an upper-limit for wave-FF. Furthermore, the difference in performance will provide insight into the most relevant control objectives for wave-FF. Therefore, the goal of this section is to identify the performance difference between wind-wave conditions, and wind-still-water conditions for the TripleSpar in all load cases.

The effect of waves on the TripleSpar is indicated in Figure 2-5, by a ratio of the decreased performance. For example, the tower DEL is increased about 10 times as a result of waves in load case one (DEL tower, first blue bar). Using the Weibull distribution, a weighted average is obtained based on the occurrence of each load case. Table 2-5 summarised the Weibull weighted values.

The results demonstrate how particularly the tower DEL and the blade pitch action increase as a result of waves. Moreover, the rotor speed variations, blade DEL and shaft DEL are moderately increased. The power production is reduced a little. To obtain more understanding in these increments, one can analyse the time series and power spectral density plots of the performance signals. This is the subject of the next section.

Waves appear most influential in calm (load case 1 and 2) and heavy sea states (case 5, 6 and 7) while being less influential in middle load cases (e.g. 3 and 4). We observe a sort of v-shape in performance, moving from calm to heavy. This applies for all measures, except the mean power[3]. A plausible explanation of the v-shape in performance is found in the thrust force graph in Figure 2-6, showing an inverted v-shape as a function of wind speed. The thrust force is strongest at load case 3 while being weakest in load case 1 and 7. Consequently, the wind is most dominant around rated rotor speed (case 3) while waves are more dominant away from rated rotor speed (load cases 1, 2, 6 and 7).

[3]For mean blade speed, load case 1, 2 and 3 are missing, since only generator torque control is present.

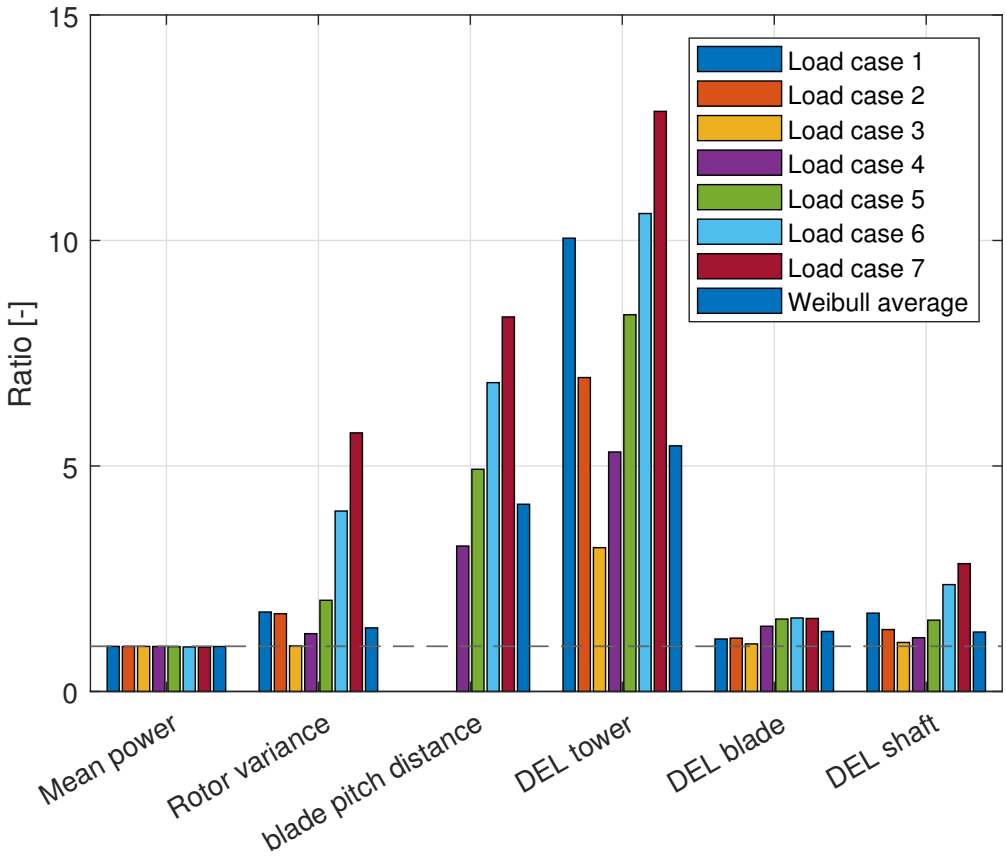

Figure 2-5: Performance difference as a result of waves, for each load cases.

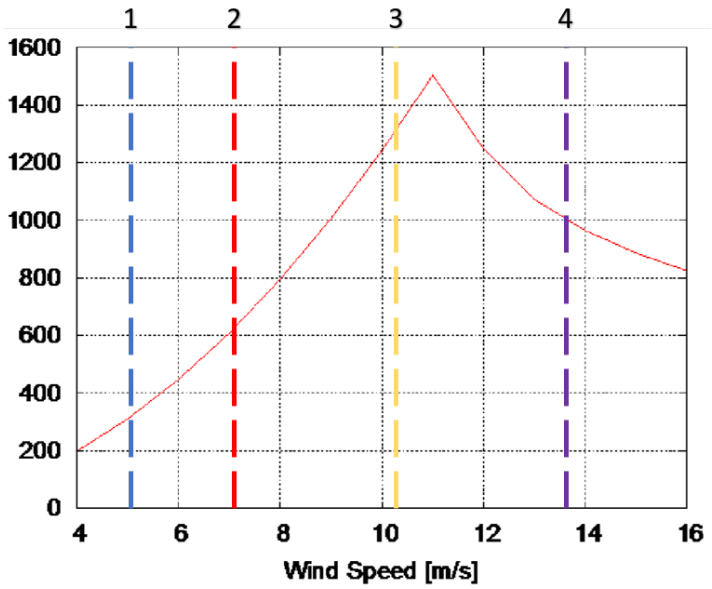

Figure 2-6: Steady-state thrust force as a function of wind speed for the 10MW DTU reference turbine [6]. The corresponding load cases are added to the plot.

Table 2-5: Weibull weighted performance increment as a result of waves.

Performance indicator	Incremental ratio [-]
$mean(P)$	0.997
$var(\|\Omega\|)$	1.4
$mean(\|\dot{\theta_c}\|)$	4.2
$DEL(M_{y,T})$	5.4
$DEL(M_{b,oop})$	1.3
$DEL(M_{lss})$	1.3

2-6 Frequency-domain analysis

By analysing the time series and PSD[4], some of the performance differences can be explained. Figure 2-7 shows the effect of waves on the dynamics. The first two rows show the wave and wind spectra. The third row is the generator torque control input τ_g. The last two rows indicate the rotor- and power variations. On the left is the time series of the simulation, on the right the PSD. Furthermore, the natural frequencies of the TripleSpar are indicated.

The same result is observed in every load case[5]. In the time series (left), the mean values are similar. The PSD-plot confirms this. The low frequent (wind-induced) part is similar, while a high-frequent wave-induced part is added. In the time-series, we see this high-frequency oscillation. Two small peaks are distinguished, at 0.18 Hz and 0.125 Hz. These peaks are found at the same location in all load cases. The oscillations are strongest in wave-sensitive load cases, such as load case 1 or 7.

[4]The PSD is a measure of power for each frequency in the simulation

[5]To simplify the analysis, only load case 2 is illustrated. However, the effect is the same and the intensity scales with the wave-dominance, described in the previous section.

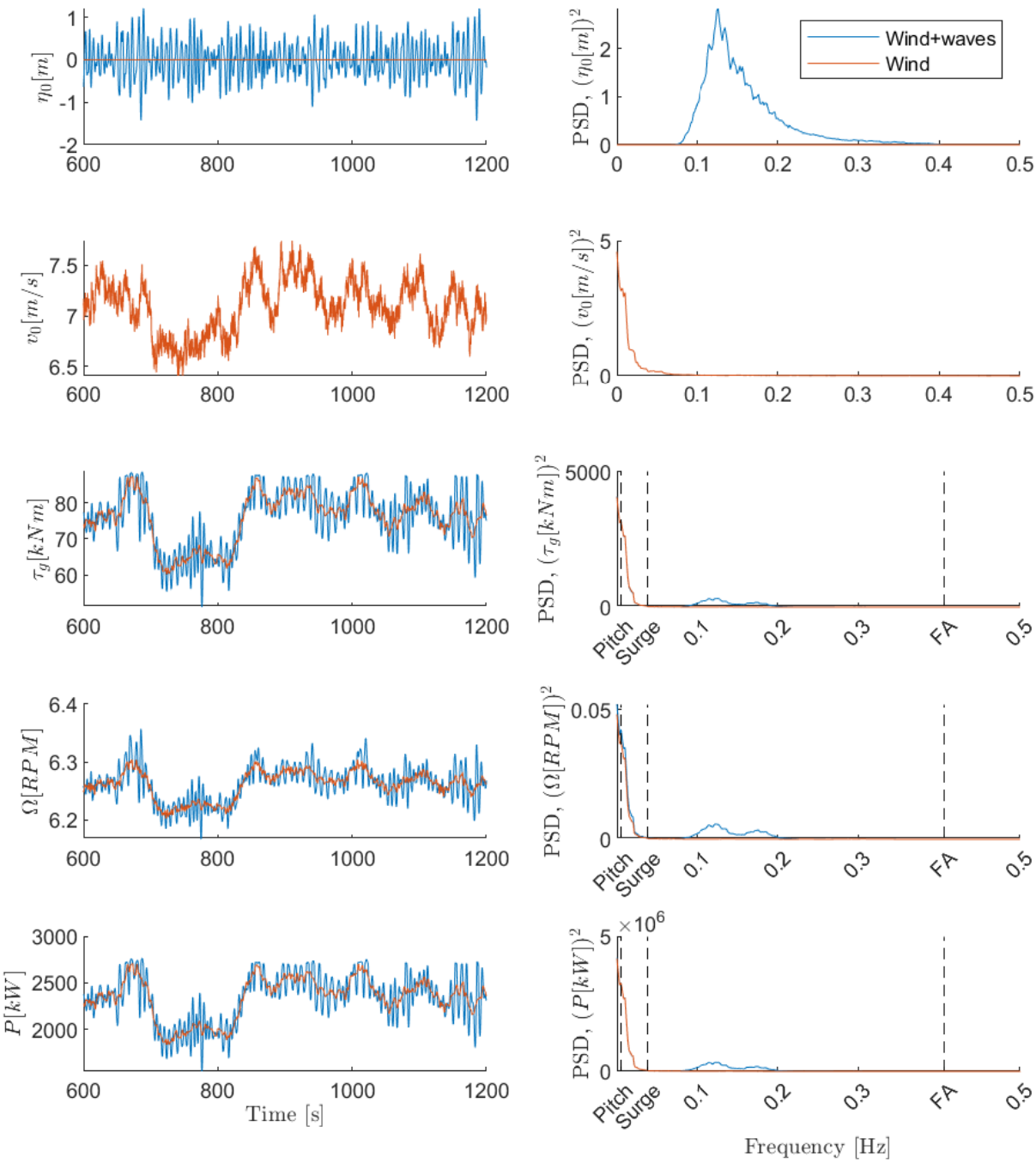

Figure 2-7: The effect of waves on the TripleSpar dynamics, using below-rated load case 2 with $\bar{v}_0 = 7.1 m/s$. Left is the time series, right the power spectral density.

Figure 2-8 shows the same plot for the derivative of the outputs. The plot shows a huge dominance of waves on dynamic motions. This implies that waves are dominant on variations of dynamics, whereas wind is dominant on mean values. The motions are now clearly in the frequency range of the wave spectrum. Also, the two peaks on 0.125 Hz and 0.18 Hz are more clear. The large difference with the previous result is likely caused by the amplification of high-frequencies that occur with a derivation.

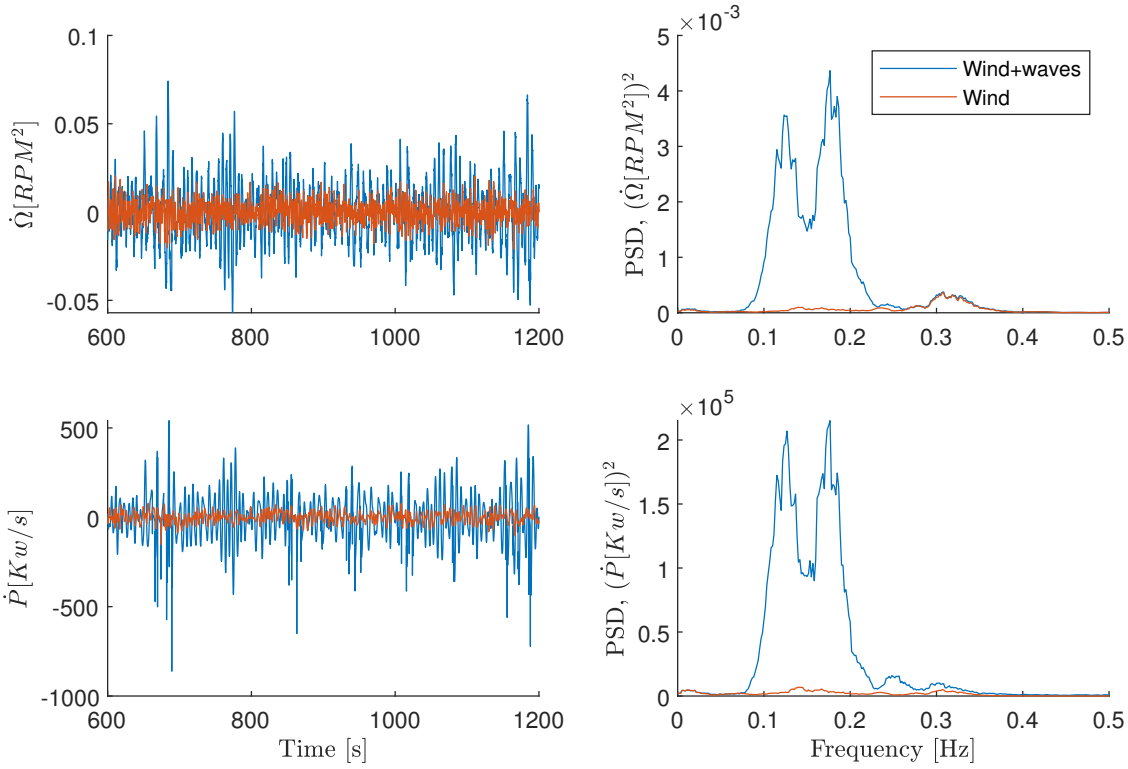

Figure 2-8: The effect of waves on TripleSpar dynamic output derivative, using below-rated load case 2 with $\bar{v}_0 = 7.1m/s$. Left is the time series, right the power spectral density.

Now, consider the wave-induced loads in Figure 2-9. Loads on the tower base $M_{y,T}$ are hugely dominated by waves, even without considering the derivative. These high-frequent load cycles are a driving force of fatigue. Looking at the blade bending moment $M_{y,oop}$, one large peak is found at $\approx 0.105Hz$. This is the result of the blade passing the tower (i.e. 1P load). The plot shows how waves are barely influencing the blade bending moment. The third row shows the rotational torque on the rotor LSS M_{LSS}. Again, the wind is dominant in the low-frequency range while waves induce a high-frequent oscillation. The oscillations of M_{LSS} are directly caused by the generator torque action τ_g.

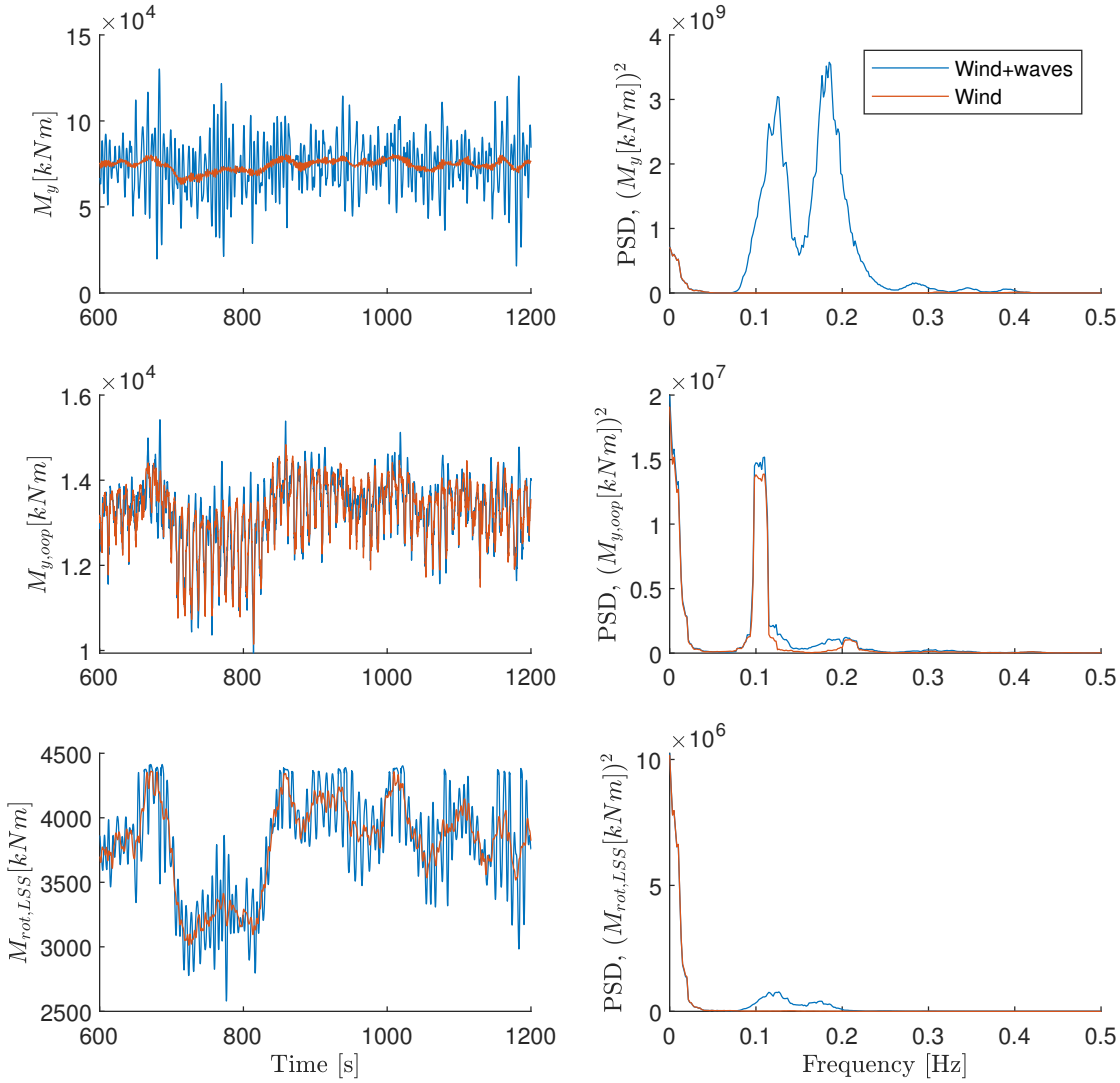

Figure 2-9: The effect of waves on structural loads, using below-rated load case 2 with $\bar{v}_0 = 7.1m/s$. Left is the time series, right the power spectral density.

2-7 Summary

In this chapter, a thorough understanding of the effect of waves is obtained using high-fidelity simulations. A two-dimensional ROM description is obtained in order to simplify the analysis, considering the surge, pitch, rotor and fore-aft dynamics. Each simulation is subjected to a set of 7 load cases, ranging from calm to extreme weather condition. The main control objectives are to obtain maximum power production with minimum structural loads and minimum power variation.

To identify the effect of waves, simulations on wind-wave conditions are compared to similar simulations without waves. Summarising the results, it is found that waves are dominant on tower-base load cycles (440% extra fatigue damage) and blade-pitch control-actions (420% more control action) the most. Furthermore, waves have a moderate effect on rotor speed variance (42%), blade-fatigue (30%) and LSS fatigue (30%). Waves have little effect on mean power production (-0.3%).

Waves particularly influence the high-frequency responses, derivatives of dynamics and load cycles. Therefore, wave-effects are dominant on dynamic accelerations. Moreover, it is found that the wave-impact is strongest in the calm and extreme load cases since the rotor thrust force is relatively lowest here. The performance in still water sets an upper limit for wave-FF control.

By also considering the control objectives, the analysis implies that tower-base fatigue, blade pitch control action and rotor speed variations are the most important control objectives for a wave-FF controller. These performance metrics may potentially benefit the most.

Chapter 3

Obtaining a causal reduced-order linear model

The wind industry is heavily dependent on time-domain simulations for the analysis of WTs. Although time-simulations prove to be highly accurate by scaled experimental verification [44], they provide little insight into the underlying physics. To understand these underlying physics, a LTI model is obtained in this chapter. This allows the use of classical linear system analysis tools. Moreover, it allows model-based (FF) control.

Obtaining a linearization of a FOWT is not straight-forward. Currently, the linearization capabilities of FAST v8 only apply for non-floating WTs. The follow-up version (OpenFAST) is currently developing fully coupled linearization capabilities for FOWTs [45]. However, these capabilities are not published yet. The previous version (FAST v7) can linearise FOWTs, but only in still water. As a result, universities are developing their custom linear models, such as [34] named SLOW[1], or [46]. These models are not publicly accessible. Hence, the goal of this chapter is to obtain a LTI state-space approximation at each operating point, such that we can obtain quantitative insight into the dynamic behaviour of a FOWT and develop a model-based controller.

The outline of this chapter is illustrated by Figure 3-1. In Section 3-1, insight is provided into the first principles of FOWTs. The equations of motions are obtained and summarised visually. Section 3-2 introduces the aero-hydro-servo-elastic linearization obtained using SLOW. In Section 3-3, a parametric model for the WEM is obtained, to model wave forces as a function of surface elevations. It is found that the WEM in the current panel code, is non-causal. Therefore, a surface-elevation prediction method is developed in Section 3-4. All individual linearized sub-systems are coupled into a so-called CROLM in Section 3-5. For complete linear analysis, the baseline controllers are also linearized.

[1] simplified low-order wind turbine (SLOW)

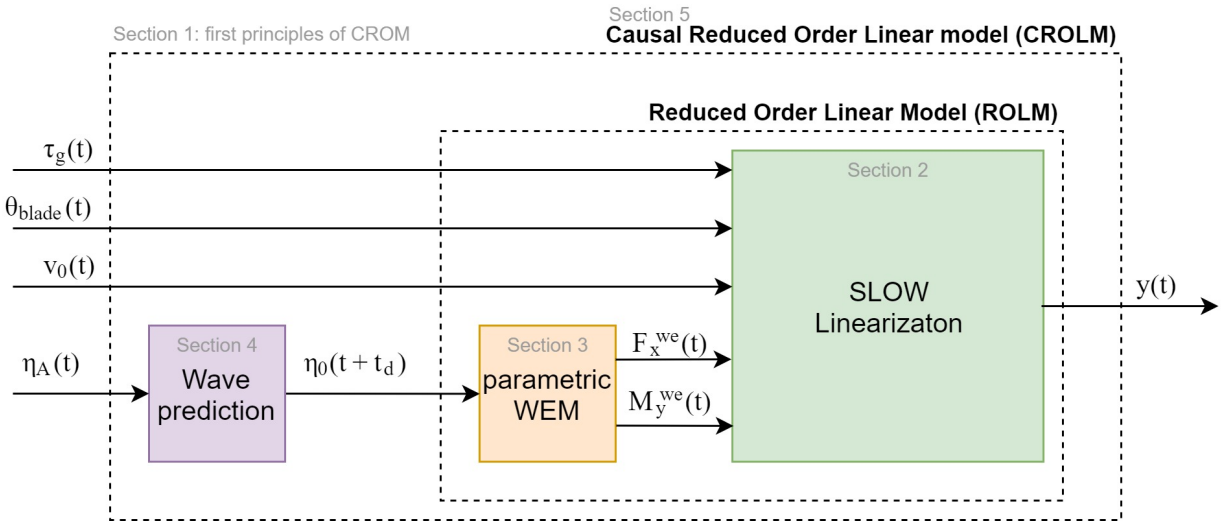

Figure 3-1: Composition of the CROLM model, consisting of all sub-modules from the previous sections. Also contains the outline of this chapter.

3-1 First principles analysis

The purpose of this section is to obtain an analytical understanding of the first principles of FOWTs, by establishing a set of differential equations for the ROM. The hydrodynamics, aerodynamics, servo-dynamics and structural dynamics are discussed and coupled into Eq. (3-1).

$$\ddot{\boldsymbol{q}} = \boldsymbol{P}(\dot{\boldsymbol{q}},\ \boldsymbol{q},\ \eta_0,\ v_0) \tag{3-1}$$

Using the principle of superposition, the loads are denoted in Eq. (3-2). Each load with $\boldsymbol{P}= [F_x,\ M_y,\ T]^T$ is described throughout the following sections. Here F_x is the surge force, M_y is the pitch moment, T is the rotor torque and M is the inertia matrix. Variables that are a function of time such as $q(t)$ are denoted simply as q, for readability reasons.

$$M\ddot{\boldsymbol{q}} = \boldsymbol{P}^{buoyancy} + \boldsymbol{P}^{gravity} + \boldsymbol{P}^{mooring} + \boldsymbol{P}^{added} + \boldsymbol{P}^{radiation} + \boldsymbol{P}^{we} + \boldsymbol{P}^{aero} \tag{3-2}$$

The internal loads $\boldsymbol{P}^{ext}$ and external loads $\boldsymbol{P}^{int}$ defined as Eq. (3-3) and Eq. (3-4). The freely floating body in still water is defined by $\boldsymbol{P}^{int} = 0$.

$$\boldsymbol{P}^{int} = M\ddot{\boldsymbol{q}} - (\boldsymbol{P}^{buoyancy} + \boldsymbol{P}^{gravity} + \boldsymbol{P}^{mooring} + \boldsymbol{P}^{added} + \boldsymbol{P}^{radiation}) \tag{3-3}$$

The external forces are obtained in Eq. (3-4).

$$\boldsymbol{P}^{ext} = \boldsymbol{P}^{we} + \boldsymbol{P}^{aero} \tag{3-4}$$

The internal and external loads are coupled by $\boldsymbol{P}^{int} = \boldsymbol{P}^{ext}$.

3-1-1 Free floating body

The first principles of the free-floating body are defined in this subsection, one by one.

Mooring lines: the mooring line force, i.e. restoring force, is well approximated by a hydrostatic restoring spring-like force with a restoring matrix C. The equation is as follows

$$\boldsymbol{P}_{mooring} = C \cdot \boldsymbol{q}_p \tag{3-5}$$

Rigid body motion: the rigid body DOF are defined in Eq. (3-6). Here $q_{r,i}$ is defined as the rigid body DOF in direction i, b_i is the rigid body damping coefficient and c_i is the mooring line restoring force.

$$\ddot{q}_{r,i} = \frac{1}{M_r}(-c_{ir,i} - b_i \dot{q}_{r,i}) \tag{3-6}$$

In matrix form, this equation is written as:

$$\ddot{\boldsymbol{q}}_r = \frac{1}{m}(-C\boldsymbol{q}_r - B\dot{\boldsymbol{q}}_r) \tag{3-7}$$

Rotor accelerations: the rotor accelerations $\dot{\Omega}$ are defined by Eq. (3-8). Here J is the rotor inertia and N the gear box rato.

$$\dot{\Omega} = \frac{1}{J}(T_{aero} - N \cdot \tau_g) \tag{3-8}$$

Buoyancy and gravity: these loads both work in the heave (z_p) direction. Since we assume that the FOWT follows the surface elevations, buoyancy and gravity cancel out.

$$\boldsymbol{P}^{gravity} + \boldsymbol{P}^{buoyancy} = 0 \tag{3-9}$$

Elastic tower deformation: the tower elastic fore-aft (FA) dynamics are approximated by Eq. (3-10), according to Euler-Bernoulli beam theory. Here m_{wt} is the turbine mass, E is the material elastic modulus, I the second moment of area, $\frac{L^3}{3EI}$ the average tower stiffness coefficient and b the elastic damping coefficient. This theory is valid for small deformations only.

$$\ddot{x}_d = \frac{1}{m_{wt}}(-\frac{L^3}{3EI}x_d - b\dot{x}_d) \tag{3-10}$$

Hydrodynamic radiation: waves interact with the FOWT in various ways. First, there are the externally caused oscillations in otherwise still water. This is called *radiation*. Moreover, wave-induced loads act on the floating body in an oscillating way. These are called wave excitation loads. Only small oscillations and waves will be considered, such that the responses may be assumed linear. Radiation forces are often described by a high-order transfer function, to simplify the problem. Equation (3-11) provides a frequency-dependent equation for the radiation force, where $B_{rad}(\omega)$ is the added viscous damping and $A_{rad}(\omega)$ the added mass by water. Moreover, ω denotes the angular frequency.

$$\boldsymbol{P}_{rad}(\dot{\boldsymbol{q}}, \ddot{\boldsymbol{q}}, \omega) = A_{rad}(\omega) \cdot \ddot{q}_p + B_{rad}(\omega) \cdot \dot{q}_p \tag{3-11}$$

A_{rad} is split into a frequency dependent part $A(\omega)$ and a non-frequency-dependent part A_∞. Often, $A(\omega)$ is also approximated by a parametric transfer function, to obtain higher computational efficiency.

$$A_{rad}(\omega) = A(\omega) + A_\infty \tag{3-12}$$

3-1-2 External loads

Aerodynamics: the aerodynamic rotor thrust force F_{thrust} is defined in Eq. (3-13). Here ρ_a is the air density coefficient, R is the rotor radius and $C_t(v_r, \theta)$ is the aerodynamic thrust coefficient. The latter is dependent on the relative wind speed v_r from Eq. (1-1) and the collective blade pitch angle θ_c.

$$F_{thrust} = \frac{1}{2}\rho_a \pi R^2 C_t(v_r, \theta_c) v_r^2 \tag{3-13}$$

The aerodynamic rotor torque T is defined in Eq. (3-14). Here $C_q(v_r, \theta_c)$ is the rotor torque coefficient, dependent on the relative wind speed v_r and the collective blade pitch angle θ_c.

$$T = \frac{1}{2}\rho A C_q(v_r, \theta_c) \cdot v_r^2 \tag{3-14}$$

Hydrodynamic wave-excitation loads: the wave-excitation loads are represented by Morison's equation. This equation is valid for long, slink cylindrical bodies. The TripleSpar can be described as being three slink cylinders. The first part of the equation defines the inertia forces of the moving water. The second part defines the drag force around the cylinder. The wave speed $u(z)$ is integrated over the height of the body z, since wave-speed is depth-dependent. Furthermore, the equation contains an added mass-coefficient c_M, the cylinder diameter D, the water density ρ, the drag coefficient c_D and the horizontal depth-dependent wave speed $u(z)$. The loads are tripled as there are three spars.

$$\begin{bmatrix} F_x \\ M_y \end{bmatrix} = \begin{bmatrix} 3\int_{z_{bot}}^{0} \left[\rho\frac{pi}{4}D^2(c_M+1)\dot{u}(z) + \frac{1}{2}\rho D c_D u(z)|u(z)|\right] dz \\ 3\int_{z_{bot}}^{0} \left[\underbrace{\rho\frac{pi}{4}D^2(c_M+1)\dot{u}(z)}_{interia} + \underbrace{\frac{1}{2}\rho D c_D u(z)|u(z)|}_{drag}\right] z dz \end{bmatrix} \tag{3-15}$$

The total surface elevation $\eta(x,t)$ of an irregular wave spectrum, is defined as a linear sum of an infinite number of sinusoidal oscillations i dependent on time t and place x. It consists of the constant wave number k_i and rotational speed ω_i for each cos in the sum.

$$\eta(x,t) = \sum_{i=1}^{\infty} \frac{H_i}{2} cos(\omega_i t - k_i x) \tag{3-16}$$

The forward speed of the water $u(x,z,t)$ is a function of surface elevation $\eta_i(t,x)$ and depth from the surface z. Furthermore, it contains the constant wave number k_i for each wave in the sum and the constant total water depth d.

$$u(z,x,t) = \sum_{i=1}^{\infty} \frac{\omega H_i}{2} \frac{cosh\ k_i(d+z)}{sinh\ k_i d} cos(\omega_i t - k_i x) \tag{3-17}$$

$$= \sum_{i=1}^{\infty} \omega \frac{cosh\ k_i(d+z)}{sinh\ k_i d} \cdot \eta_i(x,t) \tag{3-18}$$

3-1-3 Visual representation

Combining these first principles into a visual scheme, Figure 3-2 shows a complete overview. All DOF are written as states x, according to Eq. (3-19). Waves and wind are the external forces acting on the free-floating elastic body.

$$x = [x_p, \beta_p, \varphi, x_d, \dot{x}_p, \dot{\beta}_p, \Omega, \dot{x}_d] \tag{3-19}$$

Deriving a fully linear model from the current symbolic equations should be relatively easy, using a first-order Tailor approximation. However, for this work, the main purpose is to build a wave-FF controller. The first-principles are solely used to gain an understanding of the physics. Therefore, the equations are not extended to a (linearized) model. Instead, a validated linearized model is introduced later on.

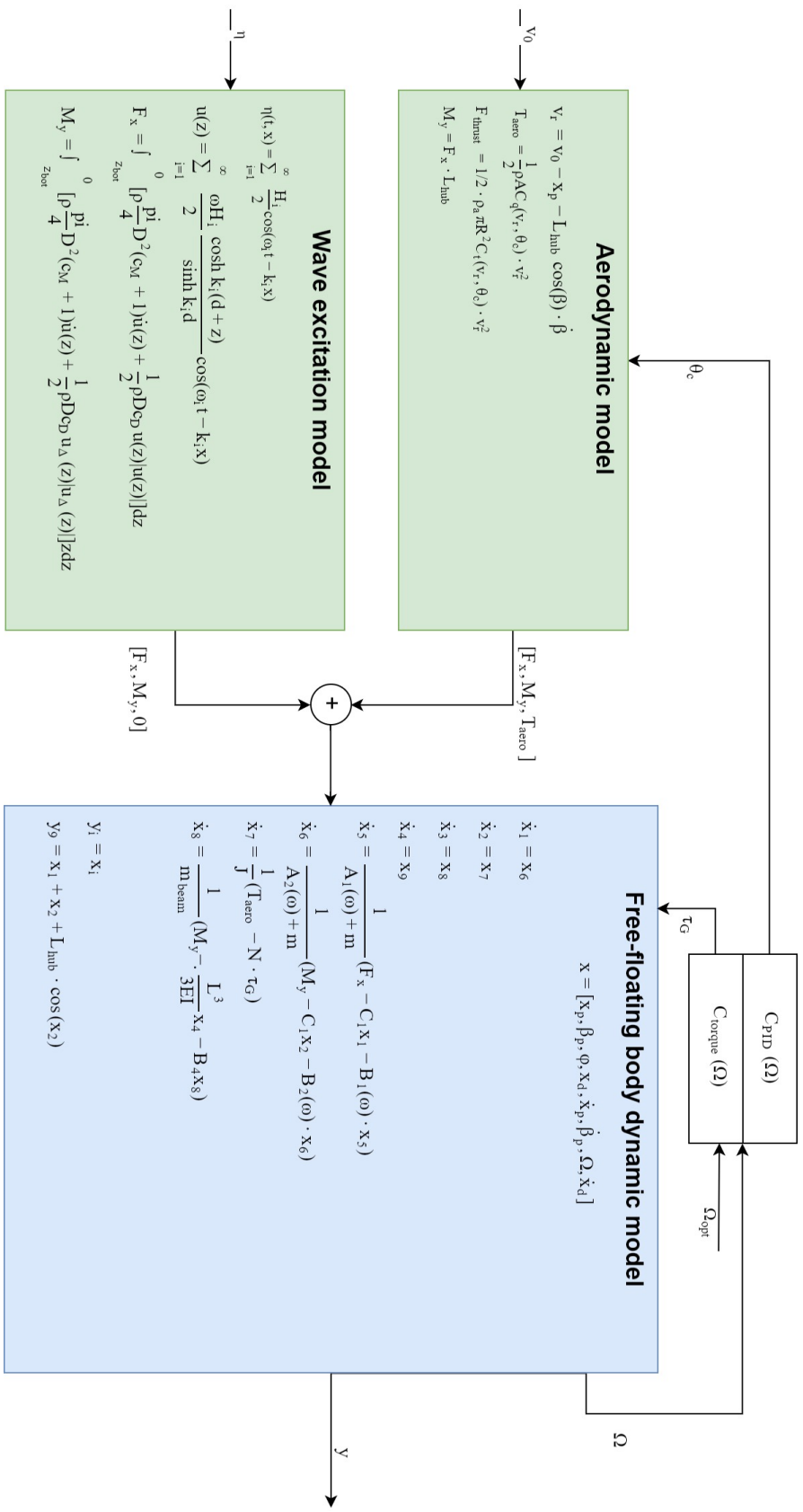

Figure 3-2: Visual summary of the first principles of the TripleSpar.

3-2 SLOW linearization: a linearized turbine model

The next sections will define the CROLM. The main dynamics are contained in a model named SLOW. It is a model developed by the university of Stuttgart [34], containing linearization capabilities for aero-hydro-servo-elastics (excluding the wave-excitation forces). This is an excellent starting point for the LTI model. SLOW is developed for computationally-efficient simulation and linearization. It consists mainly of symbolic equations, avoiding wherever possible computationally expensive operations, such as the convolution integral for non-parametric radiation. Wave excitation loads are modelled as external force inputs. In the context of Figure 3-2, SLOW consists of the aerodynamic model and the free-floating body.

Although most physics are non-linear, linearization is found to provide an excellent approximation around an operating point v_0. The general state-space system is provided in Eq. (3-20). An LTI state-space system is advantages for advanced (model-based) control strategies such as FF control because the states have a physical meaning.

$$\begin{aligned} \dot{\boldsymbol{x}} &= A\boldsymbol{x} + B\boldsymbol{u} \\ \boldsymbol{y} &= C\boldsymbol{x} + D\boldsymbol{u} \end{aligned} \tag{3-20}$$

The states $\boldsymbol{x}$ are similar to the ROM description. The inputs $\boldsymbol{u}$ are defined[2] in Eq. (3-21).

$$\boldsymbol{u} = [\tau_g,\ \theta,\ v_0,\ F_x,\ M_y]^T \tag{3-21}$$

Moreover, Eq. (3-22) defines each operating point i, linearized around $\bar{v}_{0,i}$. A linearization is given at $\bar{v}_{0,i} := [4, 6, ..., 24]$. For each $\bar{v}_{0,i}$, the operating point is defined in $\boldsymbol{x}_{0,i}$ and $\boldsymbol{u}_{0,i}$.

$$\begin{aligned} \boldsymbol{x} &= \boldsymbol{x}_{0,i} + \Delta\boldsymbol{x} \\ \boldsymbol{u} &= \boldsymbol{u}_{0,i} + \Delta\boldsymbol{u} \end{aligned} \tag{3-22}$$

Figure 3-3 illustrates the input-output model of the SLOW-linearization. It contains the same states as described in Section 2-2, plus two states for the platform heave z_p. The latter states are neglected, such that the SLOW model fits with the ROM description. Obtaining the wave-excitation forces as a function of the surface elevation is the subject of the next section.

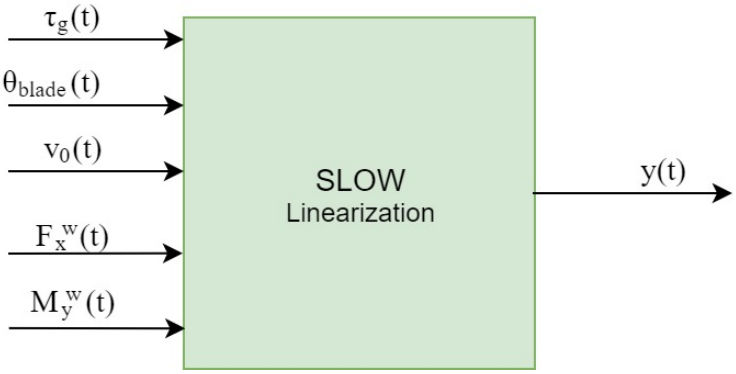

Figure 3-3: SLOW linearized model.

[2]The vertical wave excitation force F_z is set to zero.

As a final note, the SLOW model is essentially the same as a FAST v7 still water linearization. However, for the latter, no wave excitation input channels are available.

3-3 Parametric wave-excitation model

This parametric WEM relates the wave elevation η_0 to the first-order wave excitation loads F_x^{we} and M_y^{we}. Ultimately, the CROLM must relate the wave elevation η_0 to the FOWT dynamics y. Since the SLOW model only relates the wave loads to the dynamics, an additional model had to be identified relating the wave elevations with the wave loads. This model is herein named the WEM and is based on the findings in [32]. In Eq. (3-23), the WEM is denoted as $\boldsymbol{X}$, the loads are $\boldsymbol{P} = [F_x, M_y]^T$ and η_0 is the surface elevation in the origin.

$$P^{we}(\omega) = \boldsymbol{X} \cdot \eta_0(\omega) \tag{3-23}$$

Unfortunately, when measuring the waves in the origin[3], the parametric WEM is found to be non-causal [47]. This means the excitation forces act on the body before the surface elevates. To fit the panel code, wave excitation forces at time t are obtained using future surface elevations $\eta_0(t + t_d)$, similar to Lemmer did in his work [32]. The problem of predicting $\eta_0(t + t_d)$ in a realistic way is described in Section 3-4. The WEM is coupled to the SLOW model in Figure 3-4. In the remainder of this section, the parametric WEM is identified from so-called FRD.

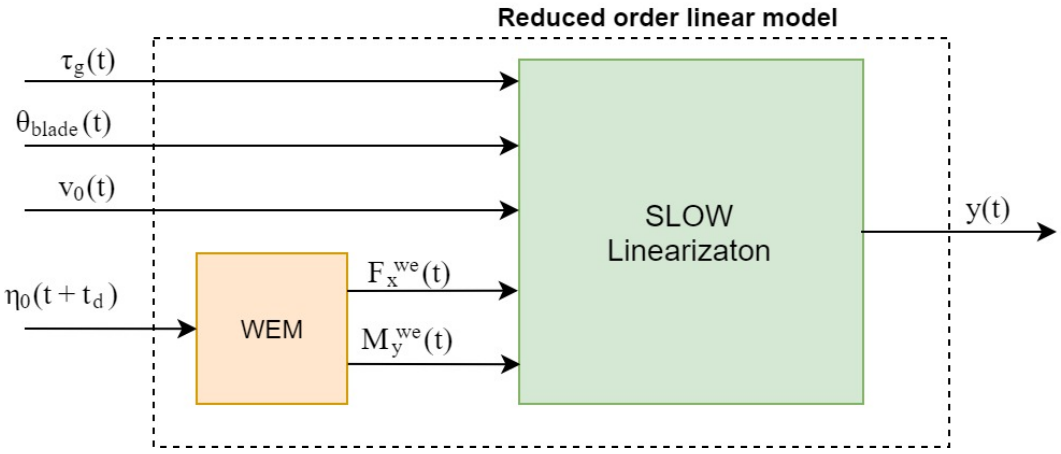

Figure 3-4: Internal structure of the reduced order linear model. The WEM is coupled with the SLOW model.

3-3-1 Non-parametric frequency response data

WAMIT is a state-of-the-art wave interaction analysis and simulation software package. It has been used by the SWE institute to compute the frequency-dependent wave force coefficients for the TripleSpar. This so-called FRD is the non-parametric mapping of surface-elevations $\eta_0(t)$ at the origin $(0, 0)$ to the wave excitation loads P^{we}. For time-domain simulation, FAST

[3]For reference FOWTs, the panel code is defined in the origin.

computes the wave loads prior to simulation, by using the inverse Fourier transform of the product between wave spectrum and wave force FRD.

In Figure 3-5, the dimensionalised [48] SIMO FRD magnitude- and phase data is shown (blue). It is obtained from the *OPTN.3* WAMIT file, contained in the TripleSpar definition files. The frequency ranges from 0.1 rad/s to 5 rad/s with a spectral resolution of 0.1 rad/s.

The first observation of the FRD is the magnitude peaks at 0.09 Hz and 0.18 Hz. These are coherent with the two peaks found in Chapter 2 because the TripleSpar is most sensitive to waves at these frequencies. Also, the positive phase ranging up to more than 2000 degrees is remarkable. It has the shape of a negative time delay, suggesting non-causality. Furthermore, an indication for noise is found in the high-frequency range, starting from about 0.35 Hz. This suggests some inaccuracy from the WAMIT simulation. A reasonable explanation for this behaviour is the element-size of the finite element method simulation being chosen too large. This would be an inaccuracy in the definition of the reference turbine. Fortunately, the inaccuracy will not have a notable effect on this work, since waves do not occur in this frequency range. Next, a parametric model-estimation of the FRD will be obtained.

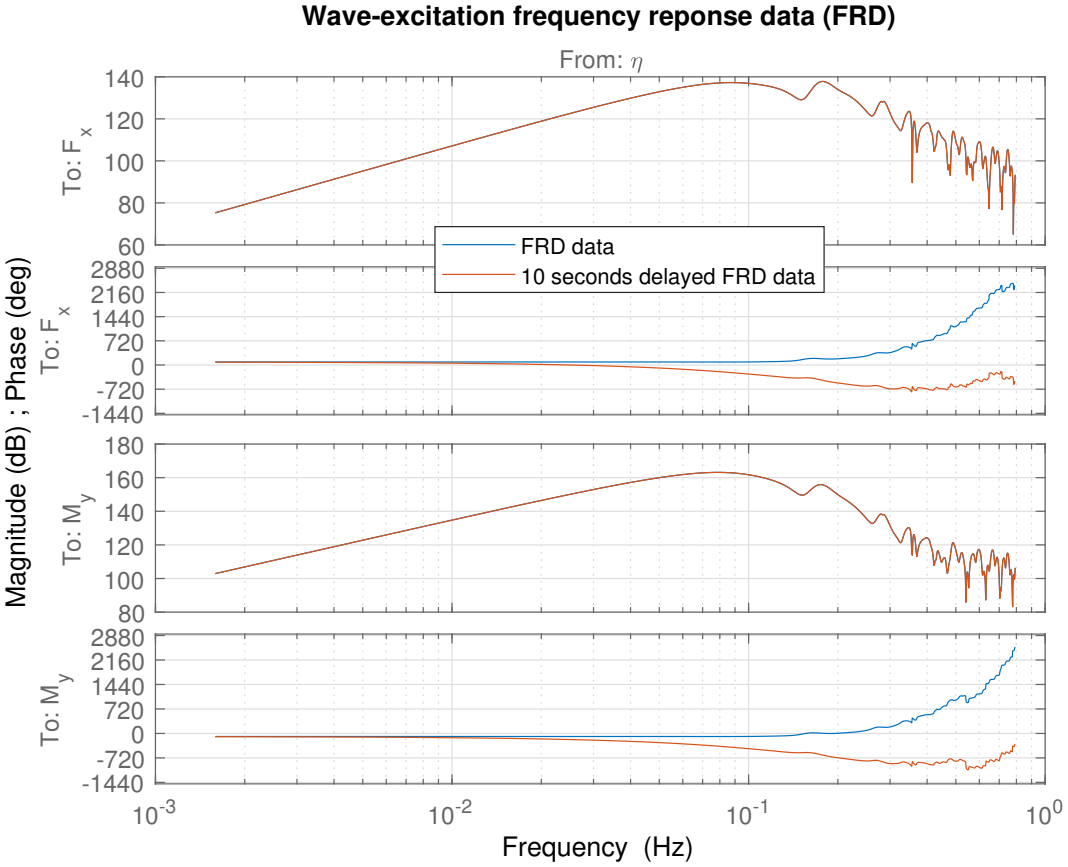

Figure 3-5: FRD from surface elevations η_0 to wave excitation forces F_x^{we} and M_y^{we}.

3-3-2 Frequency-domain subspace identification

In [32], Lemmer obtains the WEM using system identification on the impulse response of the wave force coefficients. The impulse response is calculated by the inverse Fourier transform (IFT) of the FRD. The parametric model is obtained using time-domain system identification. One could simplify this approach by directly identifying the parametric model from the FRD in the frequency domain. This novel approach is explained and implemented in this section.

To make the FRD causal, the output is delayed by 10 seconds. This value will be clarified in Section 3-4. The new FRD model in Figure 3-5 (orange) shows how the phase stays just below 0 degrees, suggesting the model has become causal.

Next, the data is subjected to frequency-domain subspace-identification method *N4SID* with a *MOESP* weighting scheme [49]. The weighing scheme is placed from 0.01 rad/s (0.016 Hz) to 2.2 rad/s (0.35 Hz)[4]. No pre-processing of the data is required. The identification is performed using *ssest* in Matlab.

Table 3-1: Fit to estimation percentages of different order subspace-identification models.

Order	**Fit to estimation data**	
N	F_x	M_y
8	80%	89%
9	88%	96%
10	88%	95%
11	91%	96%
10	89%	95%

The identification results show an excellent fit. Fit to estimation values are shown in Table 3-1. This is the accuracy for a one-step-ahead prediction using some time simulation. An order of $N = 9$ is chosen because it is the first order-size with a nearly perfect match in the relevant wave frequency-range. Both the parametric identified WEM and the non-parametric FRD are shown in Figure 3-6 for comparison. The figure confirms the correctness of the model. Only the low- and high frequency have an offset, but again, as linear waves are mainly present between 0.05 and 0.33 Hz, this is not considered to be a problem. The model can be improved by incorporating prior knowledge into the identification, such as the wave excitation forces being zero at $lim_{\omega \to 0}$.

3-3-3 Time-domain verification

The parametric WEM is simulated in the time domain for verification. When using the current wave-elevation $\eta_0(t)$, we can only calculate the wave-excitation forces 10 seconds delayed[5]. For time-domain verification, the FAST simulation results are also delayed by 10 seconds, such that they can be compared with the output of the WEM.

A time-domain verification of the parametric WEM is performed. The predicted value is compared to the FAST simulation. A JONSWAP irregular wave-spectrum is used as the

[4]The frequency is after 2.2 rad/s is presumed inaccurate, because of the observed variations in the FRD.
[5]The following section will propose a solution for this problem.

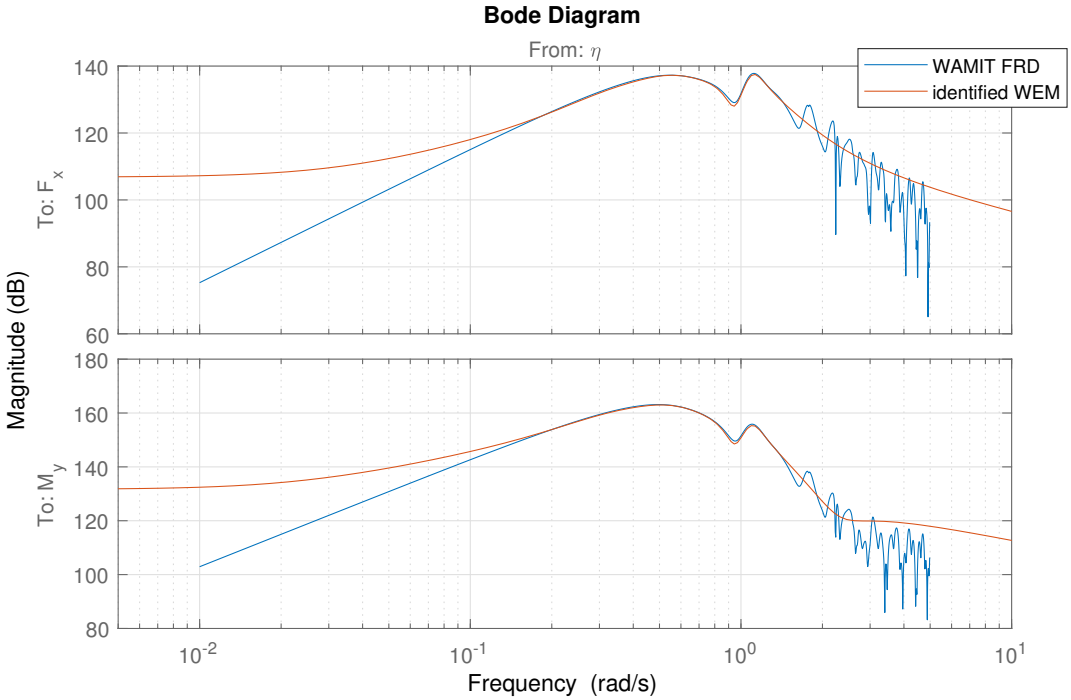

Figure 3-6: Comparison of the parametric identified 10^{th} order WEM and the non-parametric FRD

input. The variance accounted for (VAF) is used as a measure of model fit, calculated using Eq. (3-24). Here y_i is the measured value from FAST, and $\hat{y}_i$ is the estimated value by the WEM. The VAF of the parametric model is found at 98% for both outputs, indicating a nearly perfect fit. Compared to the existing time-domain identified approach by [32], the novel frequency-domain identification method suggests a better model fit while the system-order is reduced. However, a quantitative comparison cannot be obtained, since this work uses a different platform.

$$VAF_i = \left(1 - \frac{var(y_i - \hat{y}_i)}{var(y_i)}\right) \cdot 100\% \tag{3-24}$$

3-4 Surface elevation prediction

When calculating wave-excitation loads of a floating vertical cylinder caused by an impulse wave at the platform origin, it is found that the wave loads are excited prior to the impulse, according to Falness [47]. In other words, the transfer function is non-causal because the output is a function of future inputs. On the contrary, wave propagation is a well-known causal process. Falness argues that the non-causality of the WEM is a result of the spatial location of the transfer function. He states that obtaining a causal system is a matter of placing the measuring point at the side of the floating body. However, the panel code of the reference turbine is defined in the origin.

Even though the non-causality is just a matter of definition, a framework should be developed

to match the panel code of any floating platform design. The wave force coefficients are defined in $(0, 0)$ for any floating platform. The causality problem deals with finding a solution that matches the panel code, such that the WEM is causal.

3-4-1 Time delay to obtain causality

An illustration of this non-causality is shown in Figure 3-7, where the impulse response is simulated in FAST[6]. One can observe how the output of the original system (middle plot) is effected before any wave (top plot) arrives at the platform origin. A causal modification of the transfer function is introduced by Lemmer [32]. With an input-output delay of $t_d = 10$ seconds, the response becomes nearly causal (bottom plot). Only a few minor oscillations occur at negative times. Therefore, 10 seconds is defined as the time-shift for which the time-domain realisation of wave force coefficients of this floating platform is non-causal. A delay of 10 seconds on the output makes the system causal. Also, 10 seconds prior wave-elevation knowledge is enough to obtain the current wave loads using the identified model.

Future knowledge of the surface height $\eta_0(t) = \eta_0(t + t_d)$ are required to calculate the current wave excitation loads $P^{we}(t)$. Future knowledge is not available in reality. Lemmer obtains the wave-prediction in [32] by using a pre-calculated future time-series of the simulation. This works well in simulation but is not possible when dealing with real-time applications like control. A novel approach for predicting future wave elevations[7] $\hat{\eta}_0(t + t_d)$ is required.

[6]For clarity reason, this analysis is only applied only on M_y. However, the observations are similar when using F_x

[7]The hat at $\hat{\eta}$ denotes the approximation of the future value.

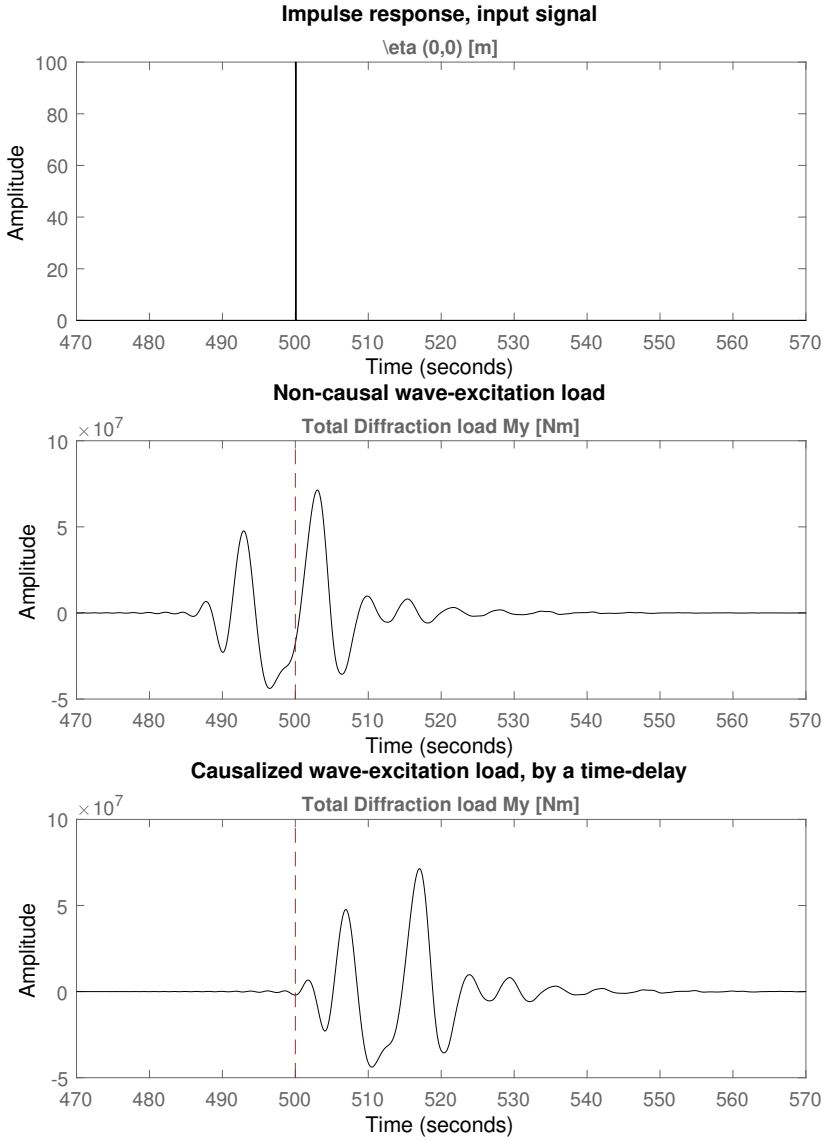

Figure 3-7: Wave-elevation impulse response of M_y on the TripleSpar platform. Above: input signal. Middle: non-causal wave loads. Bottom: causalized wave signal.

3-4-2 Mathematical derivation of the wave prediction method

In this section, an approach is proposed to predict the future wave elevation in a given downstream position from upstream measurements. Suppose we have two points on the x-axis, x_A and x_B, with $x_A < x_B$, illustrated in Figure 3-8. x_A is some point in an upstream position with respect to the FOWT, x_B is at the COF. The distance L between the points is given by:

$$x_B - x_A = L > 0 \tag{3-25}$$

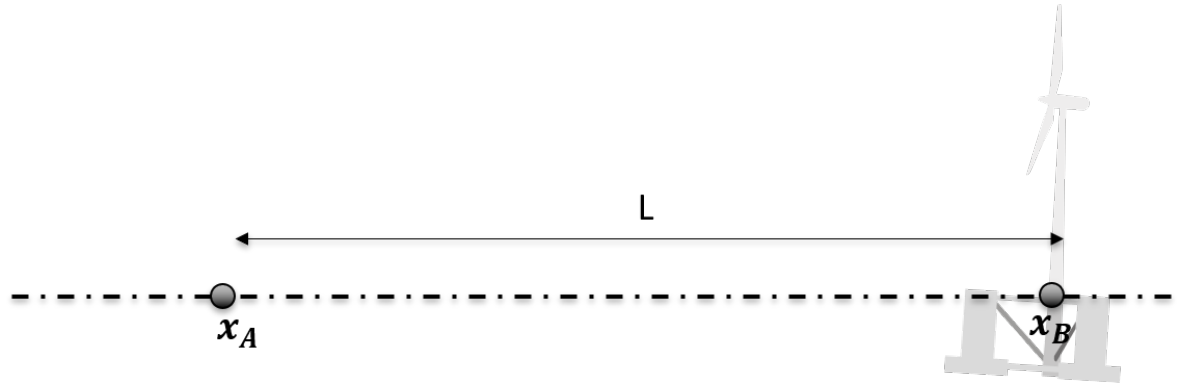

Figure 3-8: Two wave-measurement point. x_A is L meters in front of the floating platform. x_B is at the COF (0,0) of the platform.

Now consider the surface elevations $\eta_A(t)$ and $\eta_B(t)$ at each point. The time-delay between $\eta_A(t)$ and $\eta_B(t)$ is frequency dependent according to the dispersion relationship in Eq. (3-26), where c denotes the wave speed, k the (wave-frequency dependent) wave number and d the water depth.

$$c = \sqrt{\frac{g}{k} tanh(kd)} \tag{3-26}$$

From [47], assuming deep water conditions[8], we know the transfer function $H(\omega)$ from $\eta_A(t)$ to $\eta_B(t)$ can be written as Eq. (3-27), where ω denotes the angular frequency.

$$H(\omega) = \exp\left(-i\frac{\omega^2 L}{g}\right) \tag{3-27}$$

Using this, we can estimate the wave propagation from $\eta_A(t)$ to $\eta_B(t)$ at the same time instance t in the frequency domain.

$$\eta_B(\omega) = H(\omega) \cdot \eta_A(\omega) \tag{3-28}$$

Now consider a time delay t_0, of some signal $u(t)$ to $u(t - t_0)$. The fourier notation of a time delay $D(\omega)$ is written in Eq. (3-29).

$$D(\omega) = \exp\left(-i\omega \cdot t_0\right), \tag{3-29}$$

According to the definition of causality, $D(\omega)$ is causal if and only if it is subjected to $exp(-i \cdot a)$ with $a \geq 0$, or $t_0 \geq 0$. A negative time delay denotes a prediction of some signal. Negative time delays $t_d = -t_0$ (s.t. $t_0 < 0$) are by definition non-causal.

However, by combining the location shift $H(\omega)$ in Eq. (3-27) with some negative time delay $D(\omega)$ in Eq. (3-29), a causal dependency *can* be obtained for a limited bandwidth of wave

[8]For non-deep water conditions, a similar equation can be easily derived using an approximation of the wavenumber k_i as a function of the water depth d and the wave period T_i.

frequencies. The product of $H(\omega)$ and $D(\omega)$ is defined as

$$\begin{aligned} H_d(\omega) &= H(\omega) \cdot D(\omega) \\ &= \exp\left(-i\frac{\omega^2 L}{g}\right) \cdot \exp\left(-i\omega \cdot t_0\right) \\ &= \exp\left(-i\frac{\omega^2 L}{g}\right) \cdot \exp\left(i\omega \cdot t_d\right) \\ &= \exp\left(i\omega(t_d - \frac{\omega L}{g}\right) \qquad \text{causal } \forall\, t_d \leq \frac{\omega L}{g} \end{aligned} \tag{3-30}$$

Using $H_d(\omega)$ from Eq. (3-30), we have derived an analytical prediction of $\eta_B(t+t_d)$ using the measurement of $\eta_A(t)$. This information can be used for the real-time simulation purposes introduced in Chapter 4.

The exponent $exp(-i \cdot a)$ remains non-positive for all ω s.t. the causality requirement from Eq. (3-30). Physically, the requirement defines the maximum observable wave-frequency ω (remember: $\omega = 2\pi/T$), using some measurement-distance L for t_d seconds in advance. The necessary delay $t_d = 10$s is already obtained in Sec. 3-4-1. When re-writing the requirement and substituting $\omega = 2\pi/T$, one obtains the maximum causal wave period $T_{max}(L, t_d)$ as a function of measurement distance L and prediction time t_d.

$$T_i \leq \frac{2\pi L}{g t_d} \tag{3-31}$$

$$T_{max}(L, t_d) = \frac{2\pi L}{g t_d} \tag{3-32}$$

From this requirement, it follows that for example, to have causal knowledge of all waves with a period less or equal then 20 seconds ($T \leq 20$), with $t_d = 10$ seconds before this signal arrives, a measurement distance of $L \geq 436$ m is required.

3-4-3 Practical implementation

A practical method is required to perform the following operation in real-time. Equation (3-34) demonstrates the necessary operation. The Fourier transform (FT) from time domain to frequency domain is denoted as FT. In reality, a measurement of $\eta_A(t)$ is a discrete time signal $\eta(k)$ with some sampling-time T_s. Therefore we use the fast Fourier transform (FFT) and its inverse, the inverse fast Fourier transform (IFFT).

$$\hat{\eta}_0(t + t_d) = IFFT\Big(FFT(\eta_A(t)) \cdot H_d(\omega)\Big) \tag{3-33}$$

$$= ifft\Big(\eta_A(\omega) \cdot H_d(\omega)\Big) \tag{3-34}$$

The implementation of Eq. (3-34) is illustrated in Figure 3-9. The discrete time-signal $\eta_A(k)$ is stacked in an n-row array and fed into the FFT. The larger the stack-size, the better the performance, but the more computationally heavy. Next, $\eta_A(\omega)$ denotes the discrete frequency domain wave data. The frequency-range of the two-sided discrete Fourier spectrum

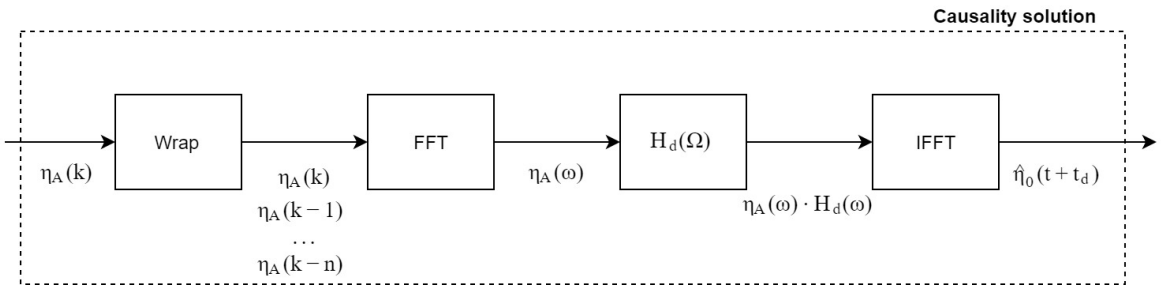

Figure 3-9: Block scheme of the practical implementation of the proposed causality solution. The framework approximates future surface elevations at $\eta_0(t+t_d)$ using some wave-measurement $\eta_A(t)$ in front the FOWT.

ω is defined in Eq. (3-35). The spectral resolution is defined as $\Delta\omega = \frac{2\pi}{n \cdot T_s}$ with T_s for the simulation time-step.

The signal $\eta_A(\omega)$ is multiplied with the transfer function $H_d(\omega)$, containing the location shift and negative time delay. This product is fed into the IFFT and results in our goal: future wave knowledge at the platform origin $\hat{\eta}_0(t + t_d)$.

$$\omega = [\frac{-n/2}{n}, \frac{-n/2+1}{n}, ..., \frac{n/2}{n},] \cdot \frac{2\pi}{T_s} \tag{3-35}$$

3-4-4 Verification

A sample time of $T_s = 0.1$ seconds and a stack-size of $n = 1024$ are chosen for verification of the methodology presented before. Furthermore, a measuring distance $L = 450$ and time delay $t_d = 10s$ are selected. Waves are simulated using load case 3. For verification, two signals are compared as illustrated in Figure 3-10. It computes the surface-elevation measurement $\eta_0(k)$ and the approximation $\hat{\eta}_0(k+N)$, for N steps in the future, with $N = t_d/T_s$. For comparison, the approximation is delayed with N steps using the block scheme in Figure 3-10.

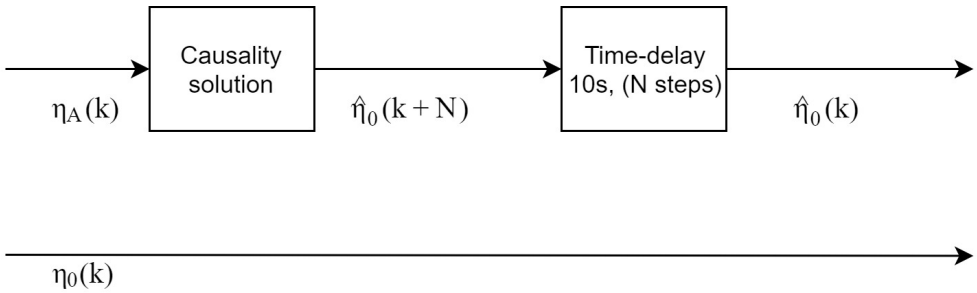

Figure 3-10: Causality verification setup. The causal wave forecast is compared to the measured signal in FAST.

The results are shown in Figure 3-11. One can observe that in the first 40 seconds, not enough data samples are available for a good approximation. In other words, not enough frequency information is available. Over time the performance increases. After 102.4 seconds, the input matrix is fully stacked and maximum performance is obtained.

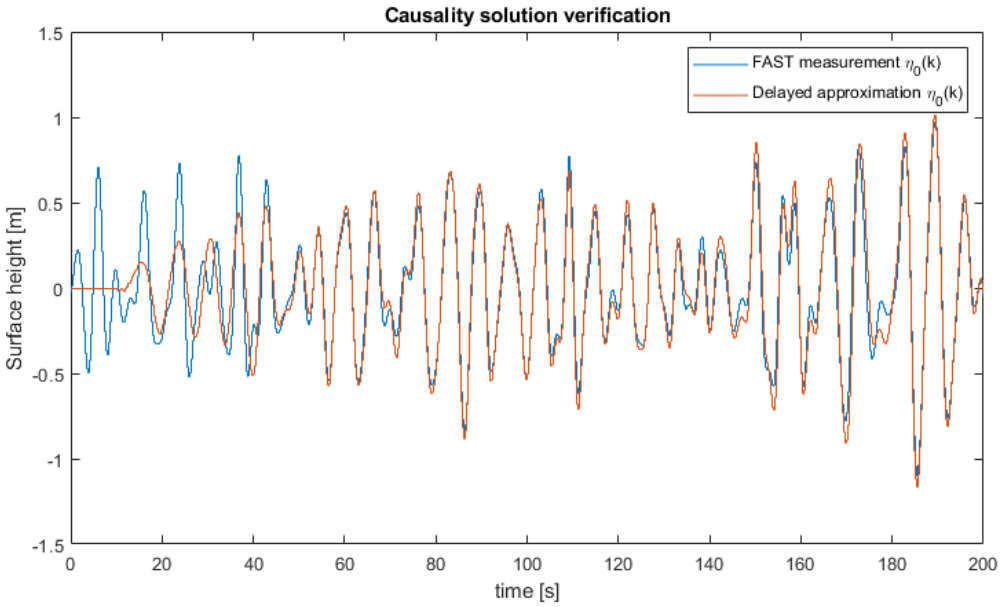

Figure 3-11: Verification results: the measurement of the surface elevation in the COF (blue) and the causal approximation (orange).

The VAF between $\eta_0(t)$ and $\hat{\eta}_0(t)$, is used as a measure of accuracy. Only the values from $t > 102.4$ are used since these are full stacked[9]. Simulating of load case 3 for 600 seconds, the VAF is found to be 95%. This should be sufficient for effective wave-FF control.

3-5 Coupling of the linear subsystems and controller linearisation

All sub-modules for obtaining a linear model are now in place. The composition of the new CROLM is illustrated in Figure 3-1. This figure is already provided at the beginning of this chapter. The CROLM is useful for many purposes, such as linear analysis and model-based FF control. It is derived by first-principles linearization (SLOW), parameterization of WAMIT wave force coefficients (i.e. the WEM) and an analytically derived wave prediction method.

For completeness, the controllers are also linearized. The quadratic generator torque P-controller (region 2) is linearized around operating point Ω_o in Eq. (3-36). Here, k_p is the controller gain. Subscript o denotes the operating point.

$$\begin{aligned} \tau_G &= k_p \cdot \Omega^2 \\ &\approx 2k_p \cdot (\Omega - \Omega_o) \end{aligned} \tag{3-36}$$

The collective-pitch PI-controller (region 3) is already linear, denoted in Eq. (3-37). Here is k_p the proportional gain and k_I the integral gain.

$$\theta_c = k_p(1 + k_I/s) \cdot (\Omega - \Omega_o) \tag{3-37}$$

[9]This can be considered to be steady-state performance.

The power PI-controller (region 3) is also linearized in Eq. (3-38), around its operating point $P_o = \Omega_o \tau_{g,o}$. It is denoted as follows, with k_p as the proportional gain and k_I the integral gain. Moreover, the o subscript denotes the operating point.

$$\begin{aligned}
\theta_c &= k_p(1 + k_I/s) \cdot (P - P_o) \\
&= k_p(1 + k_I/s) \cdot (\tau_g \Omega - P_o) \\
&\approx k_p(1 + k_I/s) \cdot \Big(\tau_{g,o}\Omega_o + \tau_{g,o}(\Omega - \Omega_o)\Omega_o + (\tau_g - \tau_{g,o}) - P_o\Big) \\
&= k_p(1 + k_I/s) \cdot \Big(\tau_{g,o}(\Omega - \Omega_o) + \Omega_o(\tau_g - \tau_{g,o})\Big)
\end{aligned} \tag{3-38}$$

3-6 Summary

In this chapter, a foundation has been established to understand the dynamics of the TripleSpar. The first principles are identified and summarised visually. Next, a CROLM is obtained according to the ROM description. It consists of a SLOW linearization, a parametric WEM and a wave prediction method. The SLOW model is developed by the university of Stuttgart and adapted in this work. It contains the dynamics of the free-floating body and the aerodynamics.

A novel approach to parameterize the WEM is obtained, such that it fits with the panel code of reference FOWTs. Wave load coefficients from the reference turbine contain the non-parametric FRD from surface elevation to wave excitation loads in COF. However, the FRD is found to be non-causal. To make it causal, the output is delayed by 10 seconds.

The delayed FRD is subjected to frequency domain subspace identification to obtain the parametric WEM. The resulting 9^{th} order SIMO state-space model has a VAF of 98% and it is in good agreement with the FRD in the frequency domain plot. This method simplifies the existing method [32], while potentially providing a more accurate and lower order model.

To estimate the wave forces at the current time, an analytical wave prediction method is introduced. The wave-elevation signal is measured at some point in front of the platform. Then, the signal is location-shifted using $H(\omega)$ and subjected to the negative time delay $D(\omega)$ in the frequency domain. The result is a prediction of the surface elevation in $\eta_0(t + t_d)$ with a VAF of 95%. This novel wave prediction method allows one to implement the model for real-time control purposes.

All subsystems are coupled into a so-called CROLM. This model relates the inputs τ_g, θ_c, η_A and v_0 with the outputs y in a linear way. The new model allows model-based control and linear analysis.

Chapter 4

Design of a linear feedforward controller

The LTI model from Chapter 3 can be utilised to design a linear FF controller. Design of the controller takes place in the simplified linear environment, using the CROLM as a plant and linearized controllers. Once a FF controller is designed, it is tested on the non-linear plant in the next chapter.

Several potential wave-FF control objectives are found in Chapter 2, based on the wave-influenced outputs. First, rotor speed variations (Ω) should be reduced to stabilise power production. Second, tower-base load ($M_{y,T}$) cycles should be reduced. Third, blade pitch control action should be reduced to extend the lifetime of the pitch bearing. The goal of this chapter is to develop an effective wave-FF controller using the findings from the previous chapters.

The linear system is analysed in Section 4-1. This should provide key-insights for the controller design. Then, the control logic is derived in Section 4-2. Here, we will also discuss alternative wave-accommodating control strategies. In Section 4-3, the controllers will be designed depending on the operating point. Ultimately, the procedure to design a wave-FF controller is generalised in Section 4-4. It contains an overview of the steps, required to design a wave-FF controller for some arbitrary FOWT or control objective.

4-1 Linear system analysis

Using linear analysis, one can increase the understanding of the system dynamics. The TripleSpar is modelled as a MIMO system. The sensitivity to control inputs and disturbance inputs on the system outputs is investigated. Furthermore, the CL disturbance sensitivity is obtained. Two important questions about the system will be answered. Which control input is best suited to reject some specific wave disturbances? Which dynamics are sensitive to wind or waves and at which frequency? Moreover, the linear analysis explains many effects that have been observed in Chapter 2.

The CROLM will from now be denoted as $\hat{G}$, where the hat indicates the linearization. The system input channels are $u = [\tau_g,\ \theta,\ v_0,\ \eta_0]^T$. The output channels y are equal to the states x plus the tower top displacement x_t. The linearised baseline CL control logic is shown in Figure 4-1. Furthermore, $\hat{G}_i$ is the controlled sub-system from $u = [\tau_g, \theta_c]^T$ to y and $\hat{G}_d$ is the disturbed sub-system from $d = [v_0, \eta]^T$ to y.

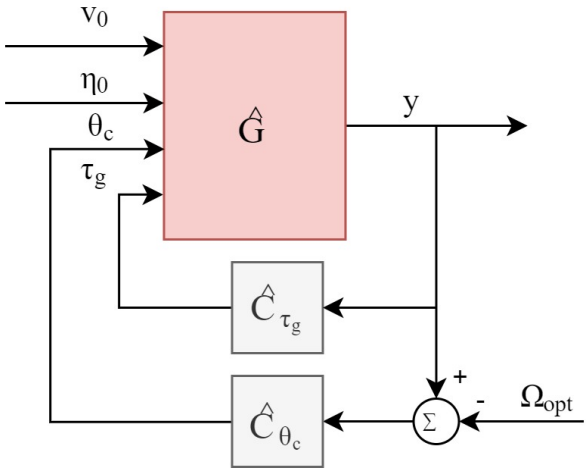

Figure 4-1: CL baseline configuration. $\hat{G}$ is the CROLM, $\hat{C}_{\tau_g}$ is the linearised torque controller and $\hat{C}_{\theta_c}$ is the linearised pitch controller.

For reasons of briefness, linear analysis is performed on two output channels: the rotor speed Ω and the second-derivative of the tower deflection $\ddot{x}_d$. The rotor speed Ω represents a linear measure of stable power production. It is chosen over the power P, because P is a quadratic output and does not follow linearly from the LTI system. The second derivative of the tower deflection $\ddot{x}_d$ represents the tower-base load $M_{y,T}$, because internal loads are not contained in the CROLM. From Eq. (3-10) in Section 3-1, we learned $c \cdot M_{y,T}$ is a linear function of $\ddot{x}_d$ using some constant c. High-frequent $c \cdot M_{y,T}$ (or $\ddot{x}_d$) variations will increase fatigue damage and shorten the lifetime.

4-1-1 The TripleSpar as I/O system

The bode plot of the input/output system $\hat{G}_i$ is used for basic system analysis. Before drawing the bode plot, an input-output scaling will be applied. This provides a quantitative, dimensionless comparison between the in- and outputs. The dimensionless system is denoted by $\bar{G}$. The scaling law is denoted by Eq. (4-1), similar to [35]. Here x_t is replaced by $\ddot{x}_d$, since we are more interested in tower load cycles then tower-top motions

$$\hat{G} = D_y^{-1} \bar{G} D_u \tag{4-1}$$

The scaling matrices are $D_{u,d}$ and D_y are defined in Eq. (4-2). Their values are also chosen similar to [35].

$$D_{u,d} = \begin{bmatrix} 0.1\tau_{g,0} & 0 & 0 & 0 \\ 0 & 5\frac{\pi}{180} & 0 & 0 \\ 0 & 0 & 0.1\bar{v} & 0 \\ 0 & 0 & 0 & 4 \end{bmatrix}, \quad D_y = \begin{bmatrix} 0.13\Omega_0 & 0 \\ 0 & 1 \end{bmatrix} \tag{4-2}$$

The bode plot of $\bar{G}_i$ is shown in Figure 4-2. The natural frequencies in surge, pitch and tower FA deflection are indicated on the x-axis, corresponding to the TripleSpar. Recall the disturbance frequency ranges of wind and waves, found in Section 2-3. For clarity the frequency ranges are denoted as f^{we} for waves and f^{wi} for wind. The scale is chosen logarithmic, similar to the frequency domain plots.

$$f^{we} := \{f \subset \mathbb{R} \mid 5 \cdot 10^{-2} < f < 3.33 \cdot 10^{-1}\} \text{ Hz} \tag{4-3}$$

$$f^{wi} := \{f \subset \mathbb{R} \mid f < 2.5 \cdot 10^{-2}\} \text{ Hz} \tag{4-4}$$

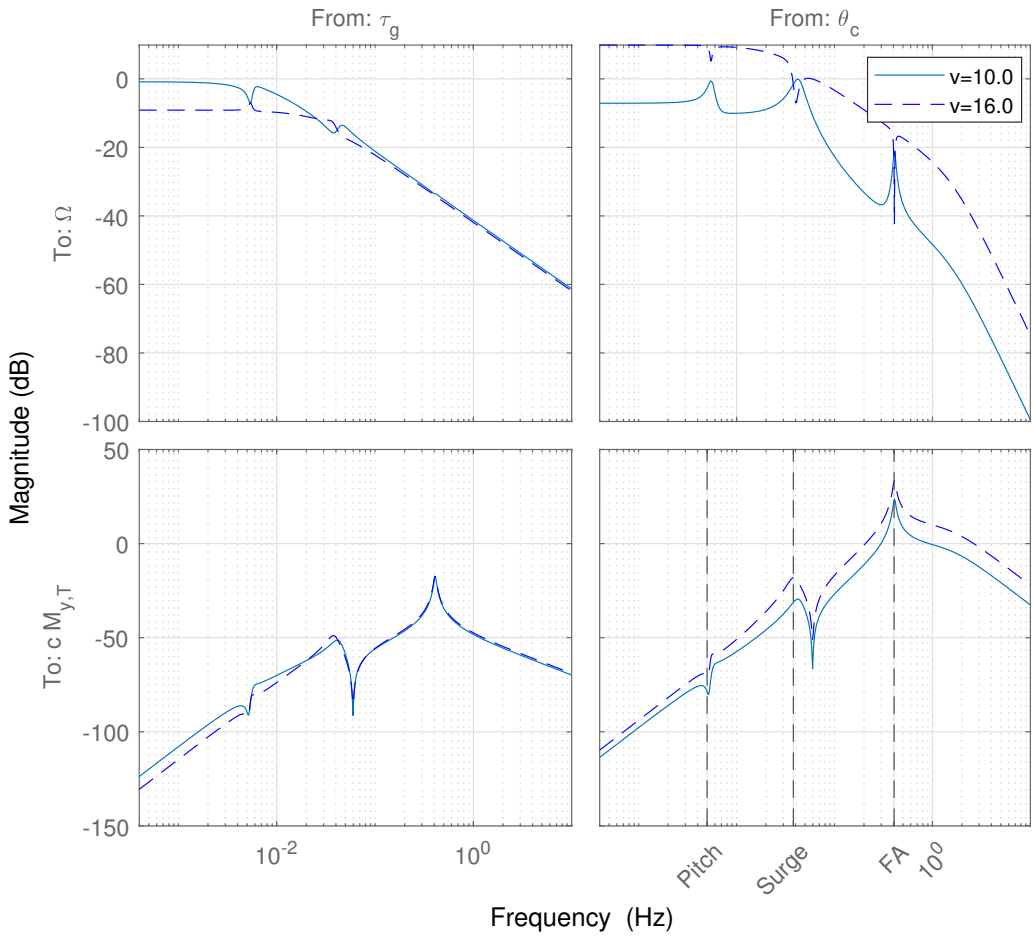

Figure 4-2: Input-output magnitude diagram of the dimensionless linearized controlled plant $\hat{G}_i$.

The figure demonstrates how control is mainly effective on the rotor speed Ω (top row) in the low-frequency range. The generator torque τ_g (top left) is less effective at the natural frequencies f_n, whereas the collective pitch θ_c (top right) is more effective at these frequencies in below rated and less effective in above-rated. A magnitude-peak at some natural frequency indicates a complex conjugate pole pair close to the imaginary axis. A magnitude-dip means a complex conjugate zero pair close to the imaginary axis. A shift from peak to dip, indicates two poles becoming two zeros. The pitch control θ_c is much more effective on $cM_{y,T}$ (bottom

left) then the generator torque τ_g (bottom right). Effectiveness is highest on the FA natural frequency.

Changing the operating point is primarily effective on $\hat{G}_{\theta_c \to \Omega}$ (right-top). The resonance peaks (i.e. complex conjugate pole pairs) become anti-resonance peaks (i.e. complex conjugate zero pairs) and the gain increases significantly. Furthermore, one pole pair of $\hat{G}_{\tau_g \to \Omega}$ (left top) disappears.

The same analysis is applied to the bode plot of the disturbance system $\hat{G}_d$, shown in Figure 4-3. Here $\hat{G}_{v_0 \to \Omega}$ (top left) looks similar to $\hat{G}_{\tau_g \to \Omega}$. Also $\hat{G}_{v_0 \to cM_{y,T}}$ (bottom left) is similar to $\hat{G}_{\tau_g \to cM_{y,T}}$. On rotor speed Ω (top row), wind v_0 is dominant in the low-frequency (i.e. f^{wi}) whereas waves η_0 are dominant in the high frequency (i.e. f^{we}). This confirms our observations in Section 2-6, stating waves are driving high-frequent dynamics whereas wind is driving low-frequent dynamics.

On the bending moment $cM_{y,T}$, we notice high gains in f^{we} and near-zero gains in f^{wi}. Again this confirms our observations in Section 2-6, stating waves are mainly responsible for high tower bending loads. The operating point for wave disturbance changes only slightly for different wind speeds.

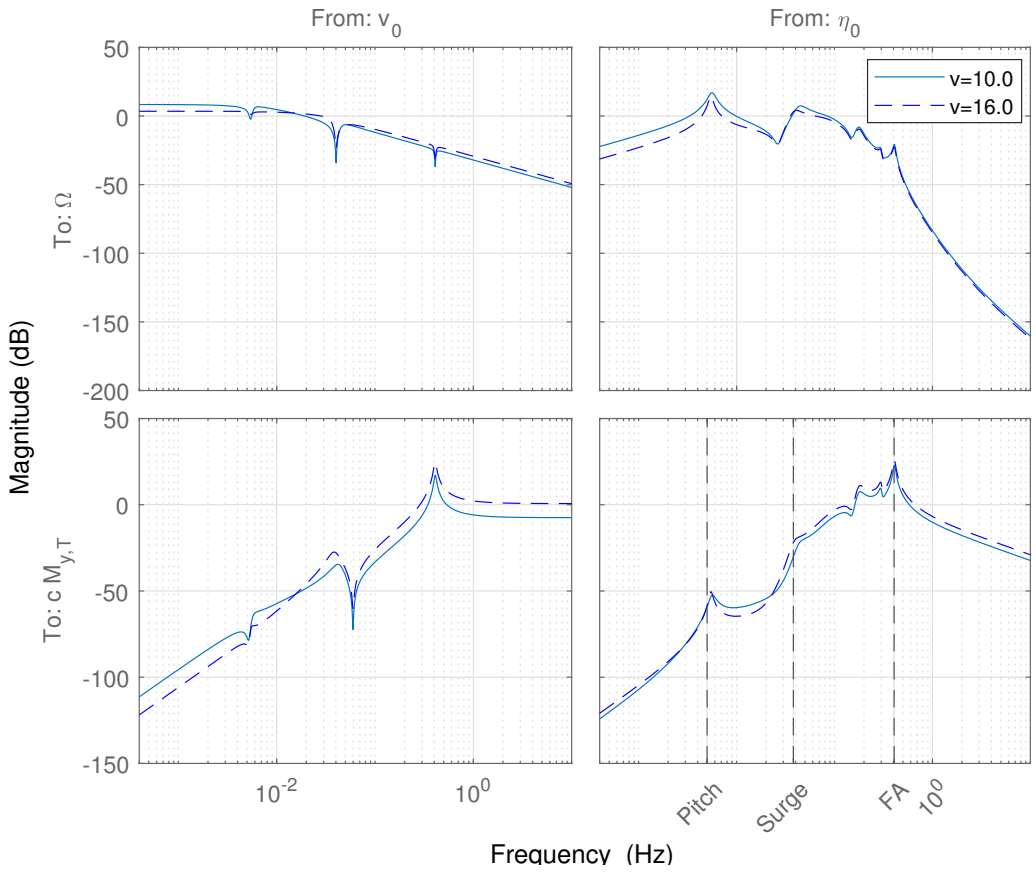

Figure 4-3: Input-output bode diagram of the dimensionless linearized disturbed plant $\hat{G}_d$

4-1-2 Closed-loop sensitivity to disturbances

Now, the linearized baseline controller is included in the analysis. The disturbance sensitivity in Figure 4-4 denotes the CL system performance. It indicates disturbance-sensitive frequencies. High magnitude indicates disturbance sensitivity and low magnitude indicates good disturbance rejection. Especially the magnitude in the range of f^{we} and f^{wi} should go to down as much as possible. To obtain additional insights, the tower top displacement is also added.

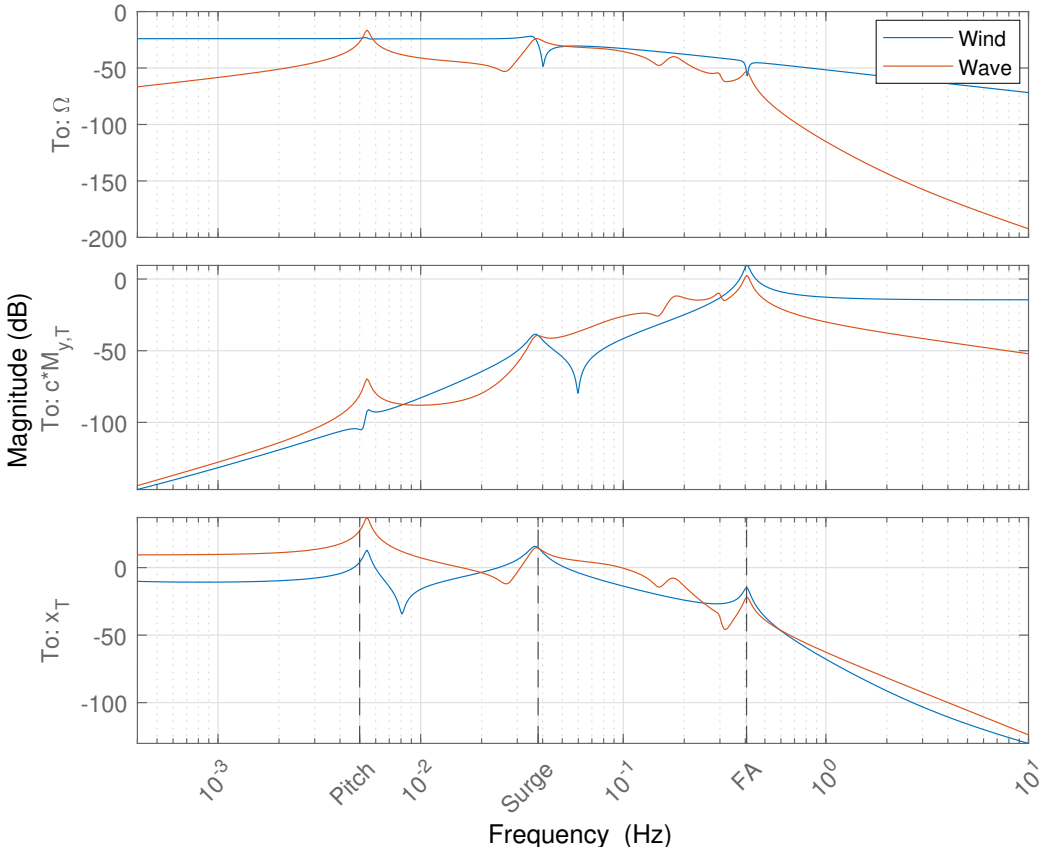

Figure 4-4: The system CL sensitivity to wind and wave disturbances at operating point $v_0 = 10$ m/s.

Many observations follow from the plot. On rotor speed Ω (top plot), the wind is dominant over the waves. Waves cause resonance on natural frequencies of the FOWT (pole-pair) while wind causes anti-resonance (zero-pair). For low frequencies, wave-sensitivity decreases whereas the wind-sensitivity stays constant. Waves in the range of f^{we} are non-dominant over wind in f^{wi}, yet significant.

On the tower bending moment $cM_{y,T}$ (middle plot), the response within f^{wi} is almost unaffected by wind, whereas the wave response is hugely effected in f^{we}. These are the wave-induced load cycles, found in Chapter 2. A reasonable explanation is the amplification of

high frequencies by the double derivation in $\ddot{x}_d$.

In the tower top displacement x_t, (bottom plot) similar resonance and anti-resonance peaks occur as with the rotor speed (top plot). This linear analysis shows the physical effect of the disturbances on the TripleSpar. A wave is acting on the platform, causes resonance on natural frequencies[1]. Therefore the tower top x_t excites, relative wind speed v_r excite and the rotor speed Ω excites. Thus, waves cause resonance on the tower top x_t and the rotor speed Ω. On the contrary, wind acts mainly on the rotor. A wind gust v_0 excites the rotor speed Ω directly. Because the tower moves along at the natural frequencies, the rotor speed Ω is damped at these frequencies. Thus, wind causes anti-resonance on the rotor speed ω while waves cause resonance on the rotor speed Ω.

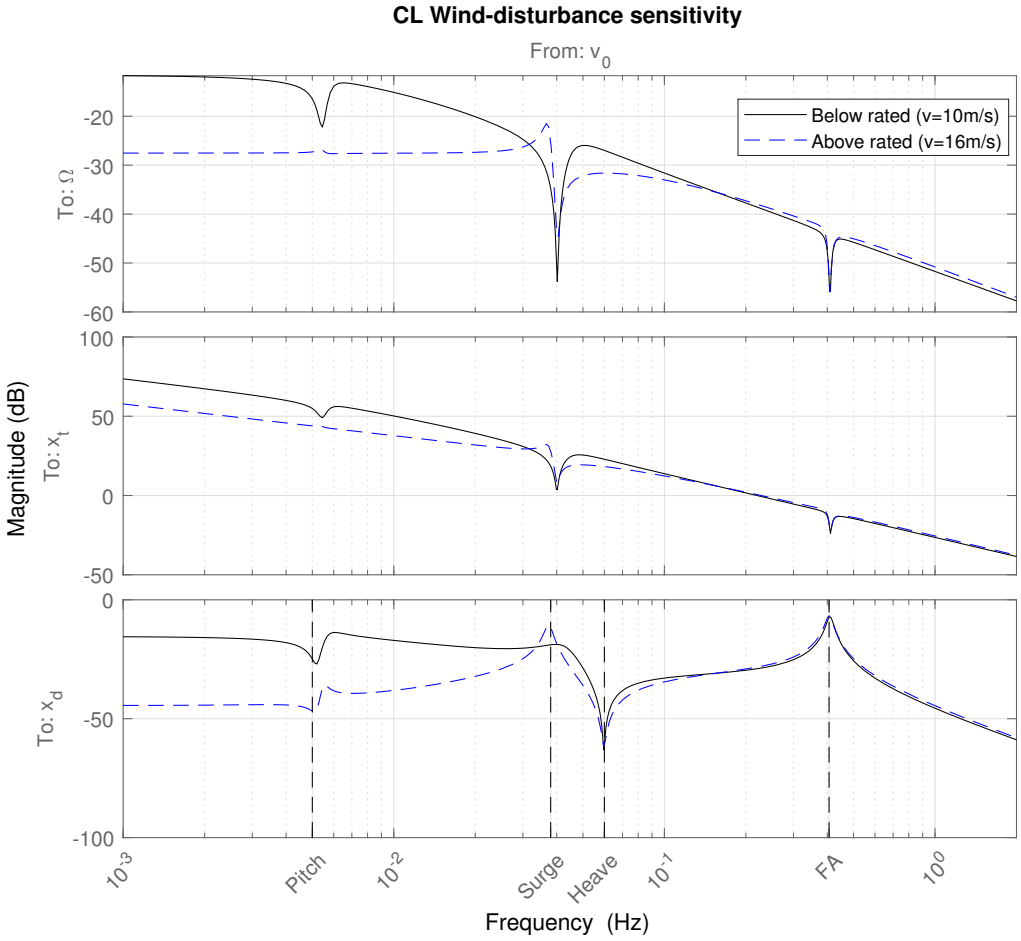

Figure 4-5: The system CL sensitivity to wind disturbances. Shift from below rated to above rated.

Comparing the wind sensitivity[2] below and above rated in Figure 4-5, several observations follow. The pitch anti-resonance disappears, while other anti-resonance peaks decrease. Furthermore, above-rated is generally less sensitive to low-frequency wind variations. Therefore,

[1] Although solely FA is contained in f^{we}, this statement is about the physics, explaining resonance and anti-resonance peak. Therefore, all natural frequencies are considered.

controllability increases. The wave-sensitivity does not change at different operating points, because it has only one operating point. Waves always oscillate around $\eta = 0$.

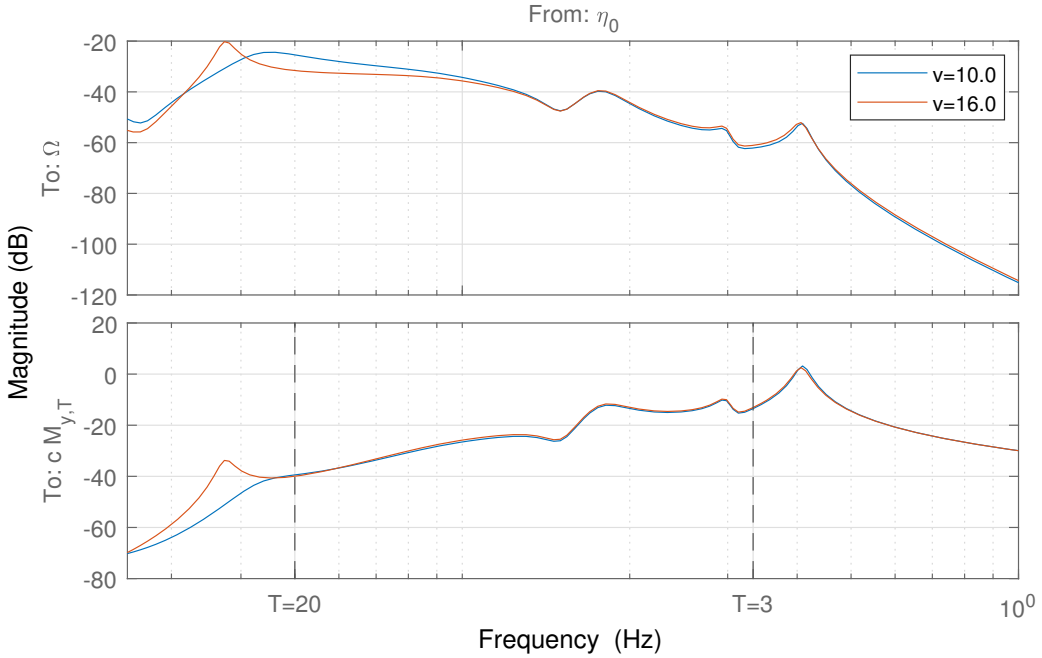

Figure 4-6: Wave sensitivity in the wave frequency. The lower, the better. The frequencies where waves are present are indicated with the black dashed lines.

Ultimately, the wave sensitivity is shown in Figure 4-6. The frequency scale is adjusted to f^{we} (indicated by the dashed lines). A peak for both outputs is again found at 0.18 Hz. The rotor is sensitive to long waves, whereas the tower-loads are sensitive to short waves. Reducing the sensitivity in this frequency-range is the primary goal of a wave-FF controller.

4-1-3 Relative gain array

The RGA [50] will provide information on which input is best suited to effectively control a certain output. The dominant input-output couples in MIMO control can be distinguished. The result is frequency-dependent and requires a non-singular, square plant. The system is decoupled when, after rearranging input and output channels with selected pairs on the diagonal, the RGA is close to identity. The RGA of $\hat{G}_d$ is less interesting since wind does not occur in the same frequency as waves.

First a simple RGA is computed in Eq. (4-5) using $\hat{G}_i$. For the below-rated system at $v_0 = 10$, the RGA at 0.1 Hz ($T = 10$ s) is nearly decoupled. It confirms τ_g is best suited to control to control Ω, whereas θ_c is best suited to control tower loads $cM_{y,T}$.

$$\begin{bmatrix} \Omega \\ cM_{y,T} \end{bmatrix} \approx \begin{bmatrix} 0.99 & 0.01 \\ 0.01 & 0.99 \end{bmatrix} \begin{bmatrix} \tau_g \\ \theta_c \end{bmatrix} \tag{4-5}$$

Looking at the frequency-dependent RGA in Figure 4-7, this relation holds for all frequencies at this operating point.

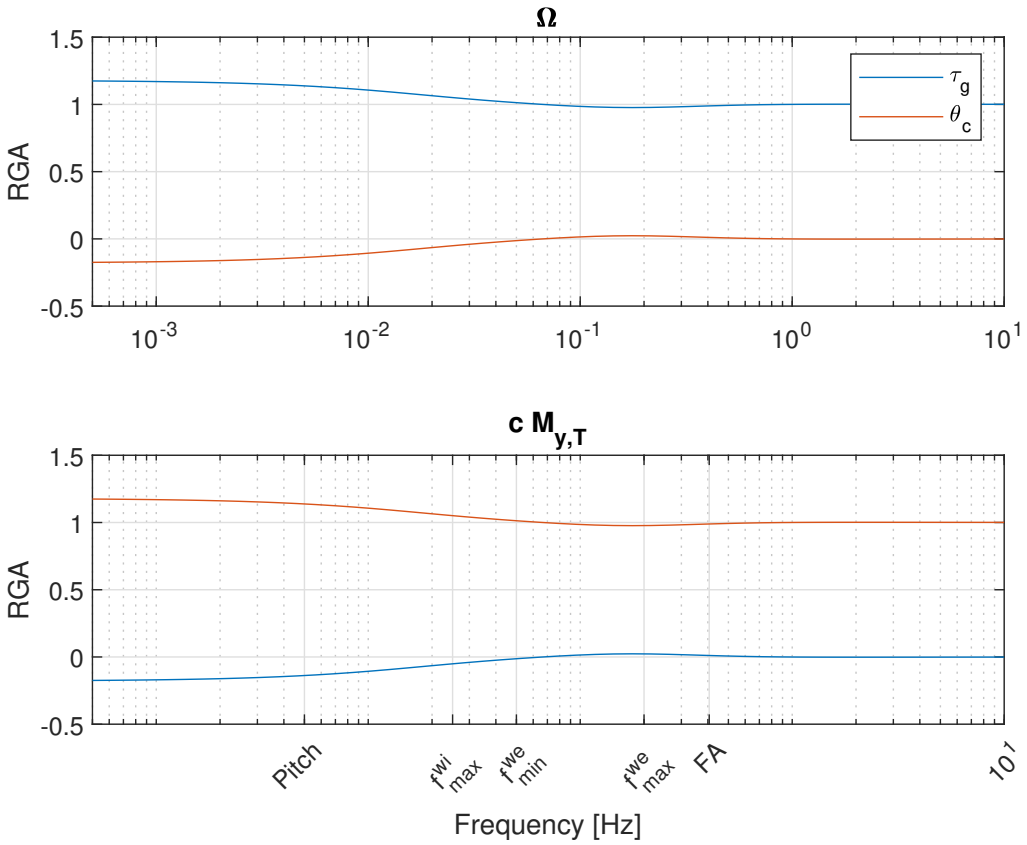

Figure 4-7: RGA in below-rated, as a function of frequency for the controlled system $\hat{G}_i$. Values close to one present a good pair for control.

Now lets consider the different operating points in Figure 4-8. At high winds ($v_0 > 17$), pitch-to-rotor control becomes dominant in the low frequencies. For example, looking at

$v_0 = 22m/s$, pitch-control is the best pair for frequencies lower then 0.085 Hz. For operating points with $v_0 \leq 17m/s$, torque-to-rotor control is always the best pair.

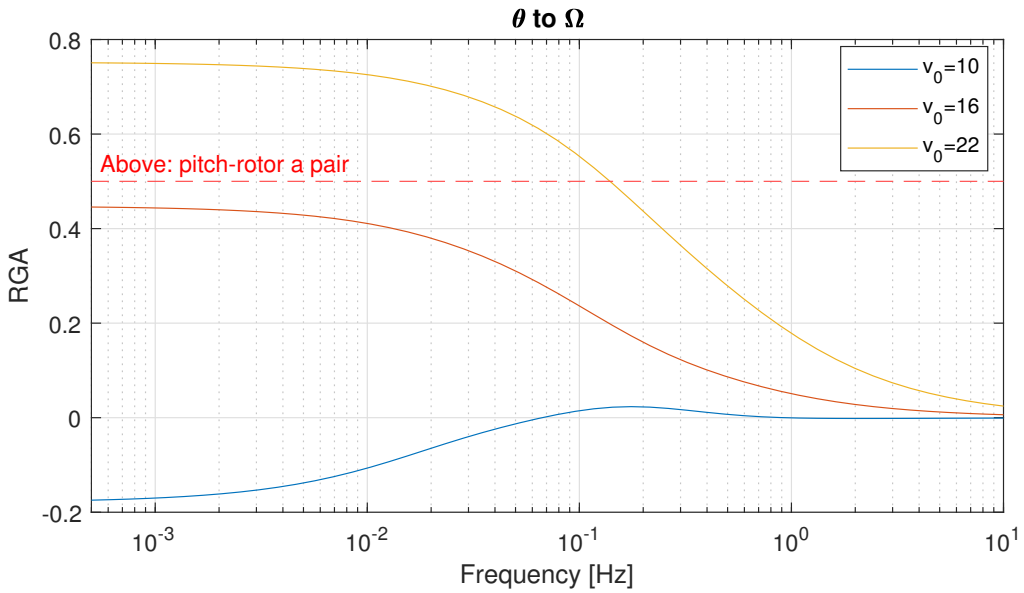

Figure 4-8: RGA for different operating points, from pitch-control to rotor speed. When the value is above 0.5, pitch control is a better pair then torque-control.

The increase of blade-pitch control sensitivity on the rotor speed, can be explained by looking at the blade frontal blade area. It is defined as $A_b \approx c_2 \cdot cos(\theta_0 + \Delta\theta)$, with c_2 is some geometry constant, $\theta_{c,0}$ the mean blade pitch and $\Delta\theta$ the pitch-control variations. Small variations of $\Delta\theta_c$ around $\theta_{c,0} = 0$ have little effect on A_b, while small variations around $\theta_{c,0} \approx 90$ have much more effect. The higher the mean with speed, the larger $\theta_{c,0}$ becomes. Therefore, in high wind speeds, pitch control becomes more effective.

4-2 Derivation of the control logic

The control logic is the architecture of the wave-FF controller. Presuming perfect wave-preview, a new category of possible designs arises. In this section, the control logic for the wave-FF controller is derived.

4-2-1 Selection of the controller

Classical FF control using an inverted plant is the most simple design. Suppose we have a system with an input u, a measurable disturbance d and some output y. Furthermore, suppose we have a linear model of the non-linear plant and full information of the incoming wave disturbance. The idea is to apply some input signal u based on the model, such that the disturbance signal d is compensated and y remains unaffected. The controller consists of a feedforward part and a feedback part. The FF part is used to reject the disturbance,

while the FB part provides robustness for model errors and measurement uncertainties. The classical FF control law is shown in the Laplace domain in Eq. (4-6).

$$u_{ff}(s) = -\hat{G}_{d\to y}(s) \cdot \hat{G}^{-1}_{u\to y}(s) \cdot d(s) \tag{4-6}$$

The control law consists of one transfer function from disturbance d to the compensated output y and one inverse transfer function from the control-input u to the compensated output y. To obtain compensation, the control action is negative. The result is a control signal u which compensates output variations y induced by the disturbance d.

The method also works for MIMO systems, as long as the outputs are non-contradicting, controllable, observable and the number of output channels equal to the number of input channels. The TripleSpar has two control inputs. Therefore, two outputs can be compensated for. For compensating more than two outputs, the system is under-actuated.

More advanced disturbance-accommodating control strategies exist as well. Inspiration can be obtained from LIDAR assisted wind control. A short literature survey on the subject provides plenty of good results. For example, by combining the FF and FB controllers (instead of separated) into one FB/FF controller, such as in [51] or [52]. This way, controllers can cooperate more smartly. However, it is much more complex in comparison to the baseline controller.

Furthermore, state-feedforward is interesting, because it allows optimising more than two objectives in some cost function. Also, the control input could be taken into account. Such a controller is showing promising results in [35]. Here, the wave-measurement can be added to the FB controller as if it is a regular model input.

Ultimately, linear model predictive control (MPC) seems to be a potential strategy. Using the wave preview, an optimal control signal can be calculated for multiple steps in advance. Unlike the wind model, the linearized wave-to-output model is merely linear over different operating points. One can therefore likely use the computationally lighter MPC instead of non-linear MPC. Good results on FOWTs are already found using this method [53].

Advanced wave-accommodating control strategies might lead to better performance than classical FF control. But to prove the potential of this new field, we want to keep it as simple as possible. The wave-accommodating controller will be designed using classical SISO FF, such that the method is proven in its most fundamental way. From there, extensions can be added for additional performance.

4-2-2 Feedforward control logic

The internal control logic of the FF controller is denoted in Figure 4-9. The expected disturbed output y_i and y_j (two channels) are estimated according the the CROLM exited by the disturbance input $\eta_0(t + t_d)$. These disturbed output are transformed into compensation inputs $u_{ff} = [\tau_{g,ff},\ \theta_{c,ff}]$ using the inverted plant and subtracted from the feedback signal for compensation.

The implementation of the wave-FF controller is shown in Figure 4-10. Note the similarities with the baseline control logic from Figure 2-2. The new logic consists of the baseline logic, plus a control signal based on the wave measurement. The plant G is divided into sub-plants.

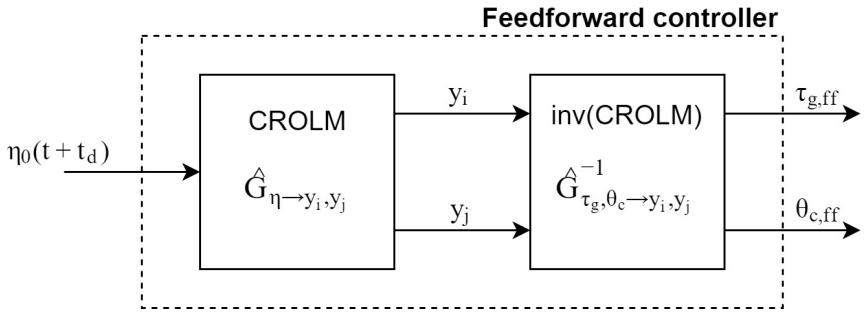

Figure 4-9: Control logic of a SIMO feedforward controller. A disturbing wave is transformed to resulting outputs. This output is transformed to the required input to compensate it.

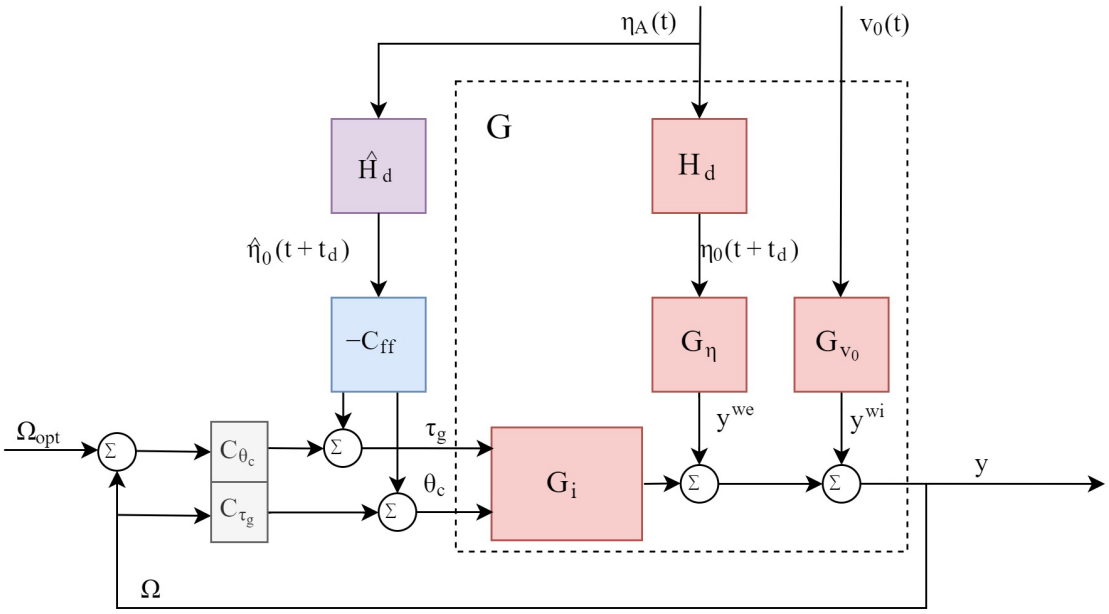

Figure 4-10: Control logic of the baseline controller complemented with the wave-FF controller.

Note that G denotes the real plant and $\hat{G}$ the CROLM. Furthermore, H_d denotes the natural wave propagation from $\eta_A(t)$ to $\eta_0(t+t_d)$ and $\hat{H}_d$ the wave predictor from Section 3-4-2.

The wave-FF controller works as follows. Wave elevation $\eta_A(t)$ is measured in point A, at L meter in front of the TripleSpar. According to our findings in Section 3-4-2, L is chosen at 300 m[3]. The wave elevation $\eta_A(t)$ is fed into the wave predictor $\hat{H}_d$ (defined in Section 3-4-2), providing the predicted wave preview $\hat{\eta}_0(t+t_d)$. This wave preview is fed into the wave-FF controller to calculate the FF control component $u_{ff}(t)$.

The effect of this control logic can be shown by the Laplace equations. Suppose no FF is applied in Figure 4-10 (i.e. $C_{ff}=0$) and no disturbances are present. Only pitch or torque control is active at the same time. For now, suppose pitch control is active. The control loop

[3]This way we have a wave preview up to $T = 13.5$s period, for $t_d = 10$ seconds in advance

is SISO using θ_c and output y_j. The baseline CL transfer function (TF) becomes:

$$Y(s) = \frac{G(s)C_{\theta c}(s)\Omega_{opt}(s)}{I + G(s)C_{\theta c}(s)} \tag{4-7}$$

Next, the wind- and wave disturbances are added. The transfer function becomes:

$$Y(s) = \frac{G(s)C_{\theta_c}(s)\Omega_{opt}(s) + G_\eta(s)H_d(s)\eta_A(s) + G_{v_0}v_0(s)}{I + G(s)C_{\theta_c}(s)} \tag{4-8}$$

Now the wave-FF control law is added using $u_{ff}(s) = -\hat{G}^{-1}_{u_i \to y_j}(s)\hat{G}_\eta(s)\eta_{0,p}(s)$. Here u_i is the FF-control input, y_j the compensated output and $\eta_{0,p}(s)$ is the predicted surface elevation. Adding this to the baseline system similar to Figure 4-10, the transfer function becomes:

$$Y(s) = \frac{G(s)C_{\theta_c}(s)\Omega_{opt}(s) + G_\eta(s)H_d(s)\eta_A(s) - G_{u_i}(s)C_{ff}(s)\hat{H}_d(s)\eta_A(s) + G_{v_0}v_0(s)}{I + G(s)C_{\theta_c}(s)} \tag{4-9}$$

$$Y(s) = \frac{G(s)C_{\theta_c}(s)\Omega_{opt}(s) + \Big(G_\eta(s)H_d(s) - G_{u_i}(s)C_{ff}(s)\hat{H}_d(s)\Big)\eta_A(s) + G_{v_0}v_0(s)}{I + G(s)C_{\theta_c}(s)} \tag{4-10}$$

The remaining wave-induced output y_j can be written as follows, where the control law is substituted.

$$Y_j^{we}(s) = \frac{(G_\eta(s)H_d(s) - G_{u_i}(s)\hat{G}^{-1}_{u_i}(s)\hat{G}_\eta(s)\hat{H}_d(s))\eta_A(s)}{I + G(s)C_{\theta c}(s)} \tag{4-11}$$

The wave-induced output y_j is fully compensated if the following equation holds. This is the case if $\hat{G} \approx G$.

$$G_\eta(s)H_d(s) \approx G_{u_i}(s)\hat{G}^{-1}_{u_i}(s)\hat{G}_\eta(s)\hat{H}_d(s) \tag{4-12}$$

Note that a powerful feature of this logic is that the baseline control logic is preserved. Moreover, a multiplication of stable systems does not become unstable. The FF control action does not occur in the denominator. Supposing stability of the FF controller C_{ff} and a stable disturbance η_A, stability is unaffected. Furthermore, all well-evaluated programs such as fault detection, gain-scheduling, etc. are unaffected.

4-3 Feed forward controller design for rotor speed stability

The only remaining question is what output y_j to optimise. Based on the findings in Chapter 2, one would say the tower-base bending moment load cycles $cM_{y,T}$, because waves affect it the most. However, to compensate tower bending moment, requires moderate pitch action, because it is insensitive to control input (found in Section 4-1). Moreover, pitch action to reduce loads would also induce rotor variations. Additional generator torque is required to compensate for these rotor speed variations[4]. Thus, collective-pitch FF load reduction works

[4]One can use torque control also in above-rated situations, as long as the mean value is zero and the amplitude is not too large

only in combination with FF torque control for rotor stability. This is an example of a *multi-objective* FF controller. Section 4-3-3 will elaborate on this controller, by designing a simple multi-objective FF controller for tower-base load reduction.

For now, the objective is kept more simple. The second-most important control objective is power stability, obtained by rotor stability. This objective has been found more simple, mainly because the generator torque regulates the rotor speed with minimum effect on additional output channels. Moreover, it is the same control objective as regular FB control.

Hence, the first goal is to minimise wave-induced variations in Ω. Two controllers are designed, for different operating points. One using torque τ_g control and one using pitch θ_c control. According to the findings in Section 4-1-3, the torque controller is active for low and moderate wind speeds $\bar{v}_0 \leq 17$ whereas the pitch-controller is active in high wind speeds ($\bar{v}_0 > 17$).

4-3-1 Generator torque FF control

The control logic of Section 4-2 is implemented in Simulink. The plant is the same CROLM as used for the FF controller (i.e. $G := \hat{G}$). This should provide perfect disturbance rejection. Furthermore, perfect laminar wind $v_0 = 8$ is used and waves are modelled irregular according to the JONSWAP spectrum. For the design, the plant is kept simple. For verification, high-fidelity simulations are used in the next chapter.

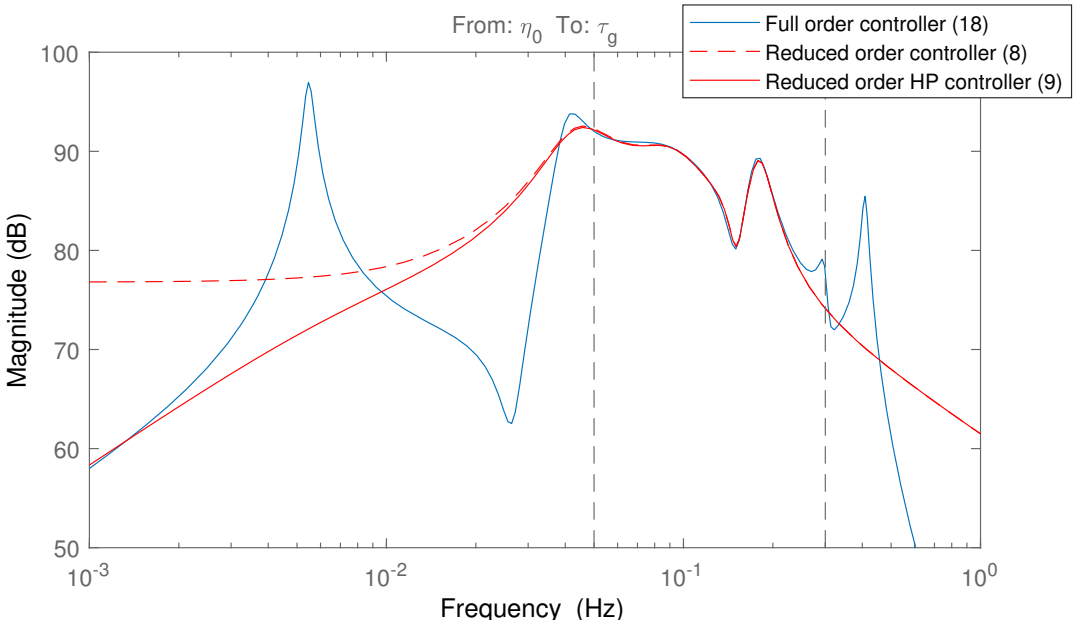

Figure 4-11: Bode plot of the torque controller after loop shaping. Full order controller (blue), the reduced-order controller (red dashed) and the final wave-FF controller (red solid)

Using the inverted plant of Eq. (4-6) and substituting $y = \Omega$ and $u = \tau_g$, the so-called *full-order FF controller* is obtained in Eq. (4-13), shown in Figure 4-11 in blue. The full-order FF controller is order $N = 18$ after pole-zero cancellation. Notice that in real systems, pole-zero cancellation is not recommended as a result of model uncertainties. However, this controller

is so far only virtual. We know the exact position of the poles and zeros. Therefore pole-zero cancellation can safely be applied.

$$u_{ff}(s) = -G_{d\to\Omega}(s) \cdot G^{-1}_{\tau_g\to\Omega}(s) \cdot \eta_{0,p} \tag{4-13}$$

An 18-order controller may be more complex than necessary. The black lines in Figure 4-11 indicate the wave typical wave frequency bandwidth f^{we}. Much complexity is contained outside this region. Therefore, a model reduction is applied using state elimination [54]. Matlab function *balred* is used to apply this operation. The relevant frequency range is set to f^{we}. An order of $N = 8$ is found to be the lowest order to approximate the full-order controller nearly perfect in f^{we}, shown by the red dotted line. It is still significant in the low-frequency range. The wave-FF controller should only react to real physical waves. Therefore, a first-order high-pass filter is applied at $f = 1/25$ Hz. The final controller C_{ff} is shown by the red solid line, denoting a 9^{th} order state-space system. As a result of the high-pass filter, the phase is increased by 90 for $f << 1/25$ Hz. This does not influence performance.

The controller C_{ff} consists more poles (9) than zeros (8). Therefore, it is strictly proper [28]. The pole-zero map is shown in Figure 4-12. Since all poles are in the LHP, the controller is stable. The RHP zeros do not become RHP poles, because C_{ff} is only present in the numerator.

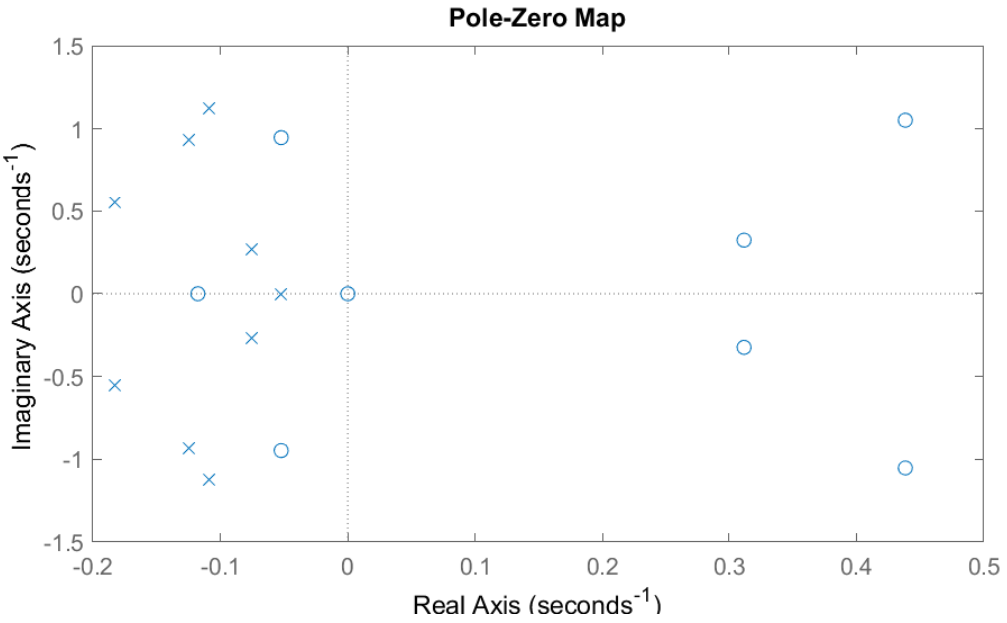

Figure 4-12: Pole-zero map of the filtered, reduced-order wave-FF controller C_{ff}.

A time simulation of this torque controller included in the control logic of Figure 4-10 is shown in Figure 4-13. The rotor variations are small because the wind is presumed to be steady. This implies that the only external disturbances are wave disturbances. The rotor-speed variations Ω is nearly-zero when using FF, at the cost of slightly more control input τ_g. By tuning a FF proportional gain $g := [0, 1]$ down, the control action is reduced. Some values of g allow a decrease in both rotor speed Ω and control action τ_g. Furthermore, the

controller reacts slightly faster for all values of g. When the full-order FF controller is used, rotor variations are found to be zero. The leftover rotor speed variations are the result of the model reduction.

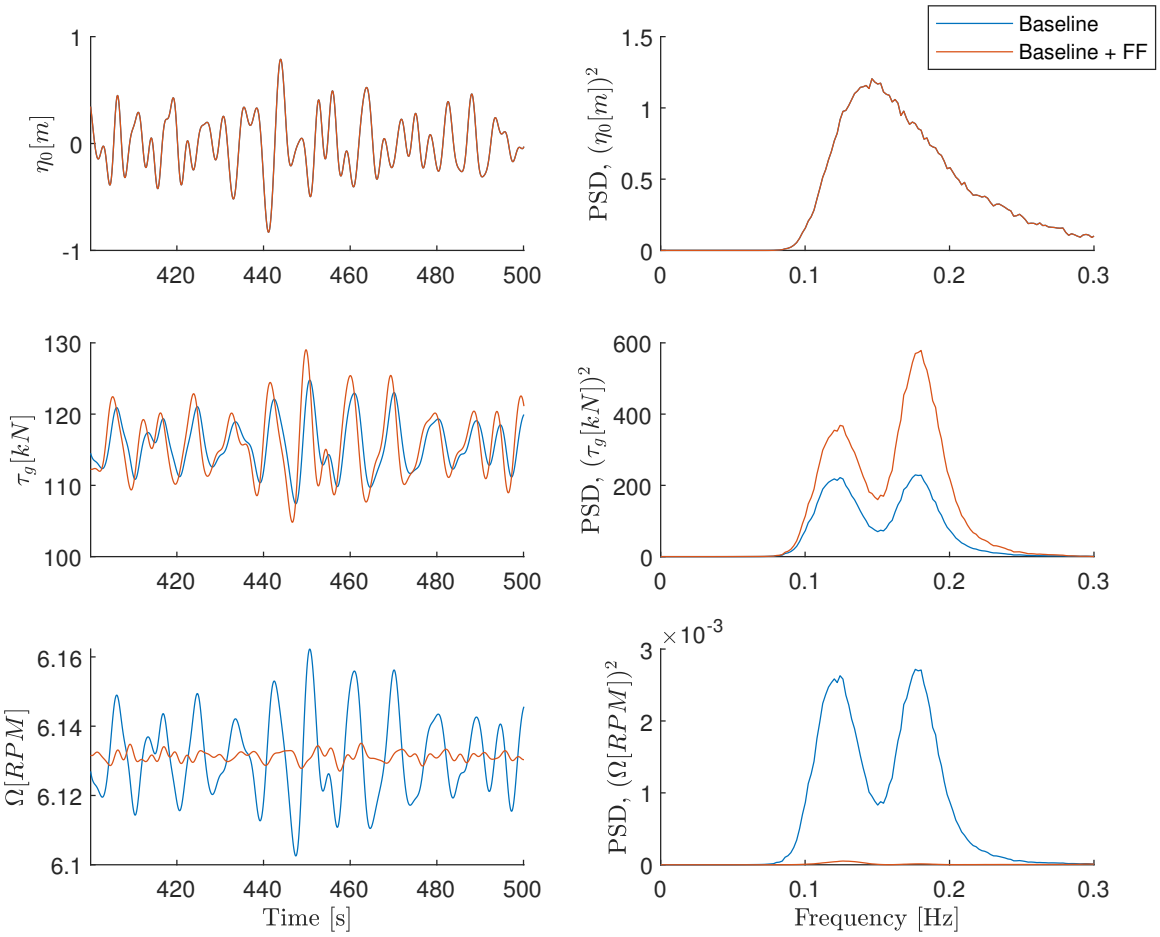

Figure 4-13: Simulation comparison between the baseline controller (blue) and the wave-FF torque-controller (orange) on a linear plant. Load case 2.

4-3-2 Collective pitch FF control

The same steps are applied to design a FF pitch controller. This controller reduces rotor variations $y_j = \Omega$ using collective pitch control $u_i = \theta_c$. The full order controller is defined by Eq. (4-14). For this design, above-rated operating point $\bar{v}_0 = 18$ is used.

$$u_{ff}(s) = -G_{\eta\to\Omega}(s) \cdot G^{-1}_{\theta_c\to\Omega}(s) \cdot \eta_{0,p}(s) \tag{4-14}$$

The full-order controller with $N = 18$ is found to be unstable, having one pole pair in $s = 0.015 \pm 0.25i$. To stabilise it with fewest influence on the dynamics, the unstable poles are cancelled using two zeros and replaced by two new (LHP) poles. The operation is shown in Eq. (4-15), where $p_1 = 0.015 + 0.25i$ and $p_2 = 0.015 - 0.25i$. The poles have been mirrored across the imaginary axis.

$$S(s) = \frac{(s - p_1)(s - p_2)}{(s + p_1)(s + p_2)} \tag{4-15}$$

A comparison of the transfer functions is shown in Figure 4-14. The original controller C_{full} (blue) and the stable system $C_{full,s}$ (green dotted) show a near-perfect match, except at the 0.040 Hz peak. Next, the model is reduced. An order of $N = 12$ is the least possible showing a good match. The new controller (red dashed) is proper, but again a high-pass filter is required to reduce the low-frequent sensitivity. The final controller C_{ff} (red solid) is shown in the figure.

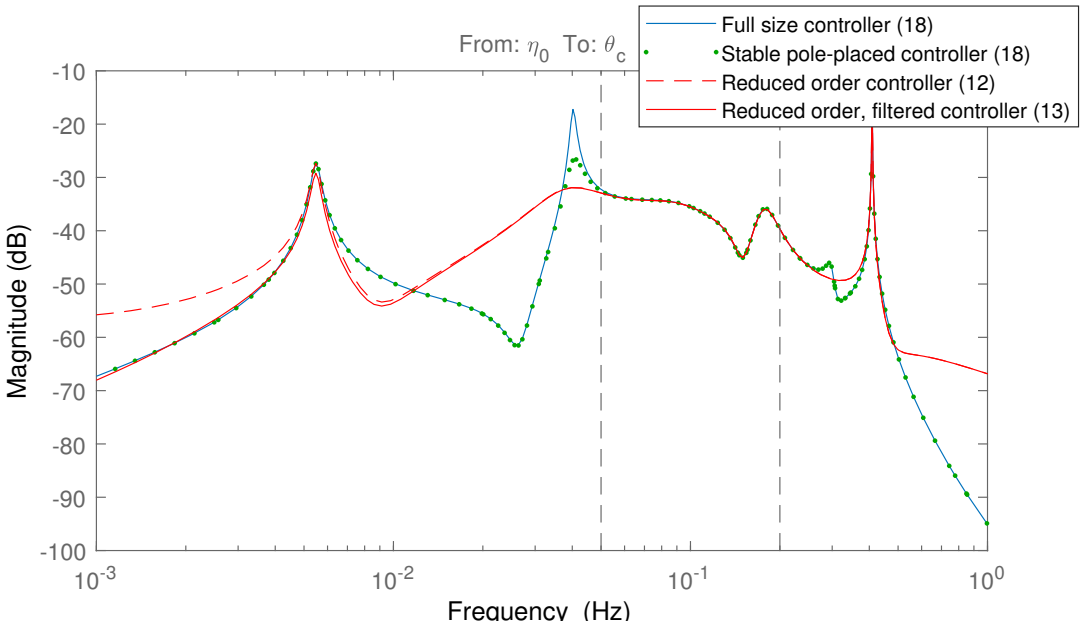

Figure 4-14: Bode plot of the FF pitch controller after loop shaping. Full order controller (blue), stabilised controller (green dots), the reduced-order controller (red dashed) and the final wave-FF controller (red solid)

The simulation comparison between baseline and baseline+FF is show in Figure 4-15. Almost all wave-induced rotor speed variations are compensated at the cost of significant extra blade pitch variations. By adding a gain $g = [0, 1]$ on the FF control signal, one can tune the controller gain down to reduce control input.

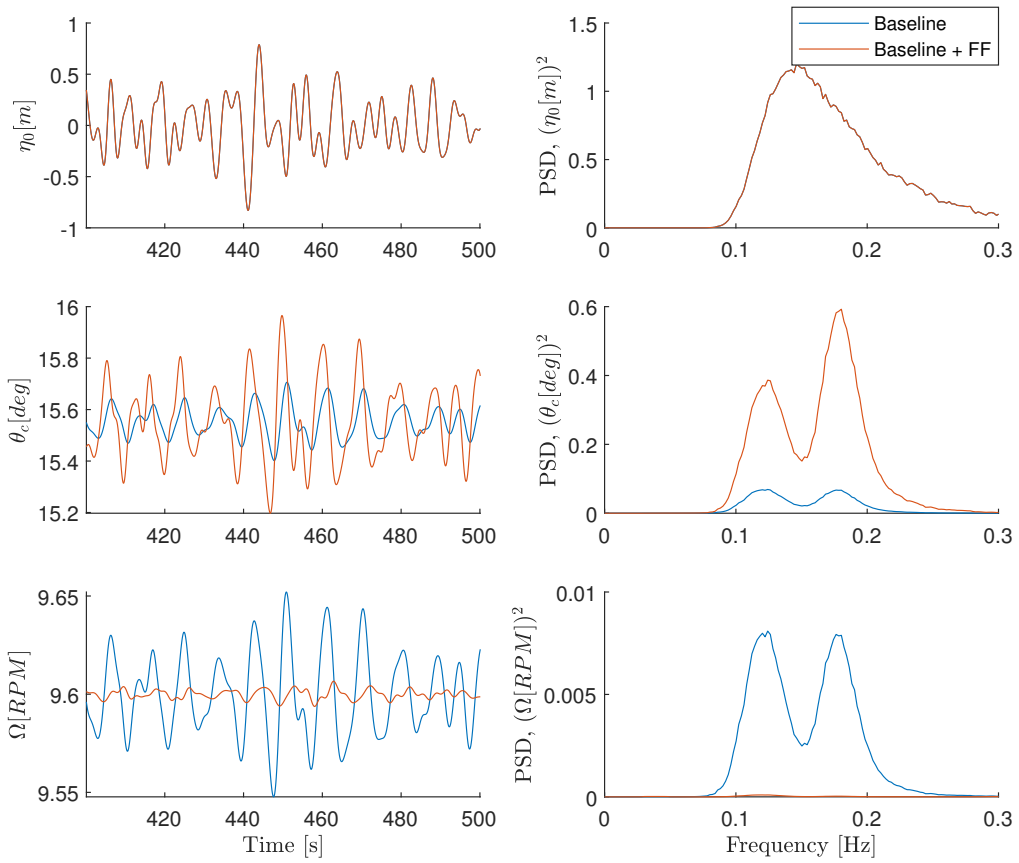

Figure 4-15: Simulation comparison between the baseline controller (blue) and the wave-FF pitch controller (orange) on a linear plant.

4-3-3 Multi objective FF control

For proof of concept, the method is extended to a SIMO wave-FF controller. The second control objective is to reduce tower deflection cycles $\ddot{x}_d$. This reduces tower base loads $M_{y,T}$, similar to Section 4-1. The design procedure of stabilising, order reduction and filtering is similar to the two previous controllers and will not be repeated. The full order controller and the reduced-order controller bode plots are shown in Figure 4-16.

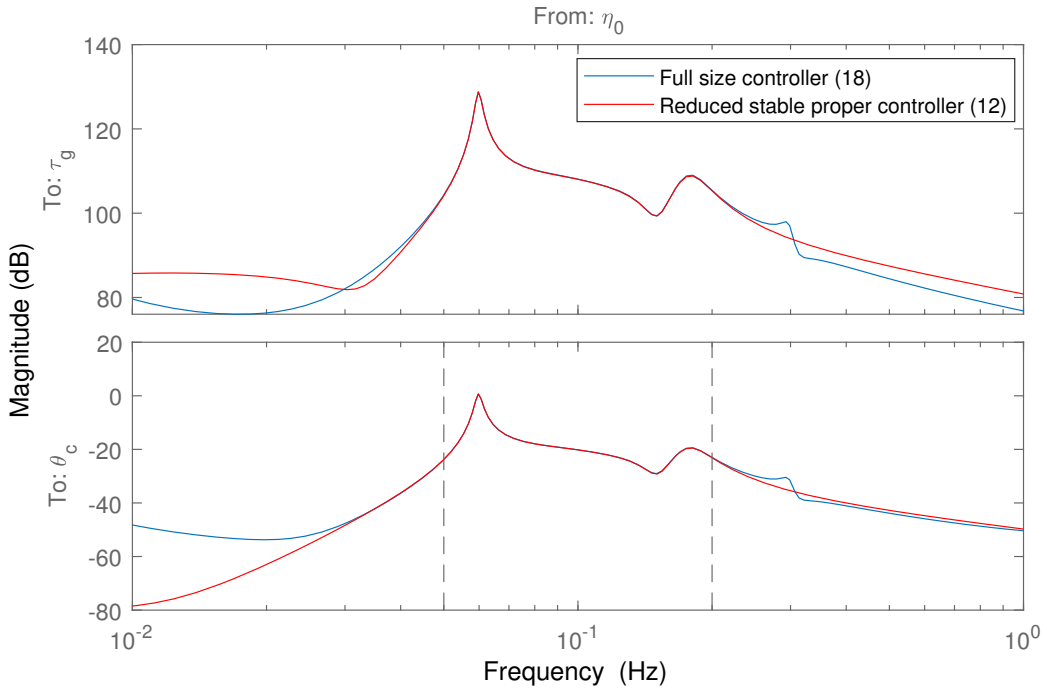

Figure 4-16: Bode comparison of the full order model and the reduced order model for the multi-objective load controller.

The simulation results are shown in Figure 4-17. Both the rotor speed and tower deflection are now nearly fully compensated by the FF controller (yellow) However, the compensation of tower deflection requires a large control action. As an alternative, an additional FF controller is simulated using gain $g = 0.5$. The control action power is halved and the output power is halved (red). Since the power is quadratic, the FF time series is only decreased by a ratio of $1/\sqrt{2}$.

The multi-objective FF controller performs excellently on the linear plant. Using moderate control, performance is increased significantly. A preview of the potential of this framework is shown. The next step is to test the controller using high-fidelity simulations in FAST. However, we will first focus on the development of the SISO controller, to prove the wave-FF framework in its most fundamental way. The multi-objective controller is put on hold, to value quality over quantity. The pitch- and torque wave-FF controllers are used for further analysis.

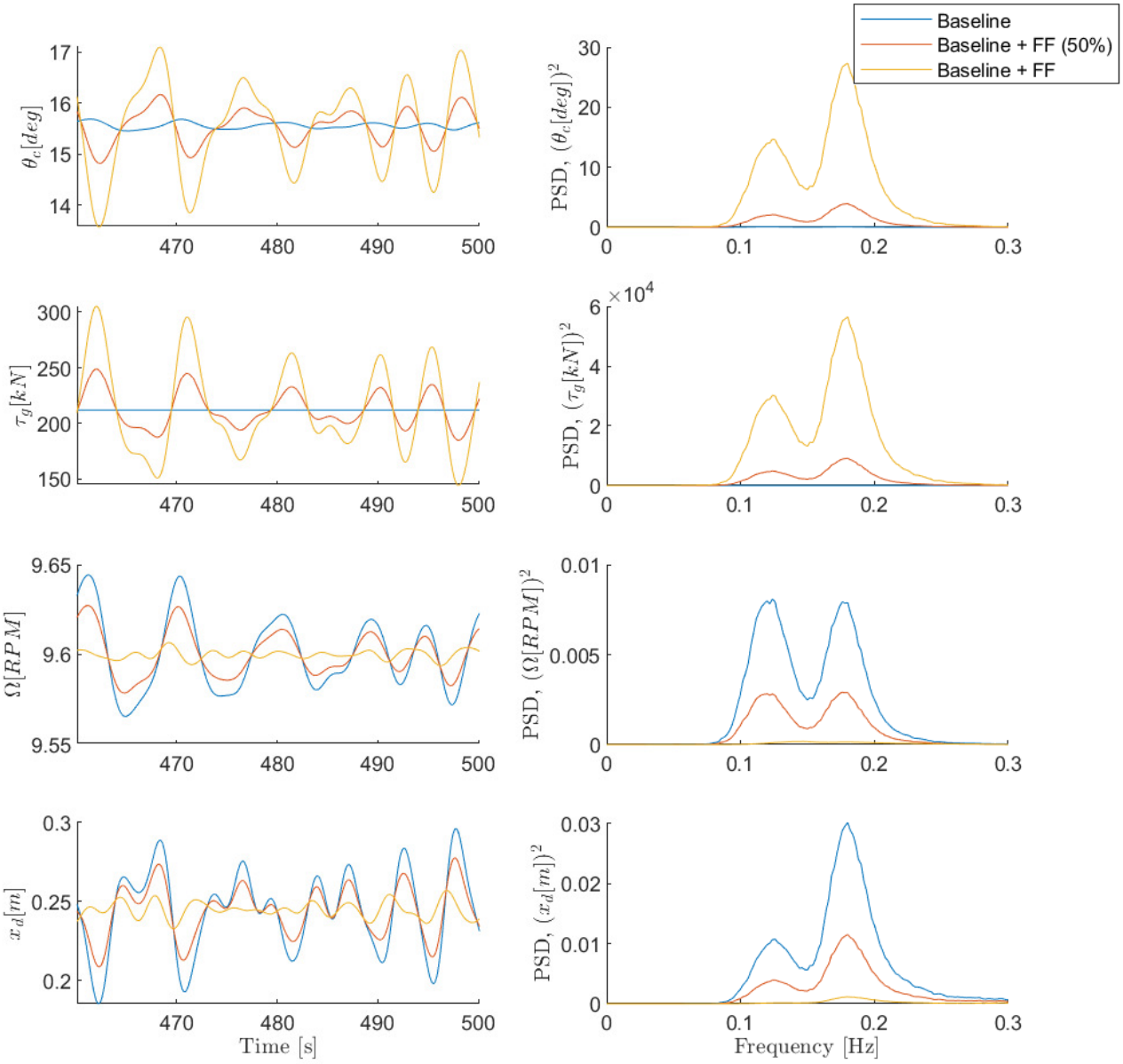

Figure 4-17: Simulation of the multi-objective controller. Left a part of the time-series, right the PSD

4-4 Design procedure for the wave-FF controller

All steps to design a wave-FF controller have now been performed. Even-though the FF controller is simple, the workflow to design it is more complex. Furthermore, these steps have only been applied for one reference turbine and one output y_j. To hand the framework to research, a general method is given in Figure 4-18.

It summarises the complex design procedure into a 9-step guide, varying from model building to controller design. The illustration is merely an overview. For a detailed description of the steps or full-sized images, please refer to the relevant section. The images contained in the procedure are solely for illustration. The figure provides an understanding of the concepts in relation to each other.

4-5 Conclusions

The CROLM from Chapter 3 has been utilised to design a wave-FF controller. Linear analysis gave new insight into the dynamics of the 10 MW TripleSpar FOWT. To reduce rotor speed variations, torque control is best suited in low and moderate winds. For stronger winds ($\bar{v}_0 > 17$) m/s, pitch-control is more effective. To reduce tower loads, pitch control is best suited. However, control is not very effective on tower loads. Reducing these requires moderate pitch-control. Moreover, additional torque control is required to compensate for pitch-induced rotor speed variations.

A simple FF control logic for compensating wave-induced dynamics is derived. This logic uses the (inverted) CROLM. It allows compensation of one or two output channels. A powerful feature of this logic is that the FF is separated from of the FB controller. Therefore, all well-evaluated properties of baseline control remain. The stability is unaffected and advanced (baseline) control strategies are not replaced. Therefore, the wave-FF logic is of low complexity with respect to other FB control strategies.

Three FF controllers are designed using this control logic and are tested on the CROLM plant. Loop-shaping is used to make these controllers stable, proper and of lower-order. The first controller compensates rotor speed variations Ω using torque control τ_g. A 9^{th} order model has shown sufficient for nearly full compensation of Ω. The second controller compensates rotor variations using collective pitch control θ_c. A 12^{th} order model has shown sufficient for nearly full compensation. Both controllers require only minor additional control action. The third controller is multi-objective, compensating tower-base load cycles $M_{y,T}$ and rotor speed variations Ω, using both control inputs. To fully compensate both outputs goes at the cost of moderate control actions. Therefore, the controller gain is tuned down to apply only 50% control action. This controller shows the potential of multi-objective FF control. However, only the first two controllers are used for further analysis.

Finally, to extend this research from a single case-study to a generalised approach, the design procedure to derive a wave-FF controller is captured in Figure 4-18. This provides a brief step-by-step guide on how to derive the wave-FF controller for some other FOWT or control objective.

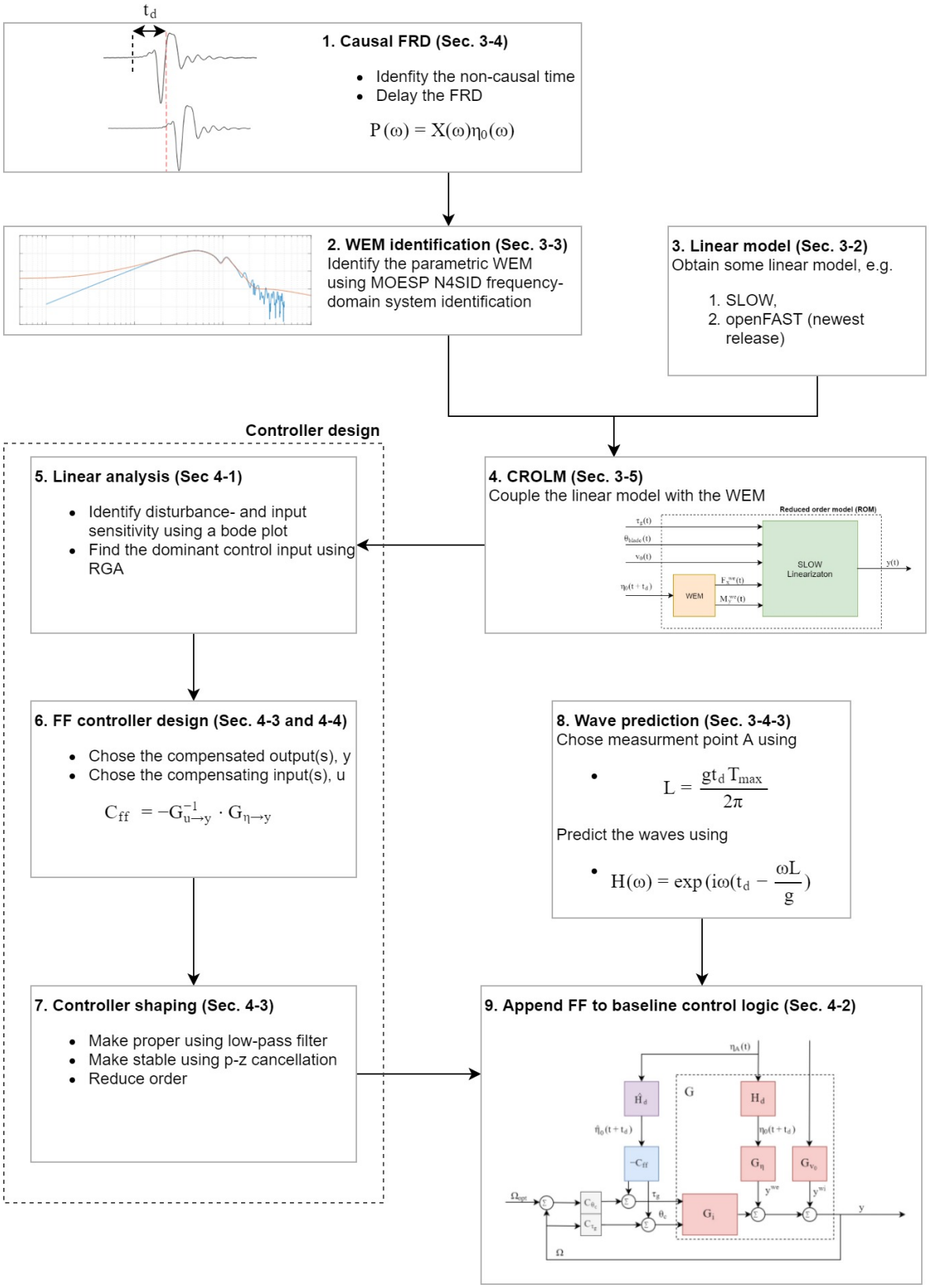

Figure 4-18: Design procedure to design a wave-FF controller some arbitrary FOWT using some arbitrary control objective.

Chapter 5

Simulation results and experimental testing

In this chapter, the wave-FF controllers are subjected to high-fidelity simulations in FAST. The configuration is similar as in Chapter 2, using the same load cases (Table 2-2) and performance metrics (Table 2-3). The objective is to measure the performance of the controller in a realistic configuration, thereby validating the effectiveness of the new framework.

The torque controller is used in load cases 1, 2, 3, 4 and 5 whereas the pitch controller is used in load cases 6 and 7, according to Section 4-1. The controller is computed for each load case, based on the CROLM and loop shaping corresponding to the operating point. A gain g is added to each FF controller, to reduce the control action. This maintains realistic control action.

Two controller-designs are discussed. The first balances the performance with the control inputs, such that inputs do not exceed regular values. The control action of this controller is very realistic. It is named the balanced performance (BP) wave-FF controller. The second controller is designed to reduce as much rotor variations as possible, without taking the required control action into account. Because the control action may become aggressive, this design is currently less realistic. This controller is named the maximum performance (MP) wave-FF controller.

The FF controller is compared to the baseline controller. Remember how $P^{wa} = P_{bl} - P_{bl,no-waves}$ is presumed to be wave-induced, similar to in Chapter 2. Furthermore, setup (3) will act as an upper limit for wave-FF control. The following setups will be simulated.

1. Baseline control
2. Baseline control with BP wave-FF control
3. Baseline control with MP wave-FF control
4. Baseline control in still water

Ultimately, scaled experiments were carried out. A scaled floating platform has been validated in a wave basin. The waves have been measured in front of the platform and are used for control. Unfortunately, the test was not sufficient to verify the controller. The experiments are described in this chapter.

The outline of this chapter is as follows. The BP wave-FF controller is validated in Section 5-1. The MP is validated in Section 5-2. Moreover, the baseline, BP and MP controller performances are compared in this section. Lastly, the sacaled experiment is described in Section 5-3.

5-1 Results of a balanced-performance wave-feedforward controller

The BP controller is implemented in the control logic. The gains g are tuned such that control input does not exceed values the regular values. Only for load case 3 and 4 the tuning is arbitrary, because FB control uses pitch control whereas FF control used generator torque. Table 5-1 shows the control region for each controller. The controller gains for the BP and MP are indicated for each load case.

Table 5-1: Controller and FF gain per load case. In load case 3 & 4, both pitch-control (FB) and torque-control (FF) are used.

Load case	1	2	3	4	5	6	7
Rated	Below	Below	Below	Above	Above	Above	Above
FB	τ_g	τ_g	τ_g	θ_c	θ_c	θ_c	θ_c
FF	τ_g	τ_g	τ_g	τ_g	τ_g	θ_c	θ_c
BP gain	0.25	0.12	0.075	0.267	0.28	0.070	0.060
MP gain	0.25	0.35	0.35	0.65	0.73	0.700	0.62

The high-fidelity simulations are implemented. Table 5-2 shows the Weibull performance metrics for the setups. By adding BP FF control, the power production is increased by 0.10%. Furthermore, the rotor speed variations are reduced by 11%, blade speed variations are reduced by 25%, the shaft DEL is increased by 31% and no significant effect on tower DEL and blade DEL is found. The reduction in power variations is found to be equivalent to the reduction in rotor speed variations.

Table 5-2: Performance metrics for different configurations.

	Mean power [MW]	Rotor varience [RPM]	Mean blade speed [rad/s]	DEL ($M_{y,T}$) [Nm]	DEL (M_{blade}) [Nm]	DEL (T_{LSS}) [Nm]
Baseline	6090	0.0332	0.00337	63900	3870	548
Baseline+FF	6096	0.0295	0.00254	63600	3790	722
Baseline (no waves)	6106	0.0235	0.000811	11700	2910	416

Figure 5-1 shows the performance of wave-FF control relative to baseline control per load case i. The performance is computed as $P_i = \frac{P_{ff}}{P_{bl}} - 1$. Values below zero indicate a decrease

as a result of FF. The extreme shaft DEL values for load case 4 (103%) and 5 (175%), are a result of FF torque control additional to regular pitch control. Therefore, their values are difficult to compare in a relative way.

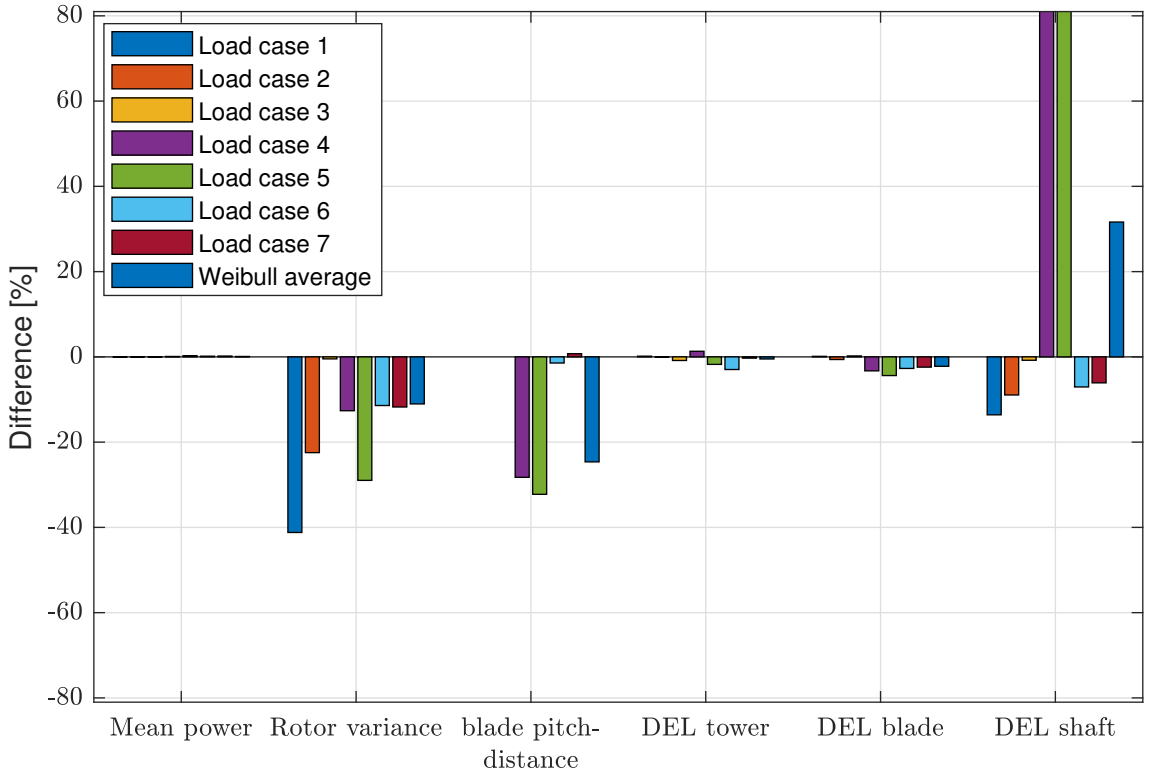

Figure 5-1: Performance difference, when extending baseline control with a wave-FF controller.

Figure 5-2 shows the so-called normalised performance P_n using Eq. (5-1). Here 100% is equal to baseline performance, 0% is equal to still water performance and P_{ff} is the wave-FF performance indicated in the plot. The closer P_{ff} is to zero, the more wave-induced effects are compensated. It is found 30% of the wave-induced power-loss is compensated and 66% of the wave-induced rotor speed variations are compensated.

$$P_n = \frac{P_{ff} - P_{no}}{P_{bl} - P_{no}} \tag{5-1}$$

For load case 1 and 2, the results are outstanding. In load case 1, the wave-induced rotor speed variations are nearly fully compensated (5% remain, Figure 5-2) while requiring 32% less control action variations. The total rotor speed variation is reduced by 41% and 22% in these load cases.
For load case 3, no significant improvement (0.5%) on the baseline is obtained, even though the normalised performance is 57%. The difference between waves and no waves is very small in this load case (demonstrated in Figure 4-4). This has the largest negative effect on the

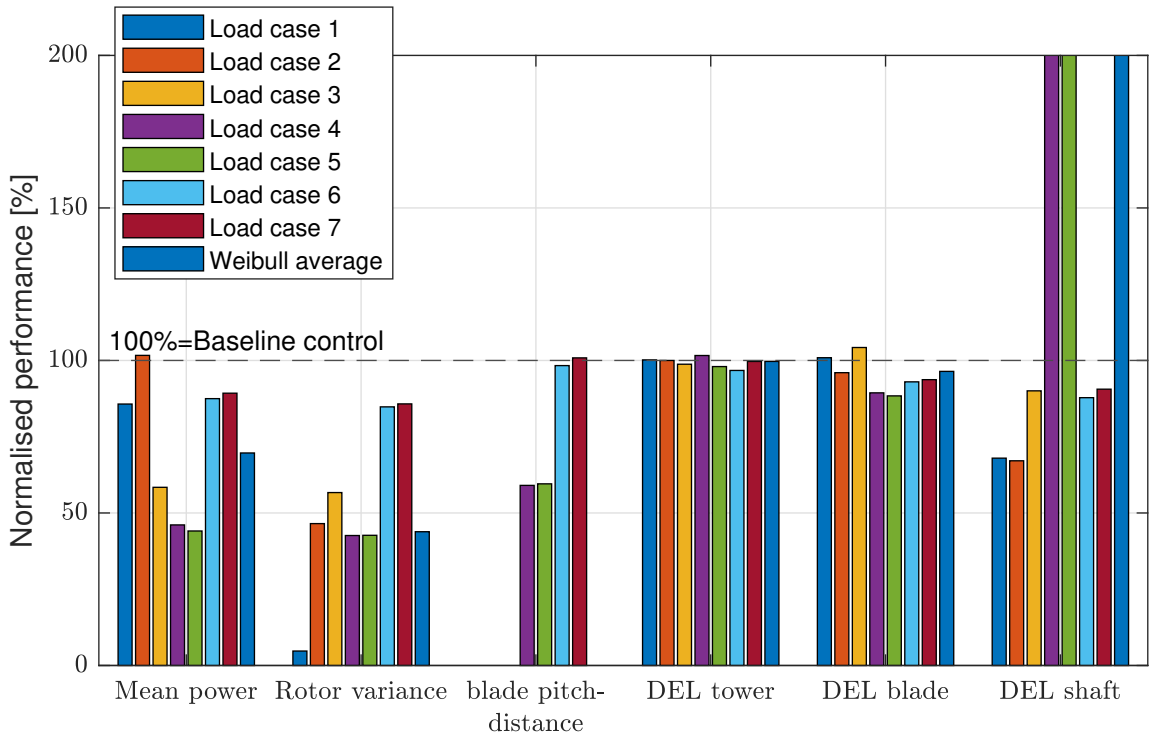

Figure 5-2: Normalised performance. i.e. amount of remaining *wave-induced* negative effects. 100% is equivalent to regular baseline performance, 0% is equivalent to baseline control in still water. The closes the value is to zero, the better.

Weibull average value.
In load cases 4 and 5, the baseline controller is using pitch-control while the FF controller is using torque-control. Therefore, the torque-control action takes extreme values compared to baseline control, while the pitch action is reduced.
For all load cases, rotor speed could be decreased further at the cost of additional control input by tuning the FF gain g. Especially in extreme loads, more compensation can be realised by using more control input. For a thorough overview of the performance, the global Weibull-averaged performance is summarised in Figure 5-3.

Figure 5-4 shows the last 50 seconds of the time series and the PSD of the simulation using load case one. The generator torque acts much faster. This is why we observe higher performance using less control action. The wave-FF controller almost fully compensates all wave-induced rotor variations. In the PSD, only the performance at frequencies between 0.8to 0.25 Hz is affected. This is the wave-excitation frequency range f^{we}. The low-frequency range (f_{wi}) is unaffected by wave-FF control.

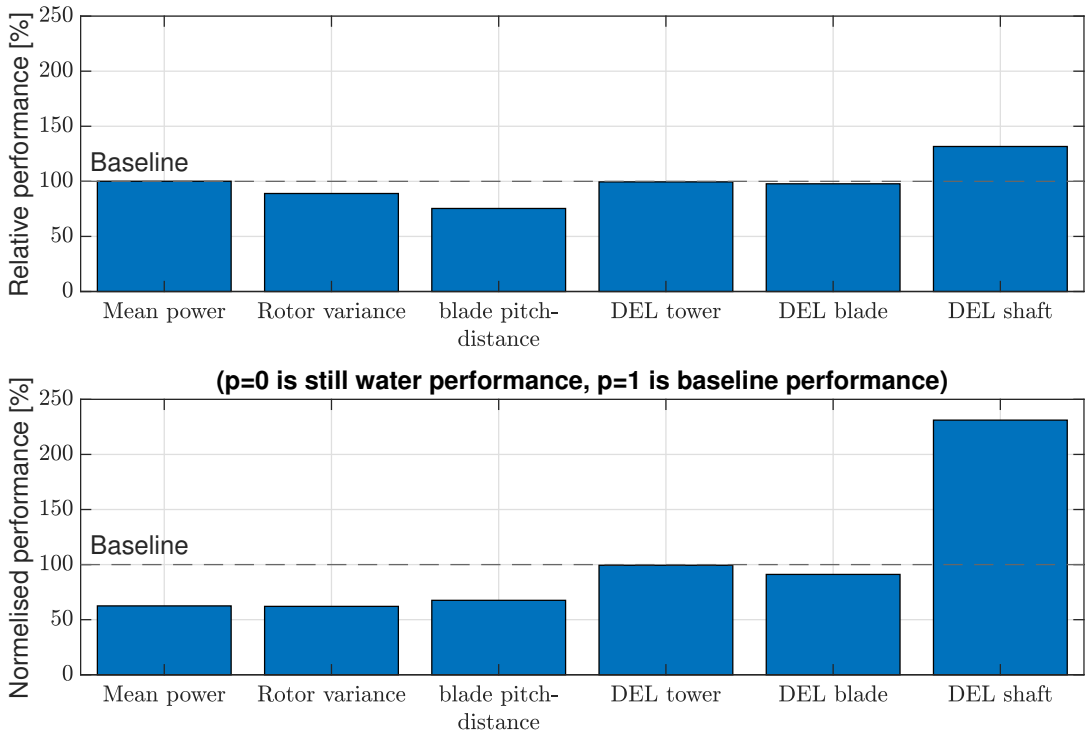

Figure 5-3: Weibull averaged performance of the BP controller, with respect to baseline control. Top: relative performance, i.e. amount of remaining negative effects. Bottom: normalised performance, i.e. amount of remaining *wave-induced* negative effects.

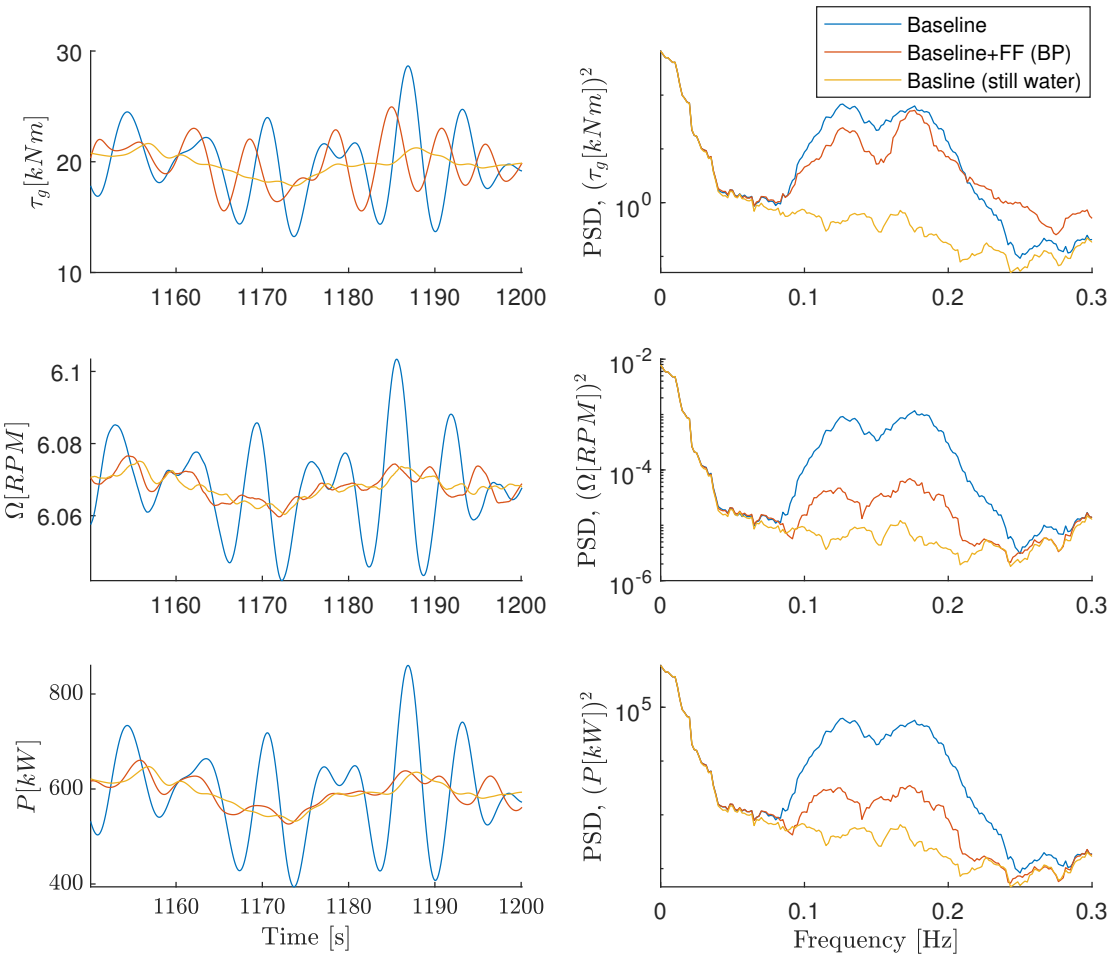

Figure 5-4: Simulation analysis on a 600s time series using load case 1. Left a part of the time series, right the PSD showing baseline control (blue), baseline+FF control (orange) and baseline in still water (yellow).

5-2 Results of a maximum-performance wave-feedforward controller

The BP wave-FF controller shows moderate improvement at the cost of limited additional control. However, for the moderate and high load cases, sensitivity to control drops such that only little improvement is obtained. The BP controller gains were tuned down such that the control action does not exceed current values. In this section, a MP controller is tuned. The goal is to reduce rotor speed variations as much as possible without balancing the required control inputs.

Figure 5-5 shows the Weibull averaged performance values. The top shows the relative performance to baseline, the bottom the performance on normalised wave-induced performance. Using the maximum gains, 27% of the rotor speed variations are reduced, equivalent to 92% of all wave-induced rotor speed variations. Again, reductions in power variation are of similar size. Furthermore, the power production is 0.14% increased, the mean pitch-action (mean blade speed) is reduced by 13%, the tower DEL is decreased by 1% and the blade DEL by 7%. On the downside, the shaft DEL is increased by 150%.

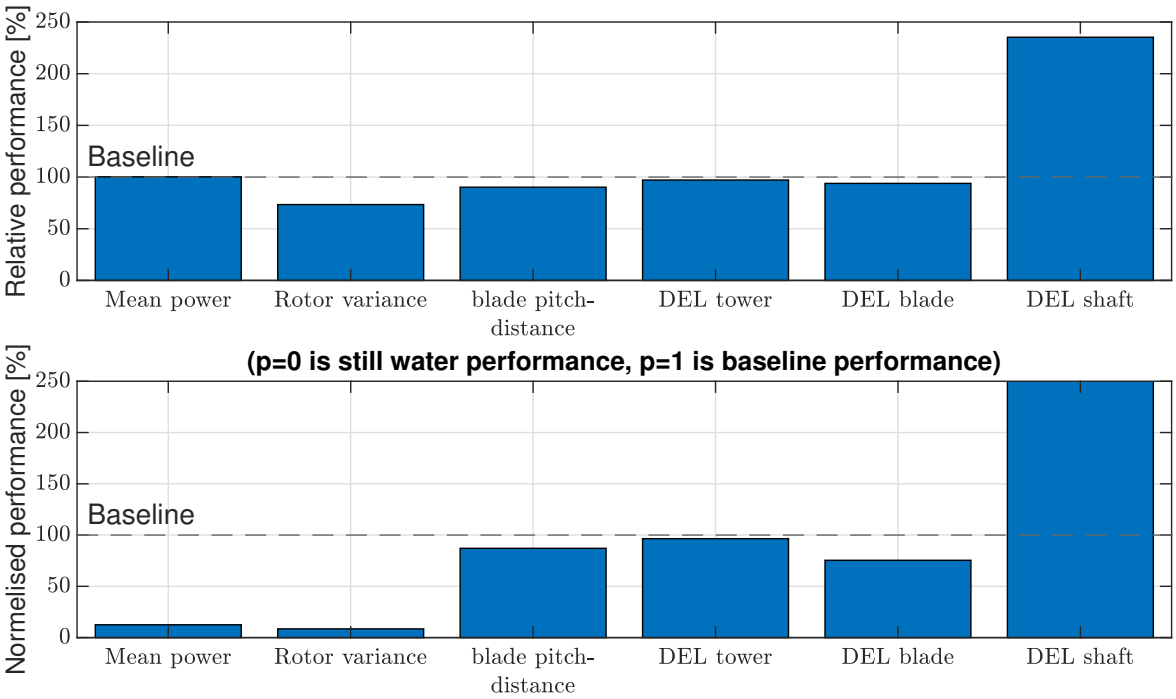

Figure 5-5: Weibull averaged performance of the MP controller, with respect to baseline control. Top: relative performance, i.e. amount of remaining negative effects. Bottom: normalised performance, i.e. amount of remaining *wave-induced* negative effects.

The relative performance in Figure 5-6 shows the performance relative to baseline. Load case 1 and 2 are similar to the BP controller. However, for the extreme load cases, the rotor speed variance decreases with over 50%. On the downside, the required pitch control action increases with over 200% for load case 6 and 7. Moreover, the shaft DEL increases with 362% and 585% for load case 3 and 4. The blade speed reduction in load case 4 and

5 is obtained because the FF controller uses generator control additionally in these regions. If the mechanical structure can handle these aggressive control inputs, performance can be increased tremendously. While the performance of FB control is limited by the RHP zeros, FF control is not subjected to these limitations. Therefore, more aggressive control becomes possible.

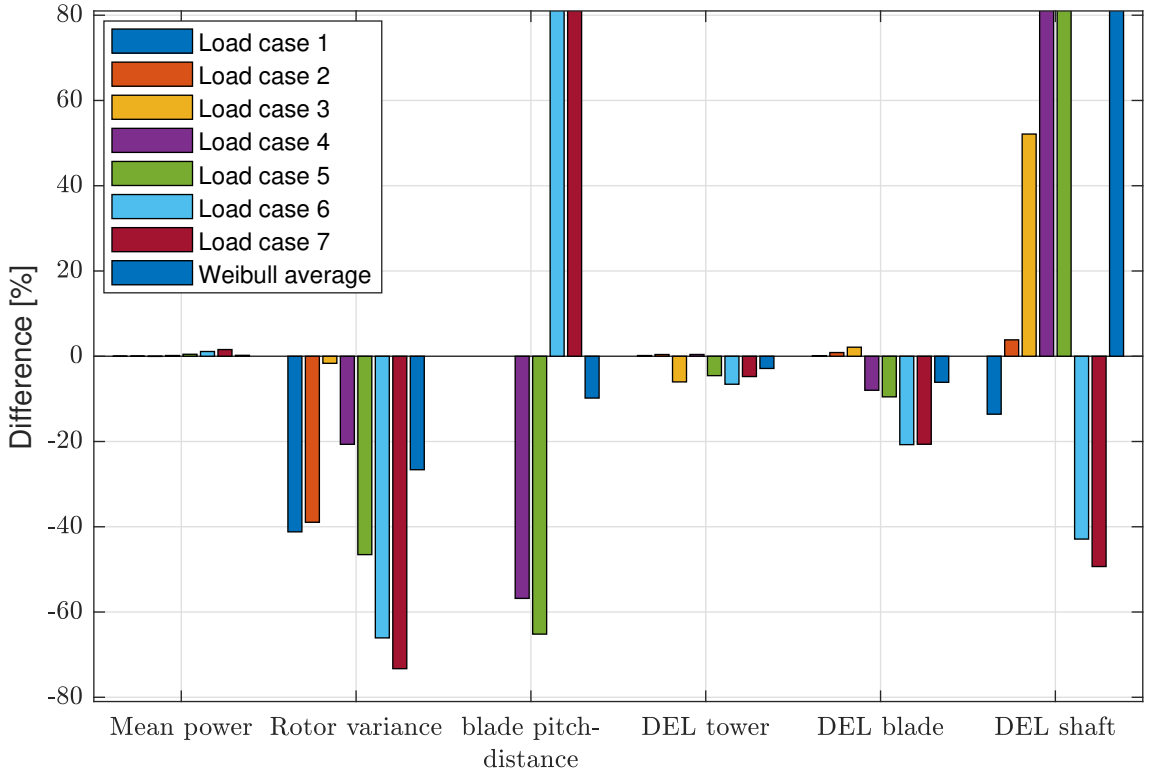

Figure 5-6: Relative performance of maximum-performance controller. Ratio of improvement, when adding wave-FF to baseline control.

For a thorough overview of the controller results, the Weibull-weighed performance metrics are shown in Figure 5-7. This figure provides a good overview of the achievements of wave-FF control, in a similar way to Figure 2-5. Summarising the controller results, the BP wave-FF controller shows moderate performance improvement at cost of only little additional torque control. The MP controller shows large performance improvement at the cost of large additional torque control.

A time- and frequency domain comparison in load case 4 between baseline control (blue), BP FF (red) and MP FF (yellow) is shown in Figure 5-8. The high-frequent collective blade pitch θ_c speed, power variations P and rotor speed variations Ω disappear at the cost of large additional torque-control action τ_g. Again, the low-frequent wind-induced variations remain present. Even though the controller is quite aggressive, it is clear that this new framework poses additional opportunities in the field of control. It raises the question of what additional control objectives can be obtained using wave-FF control. The implications with respect to other research, are discussed in the next chapter.

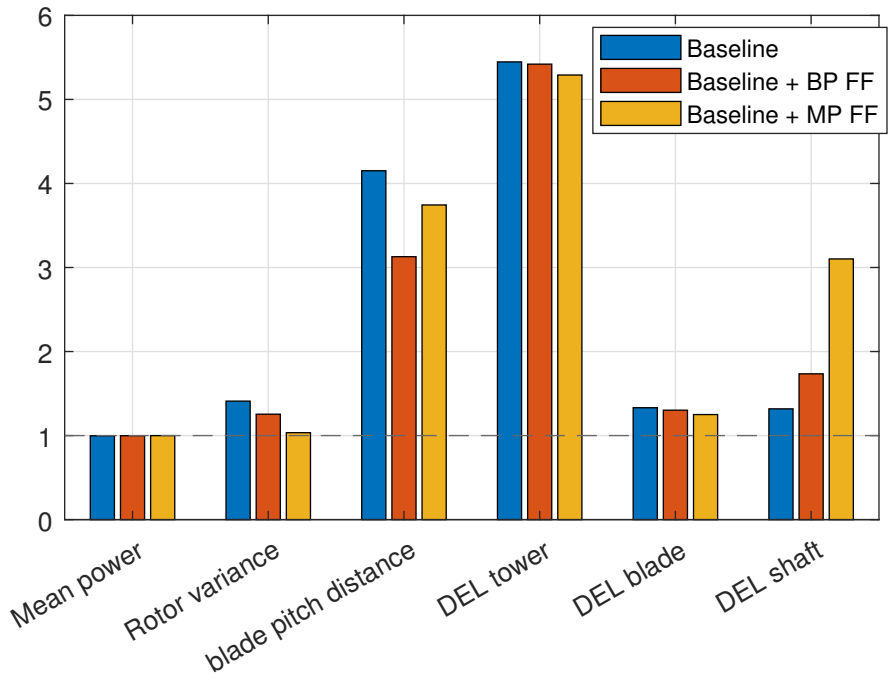

Figure 5-7: Final performance with respect to still water conditions, using three different controllers.

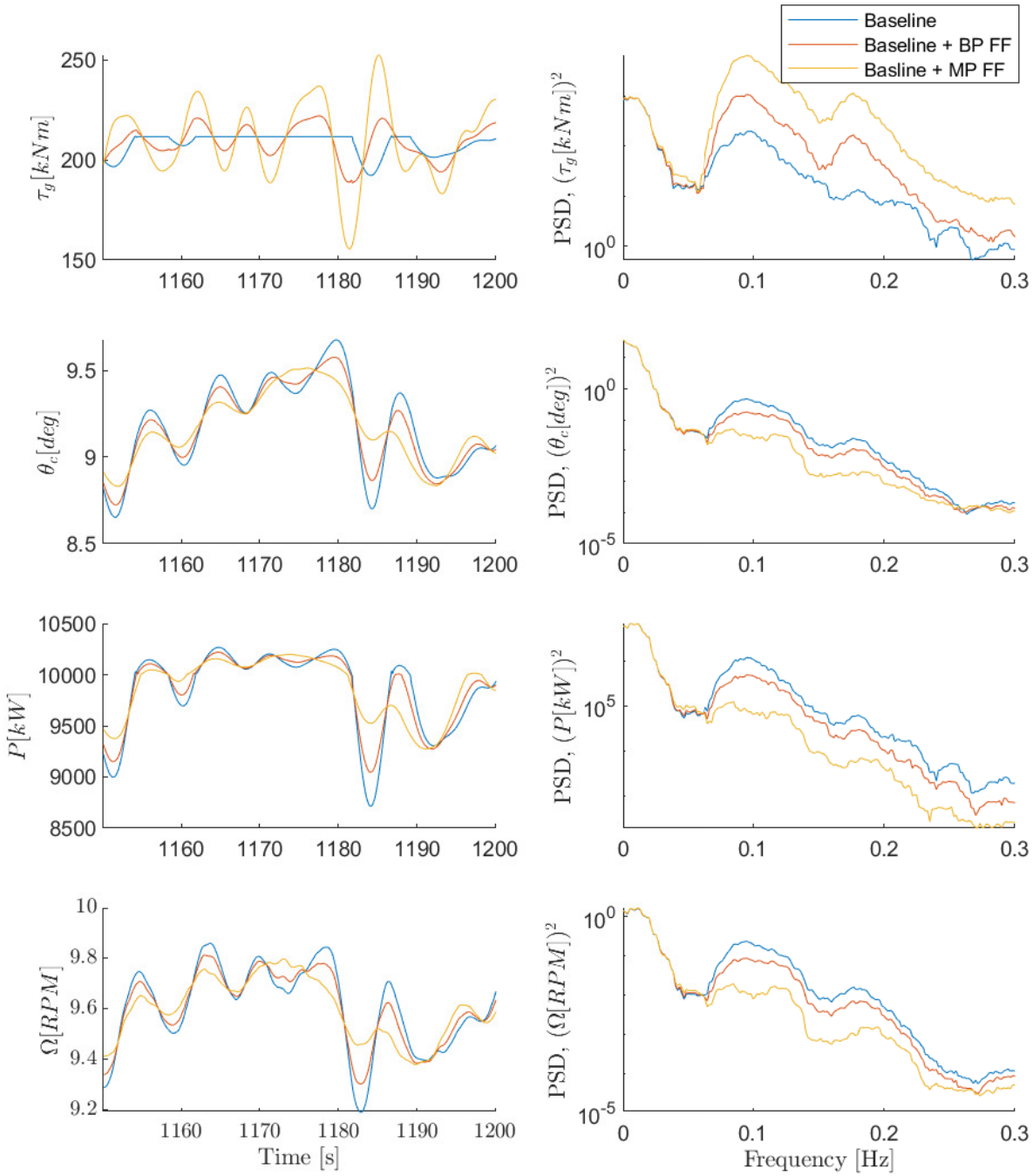

Figure 5-8: Simulation comparison using load case 4. Left (a part of) the time series, right the PSD.

5-3 Experimental testing

The results of the wave-FF controller should be validated using an experimental setup because an experiment would provide confidence on assumptions in this novel control strategy. A basin experiment with a scale of 1/50. has been set up, fully described in [55] It consists of a scaled OC6-DeepCwind reference platform (Figure 5-9, an extension on the OC5-DeepCwind [56]) and scaled 5MW NREL reference turbine [57]. The FOWT is deployed in a wave basin by MARIN. The thrust force is actively simulated by a virtual drone-like propeller. The mooring lines are modelled by a linear spring system. Because the experiments did not lead to any satisfactory results yet, the experiment is discussed only briefly.

A new wave-FF controller is designed for the new platform-turbine combination, based on a linearized model and using the wave-FF design procedure described in Section 4-4. The CROLM of the O6-DeepCwind platform is again computed and used to design a new wave-FF controller. Simulations in FAST on the new platform have shown similar results as on the 10MW TripleSpar. These results confirm the generalisability of the framework but are not further discussed in this research.

Figure 5-9: OC6-DeepCwind floating platform, used in the experimental test.

The setup is subjected to irregular waves ($H_s = 7.1$ m, $T_s = 12.1$s). The wave-spectrum is 2 dimensional. The setup is similar to the ROM description, yet with additional non-linearities and all elastic DOF. Two wave gauges are deployed to measure the waves as in Figure 5-10. One is at (real scale) 120 meter in front of the FOWT and one is at the same place as the FOWT. The controller is compiled to a dynamic link library (DLL) file for fast real-time computation. Platform motions are measured by high precision cameras. Loads are measured in the tower top. Non-measured states are estimated by FAST, running in parallel with the experiment. The simulation software is modified by research company SENER, such that the wave measurement can be used as a control input.

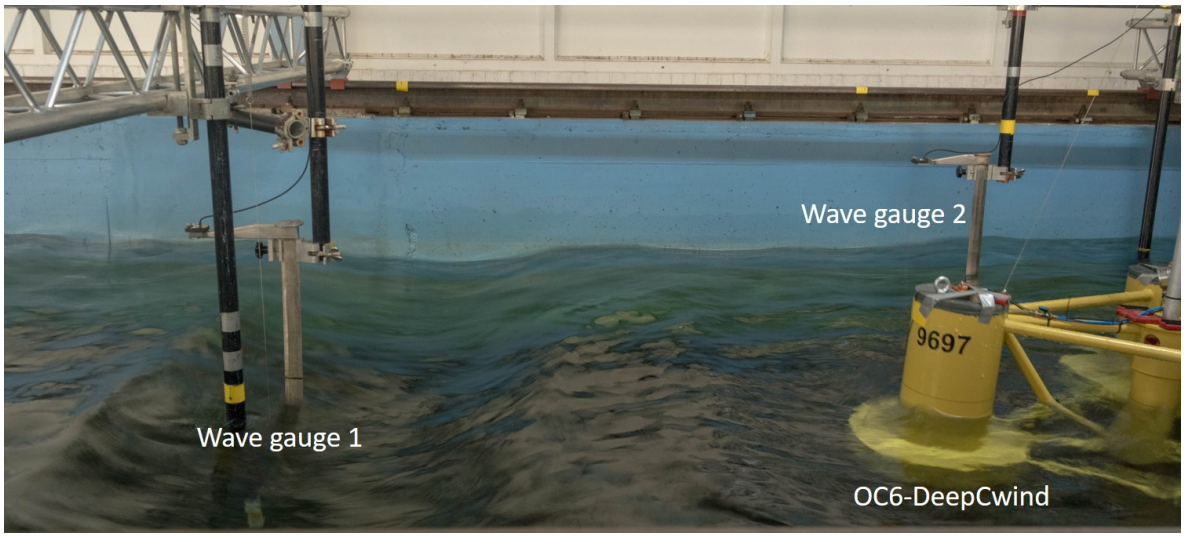

Figure 5-10: Experimental setup at MARIN, with a 2 dimensional spectrum of irregular waves acting on the floating platform.

The main interest of this experiment over simulation is to identify the differences between simulation and reality. Differences are expected to be found in higher-order wave excitation forces and wave propagation. These can be verified by an experiment. If responses are merely similar, this is a strong indication that the simplifications in the simulation are valid.

Unfortunately, the experiments have not succeeded. The virtual rotor provided increasingly large rotor thrust force oscillations, resulting in platform pitch instability. Therefore, the experiment was ended. The instability does not seem to be a result of the FF controller, for the following reason. One experiment was conducted without waves ($\eta(t) = 0$). Since the FF controller is a LTI TF, the control FF action u_{ff} is also zero. In this case, baseline+FF control is the same as regular baseline control. Yet, the system was still unstable. Therefore, a reasonable explanation is that the wave measurement was not passed correctly to the controller (i.e. not zero). This can be caused, for example, by the software modifications.
At the moment of writing this work, the data of the failed experiment was not yet available for further analysis. Therefore, no analysis of the exact cause can be conducted. Finding the cause is important before conducting any further experiments.

Fortunately, the data of the wave gauges is available for verification. Figure 5-11 shows the experimental surface elevation measurement η_0 at the platform location and the predicted surface elevation $\hat{\eta}_0$, for 10 seconds in advance. The figure shows a good prediction of the future surface elevations. However, the upper peaks are a little under-estimated, while the downs are a little over-estimated. This is presumably the effect of higher-order Stokes waves, i.e. wave non-linearity. Higher-order stokes waves are present in non-deep water or with steep waves [29]. Therefore, the extreme values are likely to be steep waves. Further research is required to take the higher-order wave dynamics into account in the wave prediction. However, the figure shows how the prediction is sufficient to provide a good estimate of the future wave elevations.

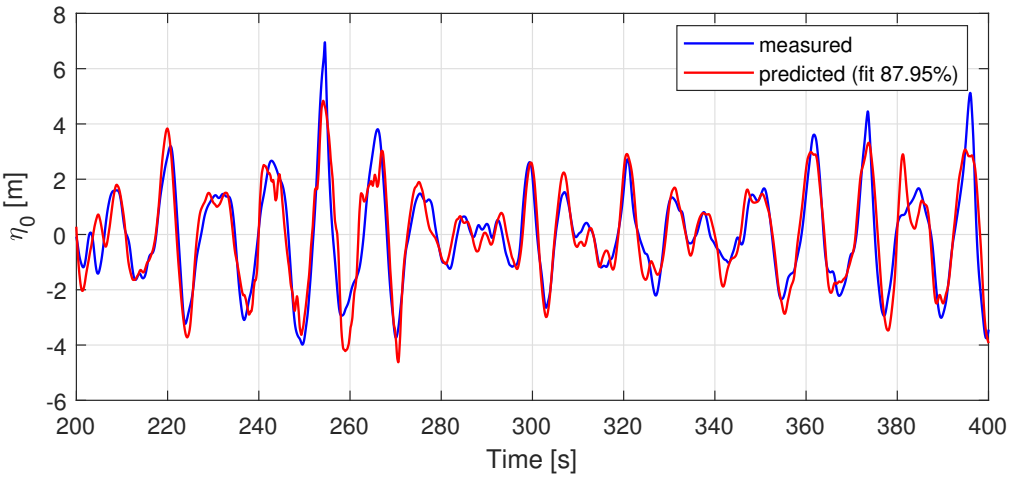

Figure 5-11: Experimental verification of the wave prediction method.

5-4 Conclusions

The two controllers, subjected to high-fidelity simulations, are showing promising results. The wave-knowledge allows FF control to improve performance without compromise using the BP controller. This involves large improvements for calm load cases and small improvements for extreme load cases. Particularly the rotor speed variations, blade pitch control action and power generation are improved. Improvements do not necessarily come at the cost of higher control action. However, additional control action *can* increase performance further.

The BP controller balances rotor speed reduction with a realistic control input. Considering the Weibull average over all load cases, the rotor speed variation is decreased by 11% (i.e. 41% of wave-induced rotor speed). The power production is increased by 0.10%, pitch-control action is decreased by 25% and the shaft DEL is increased by 31%. Because the control action is similar to the baseline controller, the BP FF controller is very realistic for implementation.

The MP controller rejects wave-induced rotor speed variations regardless of control action. It decreases rotor speed variations by 27% (i.e. 92% of the wave-induced). The power is increased by 0.14%, the mean pitch-control action by 13% and the blade DEL is reduced by 7%. On the downside, shaft DEL are largely increased by 150%

Wave-FF is most effective in calm weather. Using the BP controller in load case 1, 41% rotor speed variations are rejected (i.e. 95% of the wave-induced rotor speed variations) using 32% *less* control action. For load case 2, 22% (i.e. 54% of the wave-induced) rotor speed variations are rejected using 9% less control action. For load case 3, little improvement is found because waves have little effect. For higher load cases, the performance increases, but this can only be fully utilised at the cost of additional control input. Since wave-FF can only reject wave-induced responses, the low-frequent wind-induced response remains unaffected.

Experiments are conducted to verify wave-FF in a wave basin at MARIN. A new FF controller has been developed based on a new platform, the scaled NREL 5MW OC6-DeepCwind FOWT. The controller performs similarly with respect to the TripleSpar in FAST simulations. The experiments confirm the accuracy of the wave prediction method. Unfortunately,

no conclusions can be drawn with respect to the FF controller, most likely because of a bug in the software modification. Moreover, the experimental results of the controller are not yet available for analysis, at the moment of writing this work.

Chapter 6

Discussion

By using high fidelity simulations, wave disturbances are found to be of major influence on the performance of FOWTs. The outcome of this research on the potential of wave-FF to attenuate wave disturbances is twofold. First, the simulations show that FF control is very effective to attenuate wave-induced rotor speed variations. Second, a basis for further development proposed by a general design procedure. The procedure allows one to design a wave-FF controller for an arbitrary combination of control objective, floating platform and wind turbine.

The findings relate to the existing research in different ways. By linear system analysis, it is shown that FB control has particularly limited capabilities to attenuate wave-induced disturbances [35]. This study shows that FF control is able to attenuate these disturbances effectively. Moreover, FF control complements a regular FB controller. Most of the existing control logic can persist. FF can be combined with a state-of-the-art (FB) control strategy, such as LQR control [35], gain scheduling control [22] or even LIDAR assisted wind-FF control [27].
In comparison to recent findings on NMPC [25], which considers perfect wind- and wave preview, this work particularly demonstrates the potential of solely using a wave-preview. Moreover, while NMPC is computationally too complex to implement real-time, this FF framework *can* be implemented real-time because the controller is a simple linear time-invariant (LTI) transfer function.
A wave-excitation model (WEM) is identified to estimate the wave excitation forces based on a measurement of the surface elevation, similar to [32]. However, in this work, the parameterization is performed directly in the frequency domain. Moreover, the authors used future wave elevation measurements as an input for the WEM. In this work, a wave prediction model is developed to allow real-time implementation. The novel approach provides a low order LTI model with high accuracy.

This work is also subjected to certain limitations. First, a still-water FOWT linearization is required to design the controller. Currently, linearization requires (1) custom university software, (2) the future openFAST release for linearization or (3) adding wave-excitation forces as inputs to a FAST v7 still-water linearization. Fortunately, the openFAST update containing

linearization capabilities is already planned [45].
Second, scaled experiments have been conducted in the wave basin at MARIN, confirming the correctness of the wave prediction method. However, no conclusions can be drawn yet considering the FF controller, most likely due to an error in the experimental software. Moreover, the data of the FF experiment is not yet available for analysis at the moment writing this work. Experimental verification of the FF would have added more confidence to the results and would have provided a first step towards the analysis of non-linear wave excitation forces. In further research, the problem should be identified and care should be taken to prevent it before conducting additional experiments.
Third, in reality, the performance is negatively affected by the quality of the surface-elevation measurement. Although some methods are suggested, such as radar [30] or buoy measurements, none have been worked out. An accurate and realistic measurement system is key to realistic implementation.
Fourth, some output channels are found to be insensitive to control and are therefore difficult to attenuate. For example, tower-base load cycles are most affected by waves, however, control is less effective on the tower loads. As a result, not all control objectives might be feasible.
Lastly, compensation of waves is only possible in the direction of the rotor. In reality, a 3d wave spectrum is present and responses in other directions cannot be controlled.

Further research is needed, particularly to conduct scaled experiments using a wave-FF controller. Experiments allow further research on non-linear wave excitation force effects. Studying the first principles of higher-order wave excitation forces can potentially improve the WEM. Furthermore, the effect of measurement-errors should be identified.
Once wave-FF has been confidently tested, the simple wave-FF controller can be extended. FF control using state-estimation, multiple objectives or to reduce loads are promising new research directions. Moreover, one could use a cost function to obtain more than two control objectives. A FF strategy using a longer time horizon can be considered to use control actions more efficiently. Also, the practical implementation should be further exploited. The wave-measurement strategy should be elaborated. A scheduling rule for different controllers based on different linearizations is required. Also, a switching strategy should be established between FF torque- and pitch control. Finally, it is recommended to extend wave-FF to the barge platform. The barge is superior in terms of cost and engineering complexity [20], but it is very sensitive to wave disturbances. Wave-FF could particularly reduce this wave-sensitivity.

Chapter 7

Conclusion

In this research, we identified the effect of waves on a FOWT and developed a controller such that wave disturbances are attenuated. Based on high-fidelity simulations, mathematical derivation and linear system analysis, it was shown that the novel FF approach is able to strongly reduce the wave-induced rotor speed variations, without compromising on energy capture, control logic complexity or blade pitch control action.

Using high-fidelity simulations, it was demonstrated that waves have a large negative effect on the performance of the FOWT. Especially fatigue on the tower base (440% extra fatigue), blade-pitch control actions (420% extra) and rotor speed variations (42% extra) are affected[1]. Waves particularly influence the high-frequency responses, leading to strong oscillating accelerations. Also, waves are most influential in very calm and extreme load cases.

To design the model-based wave-FF controller, a causal reduced-order linear model (CROLM) of the TripleSpar was developed. The model consists of (1) a still water linear FOWT model, (2) a parametric wave-excitation model (WEM) to relate surface elevations to wave excitation forces and (3) a wave prediction method. A novel approach to parameterize the WEM was developed, showing a 98% variance accounted for (VAF) model fit. The wave prediction method predicts future surface elevations at the platform location, by using real-time wave measurements in front of the FOWT. This is required to obtain a causal WEM using the panel code in which reference platforms are defined. In contrast to current literature on wave excited linear FOWT models, the CROLM can be applied in real-time control purposes. Scaled experiments have been conducted in the wave basin at MARIN. These experiments have confirmed the correctness of the wave prediction method.

Based on the CROLM, a model-based wave-FF controller was developed. Linear system analysis was used to determine the control input sensitivity and disturbance sensitivity in certain frequency ranges and load cases. Two controllers were designed: one 9^{th} order transfer function (TF) for rotor speed variation reduction and one 12^{th} order TF for tower-base fatigue reduction combined with rotor speed variation reduction. Both controllers provide almost full compensation on the linearized plant. However, the load-reduction controller requires

[1] Based on the Weibull-average value of several load cases.

moderately large control actions. A design procedure was developed, mapping the complex controller design process into 9 clear steps. It allows one to design a wave-FF controller for some arbitrary FOWT or control objective.

The results of the FF rotor speed controller were demonstrated by using high-fidelity simulations, comparing the performance to the baseline controller. Based on a weighted Weibull-average over all load cases, a decrease in rotor speed variations of 27% is obtained. This is equivalent to 92% of the wave-induced rotor variations. At the same time, the collective pitch control action is reduced by 11%, while the control action on the generator torque increases the rotor shaft fatigue by 135%.
A second controller was designed to apply only moderate control actions, equal to or less than the FB control actions. A reduction in rotor speed variations of 11% is obtained using 25% less pitch control action and only increasing the rotor shaft fatigue by 31%. For all simulated FF controllers, the reduction in power variation is similar to the reduction in rotor speed variation. Wave-FF is found to be most effective in calm weather. At a mean wind speed of 5 m/s, rotor speed variations are reduced by 41% while using 31% less control action.

These results imply that further research on the topic of wave-FF control is recommended. Primarily, scaled experiments are recommended to verify the controller results and research the effect of higher-order wave excitation forces. Furthermore, this research raises the question of what additional objectives can be obtained using wave-FF control. In further research, the methodology can be applied to additional control objectives. In the long term, once the performance improvements are integrated into the design requirements, wave-FF could significantly enhance the economic feasibility of FOWTs.

Altogether, wave-FF control is found to be a feasible, simple and effective strategy to attenuate rotor speed variations on FOWTs. It is feasible because sensors to measure surface elevations are relatively low-cost and commercially available. It is simple because wave-FF does not require modifications to the feedback loop such that baseline controller properties are lost. It is effective because nearly all wave effects can be compensated. Despite waves inducing considerable disturbances on FOWTs, this work demonstrates how to efficiently reject wave-induced disturbances. After all, one cannot control the waves, but one can control how they affect a FOWT.

Bibliography

[1] The renewable energy financial advisors | green giraffe. https://green-giraffe.eu/. (Accessed on 10/18/2019).

[2] Jafar Jallad, Saad Mekhilef, and Hazlie Mokhlis. Frequency regulation strategies in grid integrated offshore wind turbines via vsc-hvdc technology: A review. *Energies*, 10(9):1244, 2017.

[3] Lucy Y Pao and Kathryn E Johnson. A tutorial on the dynamics and control of wind turbines and wind farms. In *American Control Conference, 2009. ACC'09.*, pages 2076–2089. IEEE, 2009.

[4] Wei Yu, Frank Lemmer, David Schlipf, Po Wen Cheng, Bart Visser, Harmen Links, Neelabh Gupta, Sabrina Dankemann, Bernardino Counago, and Jose Serna. Evaluation of control methods for floating offshore wind turbines. In *Journal of Physics: Conference Series*, volume 1104, page 012033. IOP Publishing, 2018.

[5] Torben J Larsen and Tor D Hanson. A method to avoid negative damped low frequent tower vibrations for a floating, pitch controlled wind turbine. In *Journal of Physics: Conference Series*, volume 75, page 012073. IOP Publishing, 2007.

[6] Christian Bak, Frederik Zahle, Robert Bitsche, Taeseong Kim, Anders Yde, Lars Christian Henriksen, Morten Hartvig Hansen, Jose Pedro Albergaria Amaral Blasques, Mac Gaunaa, and Anand Natarajan. The dtu 10-mw reference wind turbine. In *Danish Wind Power Research 2013*, 2013.

[7] lifes50plus. Deliverable 7.2: Design basis, 2017. Accessed: 28-05-2019.

[8] M Al. Control of floating offshore wind turbines: a study on state-of-the-art control strategies to enhance economic feasibility. 2019.

[9] United-Nations. Paris agreement, 2016.

[10] WindEurope. Wind in power: 2017 european statistics, May 2017. Accessed: 28-01-2019.

[11] Anders Myhr, Catho Bjerkseter, Anders Ågotnes, and Tor A Nygaard. Levelised cost of energy for offshore floating wind turbines in a life cycle perspective. *Renewable Energy*, 66:714–728, 2014.

[12] Eia - annual energy outlook 2019. https://www.eia.gov/outlooks/aeo/. (Accessed on 08/30/2019).

[13] M Dolores Esteban, J Javier Diez, Jose S López, and Vicente Negro. Why offshore wind energy? *Renewable Energy*, 36(2):444–450, 2011.

[14] Dennis YC Leung and Yuan Yang. Wind energy development and its environmental impact: a review. *Renewable and sustainable energy reviews*, 16(1):1031–1039, 2012.

[15] Jason Mark Jonkman et al. *Dynamics modeling and loads analysis of an offshore floating wind turbine*, volume 68. 2007.

[16] Henrik Stiesdal. Hywind: The worldâĂŹs first floating mw-scale wind turbine. *Wind Directions*, 31:52–53, 2009.

[17] Principle-Power. Windfloat. *Principle renewable energy delivered*, pages 1–2, 2011.

[18] Equinor. Hywind - leading floating offshore wind solution, 2017. Accessed: 27-01-2019.

[19] WindEurope. Floating offshore wind vision statement. *WindEurope*, 2017.

[20] Sandy Butterfield, Walt Musial, Jason Jonkman, and Paul Sclavounos. Engineering challenges for floating offshore wind turbines. Technical report, National Renewable Energy Lab.(NREL), Golden, CO (United States), 2007.

[21] Hazim Namik and Karl Stol. Individual blade pitch control of floating offshore wind turbines. *Wind Energy: An International Journal for Progress and Applications in Wind Power Conversion Technology*, 13(1):74–85, 2010.

[22] Omid Bagherieh and Ryozo Nagamune. Gain-scheduling control of a floating offshore wind turbine above rated wind speed. *Control Theory and Technology*, 13(2):160–172, 2015.

[23] Orhan Beker, CV Hollot, Yossi Chait, and Huaizhong Han. Fundamental properties of reset control systems. *Automatica*, 40(6):905–915, 2004.

[24] Young-Man Kim. Robust data driven h-infinity control for wind turbine. *Journal of the Franklin Institute*, 353(13):3104–3117, 2016.

[25] David Schlipf, Frank Sandner, Steffen Raach, Denis Matha, and Po Wen Cheng. Nonlinear model predictive control of floating wind turbines. 2013.

[26] Hazim Namik and Karl Stol. Disturbance accommodating control of floating offshore wind turbines. In *47th AIAA Aerospace Sciences Meeting including The New Horizons Forum and Aerospace Exposition*, page 483, 2009.

[27] David Schlipf, Paul Fleming, Florian Haizmann, Andrew Scholbrock, Martin Hofsäß, Alan Wright, and Po Wen Cheng. Field testing of feedforward collective pitch control on the cart2 using a nacelle-based lidar scanner. In *Journal of Physics: Conference Series*, volume 555, page 012090. IOP Publishing, 2014.

[28] Gene F Franklin, J David Powell, Abbas Emami-Naeini, and J David Powell. *Feedback control of dynamic systems*, volume 3. Addison-Wesley Reading, MA, 1994.

[29] Leo H Holthuijsen. *Waves in oceanic and coastal waters*. Cambridge university press, 2010.

[30] Jens Dannenberg, Katrin Hessner, Peter Naaijen, Henk van den Boom, Konstanze Reichert, et al. The on board wave and motion estimator owme. In *The Twentieth International Offshore and Polar Engineering Conference*. International Society of Offshore and Polar Engineers, 2010.

[31] Lisa Poyneer, Marcos van Dam, and Jean-Pierre Véran. Experimental verification of the frozen flow atmospheric turbulence assumption with use of astronomical adaptive optics telemetry. *JOSA A*, 26(4):833–846, 2009.

[32] Frank Lemmer, Steffen Raach, David Schlipf, and Po Wen Cheng. Parametric wave excitation model for floating wind turbines. *Energy Procedia*, 94:290–305, 2016.

[33] M Borg and M Collu. A comparison between the dynamics of horizontal and vertical axis offshore floating wind turbines. *Philosophical Transactions of the Royal Society A: Mathematical, Physical and Engineering Sciences*, 373(2035):20140076, 2015.

[34] Frank Lemmer. *Low-order modeling, controller design and optimization of floating offshore wind turbines*. Verlag Dr. Hut, 2018.

[35] Frank Lemmer, David Schlipf, and Po Wen Cheng. Control design methods for floating wind turbines for optimal disturbance rejection. In *Journal of Physics: Conference Series*, volume 753, page 092006. IOP Publishing, 2016.

[36] Morten Hartvig Hansen and Lars Christian Henriksen. Basic dtu wind energy controller. 2013.

[37] Erin E Bachynski, Marit I Kvittem, Chenyu Luan, and Torgeir Moan. Wind-wave misalignment effects on floating wind turbines: motions and tower load effects. *Journal of Offshore Mechanics and Arctic Engineering*, 136(4):041902, 2014.

[38] Bonnie Jonkman and Jason Jonkman. Fast v8. 16.00 a-bjj. *National Renewable Energy Laboratory*, 2016.

[39] Klaus Hasselmann, TP Barnett, E Bouws, H Carlson, DE Cartwright, K Enke, JA Ewing, H Gienapp, DE Hasselmann, P Kruseman, et al. Measurements of wind-wave growth and swell decay during the joint north sea wave project (jonswap). *Ergänzungsheft 8-12*, 1973.

[40] J CêŐň Kaimal, JCJ Wyngaard, YêŐň Izumi, and OR Coté. Spectral characteristics of surface-layer turbulence. *Quarterly Journal of the Royal Meteorological Society*, 98(417):563–589, 1972.

[41] Hazim Namik, Karl Stol, and Jason Jonkman. State-space control of tower motion for deepwater floating offshore wind turbines. In *46th AIAA Aerospace Sciences Meeting and Exhibit*, page 1307, 2008.

[42] Fernando D Bianchi, Hernan De Battista, and Ricardo J Mantz. *Wind turbine control systems: principles, modelling and gain scheduling design*. Springer Science & Business Media, 2006.

[43] NREL. Nwtc information portal (mlife). https://nwtc.nrel.gov/MLife. (Accessed 19-October-2019).

[44] Alexander J Coulling, Andrew J Goupee, Amy N Robertson, Jason M Jonkman, and Habib J Dagher. Validation of a fast semi-submersible floating wind turbine numerical model with deepcwind test data. *Journal of Renewable and Sustainable Energy*, 5(2):023116, 2013.

[45] Jason M Jonkman, Alan D Wright, Greg J Hayman, and Amy N Robertson. Full-system linearization for floating offshore wind turbines in openfast. In *ASME 2018 1st International Offshore Wind Technical Conference*. American Society of Mechanical Engineers Digital Collection, 2018.

[46] Alessandro Fontanella, Ilmas Bayati, and Marco Belloli. Linear coupled model for floating wind turbine control. *Wind Engineering*, 42(2):115–127, 2018.

[47] Johannes Falnes. On non-causal impulse response functions related to propagating water waves. *Applied Ocean Research*, 17(6):379–389, 1995.

[48] Chang-Ho Lee and J Nicholas Newman. Wamit user manual. *WAMIT, Inc*, 2006.

[49] IW Jamaludin, NA Wahab, NS Khalid, Shafishuhaza Sahlan, Z Ibrahim, and M F Rahmat. N4sid and moesp subspace identification methods. In *2013 IEEE 9th International Colloquium on Signal Processing and its Applications*, pages 140–145. IEEE, 2013.

[50] Jan Lunze. *Robust multivariable feedback control*. Prentice Hall Hemel Hempstead, 1988.

[51] EA Bossanyi, A Kumar, and O Hugues-Salas. Wind turbine control applications of turbine-mounted lidar. In *Journal of Physics: Conference Series*, volume 555, page 012011. IOP Publishing, 2014.

[52] Iker Elorza, Mikel Iribas, and Edurne Miranda. On the feasibility and limits of extreme load reduction for wind turbines via advanced sensing: A lidar case study. In *2013 American Control Conference*, pages 1436–1441. IEEE, 2013.

[53] Frank Lemmer, Steffen Raach, David Schlipf, and Po Wen Cheng. Prospects of linear model predictive control on a 10 mw floating wind turbine. In *ASME 2015 34th International Conference on Ocean, Offshore and Arctic Engineering*. American Society of Mechanical Engineers Digital Collection, 2015.

[54] Andras Varga. Balancing free square-root algorithm for computing singular perturbation approximations. In *[1991] Proceedings of the 30th IEEE Conference on Decision and Control*, pages 1062–1065. IEEE, 1991.

[55] Amy N Robertson, Erin E Bachynski, Sebastien Gueydon, Fabian Wendt, Paul Schünemann, and Jason Jonkman. Assessment of experimental uncertainty for a floating wind

semisubmersible under hydrodynamic loading. In *ASME 2018 37th International Conference on Ocean, Offshore and Arctic Engineering*. American Society of Mechanical Engineers Digital Collection, 2018.

[56] Amy N Robertson, Fabian Wendt, Jason M Jonkman, Wojciech Popko, Habib Dagher, Sebastien Gueydon, Jacob Qvist, Felipe Vittori, José Azcona, Emre Uzunoglu, et al. Oc5 project phase ii: validation of global loads of the deepcwind floating semisubmersible wind turbine. *Energy Procedia*, 137:38–57, 2017.

[57] Jason Jonkman, Sandy Butterfield, Walter Musial, and George Scott. Definition of a 5-mw reference wind turbine for offshore system development. Technical report, National Renewable Energy Lab.(NREL), Golden, CO (United States), 2009.

Glossary

List of Acronyms

BP	balanced performance
COF	centre of floating
COM	centre of mass
CL	closed-loop
CROLM	causal reduced-order linear model
DAC	disturbance accommodating control
DEL	damage equivalent load
DLL	dynamic link library
DOF	degrees of freedom
FA	fore-aft
FAST	fatigue, aerodynamics, structures, and turbulence
FB	feedback
FF	feed forward
FFT	fast Fourier transform
FOWT	floating offshore wind turbine
FRD	frequency response data
FT	Fourier transform
IFT	inverse Fourier transform
IFFT	inverse fast Fourier transform

JONSWAP joint North Sea wave project

LCOE levelised cost of energy

LHP left-half plane

LIDAR light detection and ranging

LQR linear-quadratic regulator

LSS low-speed shaft

LTI linear time-invariant

MARIN maritime research institute Netherlands

MP maximum performance

MIMO multi-input multi-output

MPC model predictive control

NDP negative damping problem

NMPC non-linear model predictive control

OL open-loop

OOP out of plane

OWT offshore wind turbine

PI proportional-integral

PSD power spectral density

RGA relative gain array

RHP right-half plane

ROM reduced-order model

RNA rotor nacelle assembly

SIMO single-input multiple-output

SISO single-input single-output

SLOW simplified low-order wind turbine

TLP tension leg platform

TRL technology readiness level

TF transfer function

VAF variance accounted for

WEM wave-excitation model

WT wind turbine

List of Symbols

η_0	Wave surface elevation at the centre of floating of the platform
η_A	Wave elevation at point x_A, in front of the FOWT
Ω	Rotor speed
ω	Angular frequency
Ω_{err}	Error between current rotor speed and optimal rotor speed
Ω_{opt}	Optimal rotor speed for maximum power production
τ_g	Electric generator torque
θ_c	Collective blade pitch angle
φ	Rotor azimuth angle
$\bar{v}_0$	Mean rotor effective wind speed
β_p	Platform rotational pitch displacement
$\boldsymbol{P}$	Load vector, containing F_x, M_y and T
$\hat{G}$	Linearized LTI model of the TripleSpar
$\hat{G}_d$	Linearized disturbance LTI model of the TripleSpar
$\hat{G}_i$	Linearized input LTI model of the TripleSpar
$\bar{v}_0$	Mean rotor effective wind speed
$\hat{G}_i$	Linearized input LTI model of the TripleSpar
$\mathbf{x}$	State vector of the ROM
C	Controller
C_{τ_g}	Baseline generator torque controller
C_{θ_c}	Baseline blade pitch angle controller
$cM_{y,T}$	Tower base momentum, multiplied with some constant
d	Water depth
f^{we}	Bandwidth wherein waves occur
f^{wi}	Bandwidth wherein wind occurs
F_x	Surge force
F_x^{we}	Wave induced surge force
F_z	Heave force
F_{thrust}	Aerodynamic thrust force
G	Non-linear plant of he TripleSpar
g	FF controller gain
$H_d(\omega)$	Wave prediction function
H_s	Significant wave height
M_y	Pitch moment
M_y^{we}	Wave induced pitch moment
$M_{b,oop}$	Blade out-of-plane moment
M_{LSS}	Bending moment LSS
$M_{y,T}$	Tower bending moment

N	System order
P^{we}	Wave induced loads
p_i	Probability of load case i to occur
s	Laplace vaiable
T	Aerodynamic rotor torque
t	Time
t_d	Future time of wave prediction
T_s	Significant wave period
u	System input of some (linear) system
v_0	Absolute rotor effective wind speed
x_A	Wave measurement point, L meters in front of the FOWT
x_d	Fore-aft tower deflection
x_p	Platform translational surge displacement
x_t	Tower-top displacement
y_i	Output channel i of some (linear) system
z_p	Platform translational heave displacement (upwards)
DEL(M(t))	1 Hz-fatigue-equivalent load of the time series $M(t)$
q	Configuration vector, containing the model DOF
T_s	Sampling time of the simulation
v_r	Relative wind speed